EFFECTS OF DRESSING PARAMETERS ON GRINDING WHEEL SURFACE TOPOGRAPHY

A Thesis
Presented to
The Academic Faculty

by

Craig Woodin

In Partial Fulfillment
Of the Requirements for the Degree
Master of Science in the
School of Mechanical Engineering

Georgia Institute of Technology
December 2014

EFFECTS OF DRESSING PARAMETERS ON GRINDING WHEEL SURFACE TOPOGRAPHY

Approved by:

Dr. Shreyes Melkote, Advisor
School of Mechanical Engineering
Georgia Institute of Technology

Dr. Steven Liang
School of Mechanical Engineering
Georgia Institute of Technology

Dr. Thomas Kurfess
School of Mechanical Engineering
Georgia Institute of Technology

Date Approved: November 14, 2014

ACKNOWLEDGEMENTS

I would like to express my special appreciation and gratitude to my research advisor, Professor Shreyes Melkote, for his mentorship and guidance throughout my undergraduate and then graduate research. I would also like to thank my committee members, Professor Steven Liang and Professor Thomas Kurfess for serving as my committee members. A special thanks to my lab mates, friends, and family members who provided support and encouragement throughout my academic career.

This thesis would also not be possible without the financial and in-kind support of this work by the Caterpillar Technical Center. X-ray micro-tomography (µCT) services were performed by ImageIQ. Grinding wheels, diamond dresser, and assistance were provided by Mike Hitchiner of Saint-Gobain.

TABLE OF CONTENTS

LIST OF TABLES

LIST OF FIGURES

Page

SUMMARY

Grinding is a critical manufacturing process and is often the only alternative when producing precision components or when machining brittle materials such as ceramics. Characterizing and modeling the surface finish in the grinding process is a difficult task due to the stochastic nature of the size, shape and spatial distribution of abrasive grains that make up the surface of grinding wheels. Since the surface finish obtained in grinding is a direct function of the wheel surface topography, which is conditioned by a single point dressing process, understanding the effects of dressing parameters on the wheel topography is essential. Therefore, the main objectives of this thesis are: 1) to experimentally characterize the three-dimensional surface topography of a conventional grinding wheel including attributes such as the abrasive grain height distribution, grain geometry and spacing parameters and their respective statistical distributions, 2) to determine the effects of single point dressing conditions on the three-dimensional wheel surface topography parameters and their distributions, 3) to model and simulate the three-dimensional wheel surface topography, and 4) to experimentally validate the wheel topography model. In this research, new and existing characterization methods are used to characterize the wheel surface and the individual abrasive grains. The new techniques include the use of X-ray micro-tomography (μCT) to obtain a better understanding of the grinding wheel's internal micro-structure, and a focus variation based optical measurement method and scanning electron microscopy to characterize previously ignored attributes such as the number of sides and aspect ratio of individual grains. A seeded gel (SG) vitrified bond conventional grinding wheel is used in the study. A full factorial design of single point wheel dressing experiments is performed to investigate the effects infeed and lead dressing parameters on the grinding wheel surface topography. A custom wheel indexing apparatus is built to facilitate precision relocation of the grinding wheel surface to enable optical comparison of the pre- and post-dressing wheel surface topography to observe wheel surface generation mechanisms such as macro-fracture and grain dislodgement. Quantitative descriptions of how each dressing parameter affects the wheel surface characteristics are given in terms of the wheel surface roughness amplitude parameters (*Sp, Ssk, Sku*) and areal and volume parameters (*Spk, Sk, Vmp, Vmp, Vvc, Smr1*) derived from the bearing area curve. A three-dimensional wheel topography simulation model that takes as input the abrasive grain height distribution and the statistical distributions for the various abrasive grain geometry parameters is developed and experimentally validated.

The results of wheel characterization studies show that the actual abrasive grain height distribution in the SG wheel follows a beta distribution. The µCT work shows that the abrasives are polyhedral in shape, as opposed to the spherical or conical shapes commonly assumed in grinding literature. Grain spacing is found to follow a beta distribution while the number of sides of the grain and the grain aspect ratio are found to follow the gamma and the Weibull distribution, respectively. The results of the dressing study show that the lead dressing parameter has the strongest effect on wheel topography. Using statistical distributions for the key parameters (e.g. grain height, number of sides, grain spacing), a stochastic three-dimensional model is developed to simulate the wheel surface topography under different dressing conditions. The resulting model is shown to yield realistic results compared to existing models mainly due the fact that additional abrasive grain geometry parameters and more realistic assumptions of the different grain attributes are used in the model. It is shown that the model follows the overall wheel surface topography trends during dressing but has difficulty in accurately simulating some of the wheel characteristics under specific dressing conditions. The thesis then concludes with a summary of the main findings and possible future research avenues including extending the model to rotary dressing and simulation of wheel-workpiece interaction.

1. INTRODUCTION

1.1 BACKGROUND

Grinding is one of the oldest machining processes and has been used since the stone ages to accomplish such tasks as creating hunting tools. Times have changed and now precision grinding is a complex machining process widely used to produce precision components such as bearing rings, lenses, and structural components. Even with lower production speeds, the grinding process is often preferred due to its ability to produce superior surface finish, and is often the only alternative when finishing brittle materials such as tool steels, ceramics, and optical materials. One of the first and main determining factors of the final ground surface quality is the dressing of the grinding wheel. The relationship of the dressed grinding wheel topography and ground surface finish is very important and is greatly affected by the dressing process. The ability to accurately simulate the grinding wheel topography after dressing would aid in increasing the efficiency of the grinding process resulting in greater number of high quality parts produced in less amount of time.

1.2 PROBLEM AND MOTIVATION

Precision grinding wheels are very complex due to the stochastic nature of abrasive grains, which are randomly placed within the volume of the grinding wheel that consists of a bonding material and porosity created during the wheel manufacturing process. Traditionally, efforts to study the three-dimensional grinding wheel surface as a function of the dressing condition has focused on either conventional aluminum oxide [1]–[3] or super-abrasive wheels such as diamond [4]–[6] or CBN [7]–[12]. In contrast, very limited work on seeded-gel wheels (SG) grinding wheel surface topography and its dressing response has been reported. The scanning electron microscope (SEM) image in Figure 1.1 demonstrates the complexity of a typical SG grinding wheel surface.

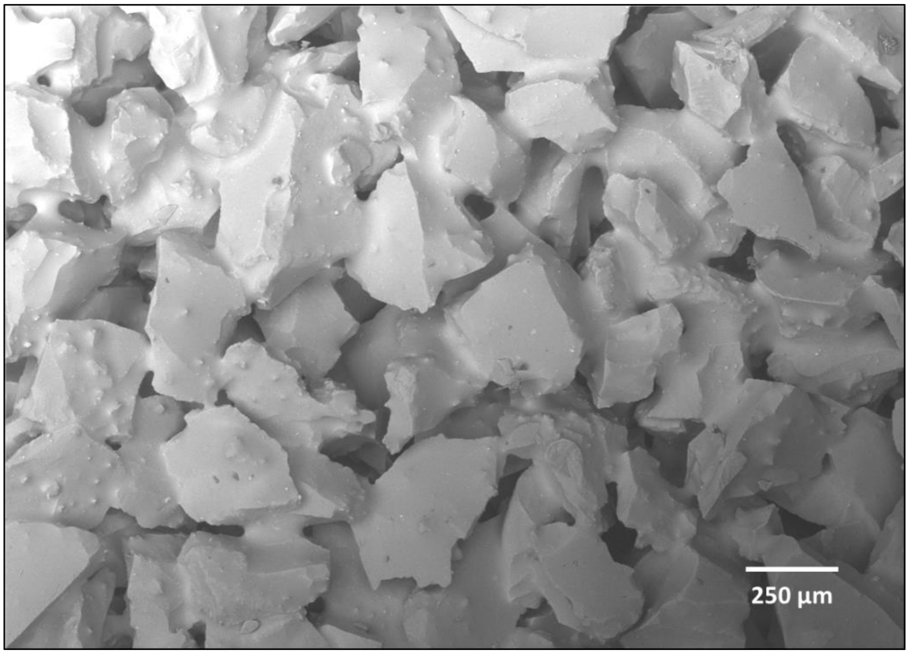

Figure 1.1 – SEM image of a precision grinding wheel

The surface of the grinding wheel changes as a result of the interaction of the diamond dresser with the abrasive grains and bond material. Surface metrology techniques have advanced in recent years and now allow for more precise methods for measuring the complex surface texture of grinding wheels. Scanning electron microscopes are very useful to provide qualitative information and are generally used in combination with other measurement methods that can describe the surface quantitatively. A superior measurement apparatus is necessary to measure the surface and how it changes as a function of the dressing conditions such as infeed, which represents the depth the diamond dresser engages into the wheel surface, and how fast it traverses across the wheel (dressing lead). Different methodologies for measuring the surface of grinding wheels ranging from simple two-dimensional contact methods to advanced three-dimensional scanning instrumentation need to be explored to precisely describe the surface of the grinding wheel.

In order to describe the transformation of the wheel surface due to dressing, it is important to fully understand and characterize the grinding wheel surface topography and how it changes throughout the dressing process. Grinding wheels are typically described in terms of the surface texture height distribution, abrasive grain size distribution, and grain density. The question is if there are other characteristic parameters that should be used to describe the grinding wheel surface topography as precisely as possible.

Stochastic simulation models are often used to describe the wheel surface since the grinding wheel surface topography consists of randomly distributed abrasive grains, bonding material, and porosity. This modeling technique is often chosen since the fracture and/or dislodgement of an abrasive grain from the bond is complex and depends on many random factors such as the dressing load, extent of adhesion between the bond and the grain, fracture toughness of the abrasive, and stress concentrations at the grain-bond interface [8].

Verification of the resulting simulation of the precision grinding wheel surface topography is needed to determine its validity, which is often overlooked in previously reported models. Simulations can be validated in both qualitative and quantitative terms. The majority of existing grinding wheel topography simulation models result in geometry that lacks the realism of an actual grinding wheel surface topography. Quantitative validations of wheel surface topography models are often limited by the ability of the measurement and analysis equipment.

1.3 RESEARCH OBJECTIVES

The main focus of this research is to accurately characterize, model, and understand how the surface topography of a precision grinding wheel changes during the single point diamond dressing process. The specific objectives of this work are as follows:

1. Understand the effects of single point diamond dressing parameters on seeded-gel (SG) grinding wheel surface topography**.**
2. Characterize the grinding wheel and individual grain geometry of the SG grinding wheel.
3. Develop a three-dimensional surface topographical model of the SG grinding wheel surface based on the wheel characterization findings.
4. Validate the wheel surface topography model by comparing model simulations to experimental results for different dressing conditions.

1.4 THESIS OUTLINE

The second chapter of this thesis begins with an overview of different methods for measuring the surface of grinding wheels ranging from simple two-dimensional contact profilometry to advanced three-dimensional scanning techniques. As with improvement in measurement techniques, modeling and simulation of the grinding wheel surface topography has advanced as well. Different grinding wheel topography modeling methods are therefore reviewed. The chapter concludes by summarizing the limitations of the current methods and emphasizes the need for additional research in dressed wheel surface characterization and modeling.

Chapter 3 of the thesis describes the characterization of the grinding wheel surface using various types of measurement equipment. Precision grinding wheels are often difficult to characterize due to the stochastic nature of abrasive grinding grains, which are randomly distributed on the wheel surface. The wheel characterization study is broken into two main components including characterization of the wheel surface and characterization of the individual grits/grains. Statistical distributions of the key parameters (e.g. grit density, grit size, grit height, number of sides of grit, grit spacing) are then determined and analyzed.

Single point dressing experiments on seeded gel grinding wheels are performed and summarized in Chapter 4. The experimental grinding wheel dressing trials are performed on a seeded-gel (SG) grinding wheel using a single point diamond dresser mounted on a cylindrical grinding machine. The surface of the grinding wheel is measured using three-dimensional optical surface measuring instrumentation. A full factorial design of experiment is utilized to determine the effects of the lead and infeed dressing parameters on the SG grinding wheel surface topography. The findings of the experimental trials along with appropriate characterization of the grinding wheel are employed to create a stochastic model to describe how the surface topography of the grinding wheel changes due to single point dressing.

Chapter 5 presents a stochastic model for the simulation of three-dimensional wheel surface topography. The statistical inputs to the model consist of the distributions for the key wheel parameters established in the characterization and experimental chapters. A stochastic modeling method was used since the interaction between the dressing diamond and the randomly structured grinding wheel surface is complex and stochastic in nature. The transformation of the wheel surface topography during dressing is characterized by such factors as grit fracture and/or grain pull-out, which occur in a stochastic manner.

The outputs of the wheel topography model are validated against experimental data in Chapter 6. The main surface topographical parameters chosen for model validation include the wheel surface texture height, bearing area, and volume parameters.

2. LITERATURE REVIEW

This chapter summarizes and reviews past studies on the measurement and simulation of the surface topography of precision grinding wheels. The chapter begins with an overview of different methodologies of measuring the surface of the wheels ranging from simple two-dimensional contact methods to using advanced three-dimensional scanning instrumentation. As with improvement in measurement methods, simulation of the grinding wheel has advanced as well. Different wheel topography modeling methods are then introduced. The limitations, as well as research areas for each method of measurement and surface topography modeling methods are discussed. The chapter then concludes by summarizing the limitations of the current methods and emphasizing the need for additional.

2.1 INSTRUMENTATION TO MEASURE SURFACE TOPOGRAPHY

The technology of surface metrology has advanced in the recent decades allowing for more precise methods for measuring the surface texture of grinding wheels and workpiece surfaces. The main concentration of this work is the study of the grinding wheel surface topography. As technology has advanced, surfaces can be characterized using advanced methods that enable researchers to observe and understand more of the surface microstructure. For comparison, in 1952 Backer *et al*. rolled a grinding wheel under its own weight on a glass plate covered by carbon powder [13]. The image of the imprint on the carbon was then magnified and projected to count the number of cutting points and was actually used as a peak count of abrasive grains that protruded from the wheel surface contacting the workpiece surface during the grinding process. Additionally, other early work involved rolling the grinding wheel over a piece of Sanborn recording paper to observe surface mapping characteristics of the grinding wheel [14].

There are many different technologies used to measure the surface texture of grinding wheels. Some researchers in the past have relied on scanning electronic microscopes (SEM) to characterize surfaces [1], [15]–[17] but they are generally used in combination with other measurement methods. Syoji *et al.* used a pair of scanning electronic microscope (SEM) stereo photographs to generate the grinding wheel topography in three dimensions, by comparing photographs taken simultaneously from different angles [18]. Information about the height, represented by the third dimension, can then be obtained through a triangulation process to measure the surface. During the 1960s and 1970s, the characterization of engineering surfaces became more prevalent for research as a result of the increasing availability of low cost computing and development of low cost microprocessors [19].

Of the many different approaches available to measure the surface topography of surfaces (including grinding wheels), the main methodologies include contact and non-contact instrumentation. The follow up sections discuss these methods. Note that this thesis concentrates on *static* methods for measuring the grinding wheel surface topography. The *static* cutting edges include all the cutting edges of the grinding wheel while the *dynamic* cutting edges are those actually involved in the cutting action [20]. *Dynamic* measurement methods include such techniques as acoustic emission, thermocouple, and scratching of test specimens.

2.1.1 Contact Instrumentation

First, stylus profilometers were developed in the 1930's without much advancement for the next 30 years [21]. It was then realized that the effects of waviness and form errors influence the values obtained and it became necessary to specify surface roughness on engineering drawings during manufacturing [22]. The introduction of the first scanning electron microscopes (SEM) and the resulting images of the workpiece surface triggered the need for quantitative height information [23]. Stylus instruments are one of the oldest and widely used methods of measuring surface topography and their measurement limitations have been widely investigated and documented [19], [24], [25]. There are two main types of contact instrumentation including two-dimensional and three-dimensional measurement methods.

2.1.1.1 Two-Dimensional Contact Measurement

Early stylus measurements were carried out by traversing the measurement probe across the surface and recording the vertical movement of a lever arm. The major improvements of these systems were due to the advancements in the logging of data and sensors attached to the lever arm.

In newer systems, the basic apparatus consists of a stylus probe that is traversed across a surface and a pick-up. The pick-up is physically attached to the tip and converts the vertical movements into an electrical signal to be analyzed. The electrical signal is then amplified and digitized to be processed by a computer. A linear variable differential transformer (LVDT) or an optical transducer are used in the pick-up and the translation stages are controlled by a gearbox driven by either a stepper motor, a DC motor or a linear motor regulated by a driving unit [24]. Early research of grinding wheel surface topography characterization was performed with this measurement method [26]–[31]. A typical example of two-dimensional stylus measurement is shown in Figure 2.1 Approved national and international standards exist for measurements made using two dimensional stylus instruments [23].

Figure 2.1 – Typical two-dimensional stylus measurement of 46 grit grinding wheel [26]

2.1.1.2 Three-Dimensional Contact Measurement

Early two-dimensional methods worked adequately for the time and provided basic surface profile information. A new three-dimensional method using stylus instrumentation was proposed by Williamson [32] and Peklenik [33] in the late 1960s. Additional surface topography information added to the two-dimensional method provided an area map of the surface via a raster scan measurement approach. A *raster scan* is a collection of parallel two-dimensional profile traces where each individual profile is spaced equally along the *x,y* directions providing a three-dimensional output of the surface [34]. These three-dimensional maps can be used to calculate areal roughness parameters. Many authors have used the three-dimensional stylus method to map surfaces of grinding wheels [24], [35]–[40] . Blunt and Ebdon [39] used a Somicronic Surfascan 3D stylus-based measuring instrument and Nguyen and Butler [35] used a Talyscan 150 stylus system to characterize the grinding wheel surface.

2.1.2 Non-Contact Instrumentation

Non-contact measurement methods range from conventional optical microscopes to advanced methods utilizing white light interferometric instrumentation and beyond. The measurement method utilized is determined by the required information to be obtained during the measurement process. Lachance *et al.* used a conventional microscope mounted to a grinding machine but they were only looking to obtain information such as identifying the cutting edges and wear flats between grinding cycles [15]. Due to the simplicity of the system, he was unable to identify the sharp cutting edges or the protrusion height of the grinding wheel grains. More advanced systems are needed for such measurements and will be summarized in the following section including such methods as i) laser displacement and triangulation, ii) white light interferometry, and iii) confocal microscopy.

2.1.2.1 Laser Displacement and Triangulation

Laser based methods are one of the simplest non-contact measurement systems. It is relatively low cost, but offers poor resolution [41]. The measurement system works by focusing a laser beam onto a surface and the illuminated point is imaged onto a position sensitive device. This device is calibrated in terms of the surface height. The use of lasers for measuring surfaces is broken into two main categories. The term *laser displacement* generally refers to two-dimensional measurement while *laser triangulation* takes three-dimensions into consideration throughout the measurement process.

Laser displacement is used to eliminate some sources of error found in early mechanical sensors and were adopted to trace the wheel profile in some studies [42],

[43]. They are two-dimensional systems that provide information for characterization of the grinding wheel form deviations, waviness, and roughness.

Some authors such as Brinksmeier [43] and Liu [44] have utilized the more advanced three-dimensional method of triangulation. The basic principle of laser triangulation method is illustrated in Figure 2.2.

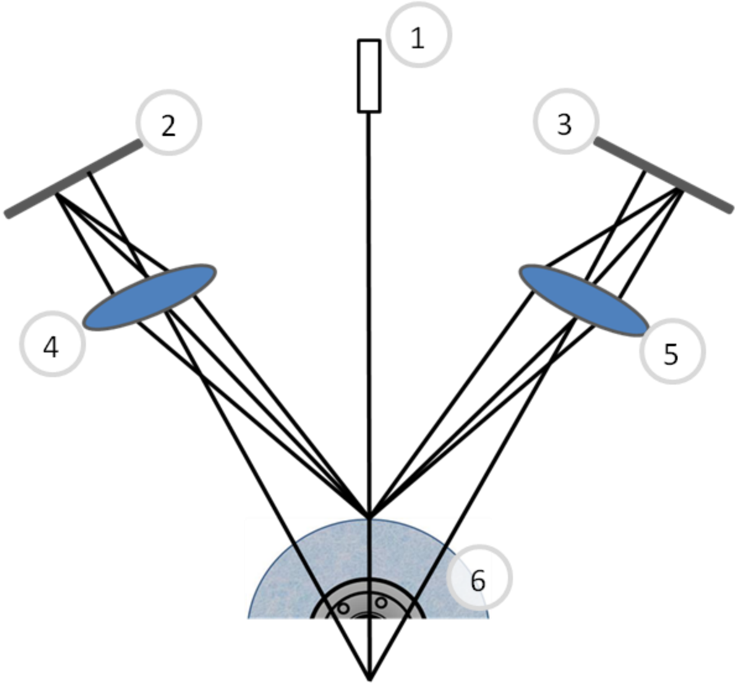

Figure 2.2 – Laser triangulation measurement. (1) laser, (2) PSD-1, (3) PSD-2, (4) lens-1, (5) lens-2, and (6) sample [45]

The laser triangulation instrument consists of a laser, lens group, and a position sensitive device (PSD) making up the scanning probe and operates on the following basic principle:

1. Scanning probe is moved along the horizontal (*x*-axis) direction.
2. Position of the reflection point on the grinding wheel surface changes in the *z*-axis direction.

3. The corresponding imaging position of the light spot on the PSD changes and is sent to the computer by the analog-to-digital converter.
4. The height values in the vertical (*z*-axis) direction can be calculated by the triangulation relationship.

2.1.2.2 White Light Interferometry

Optical interferometry was typically only used for visualization of surfaces and qualitative analysis until the 1970's mainly due to their complexity and time consuming operation [34]. These undesirable attributes were overcome with advancements in computing and electronics. The basic principle of the white light interferometric profilometer is shown in Figure 2.3.

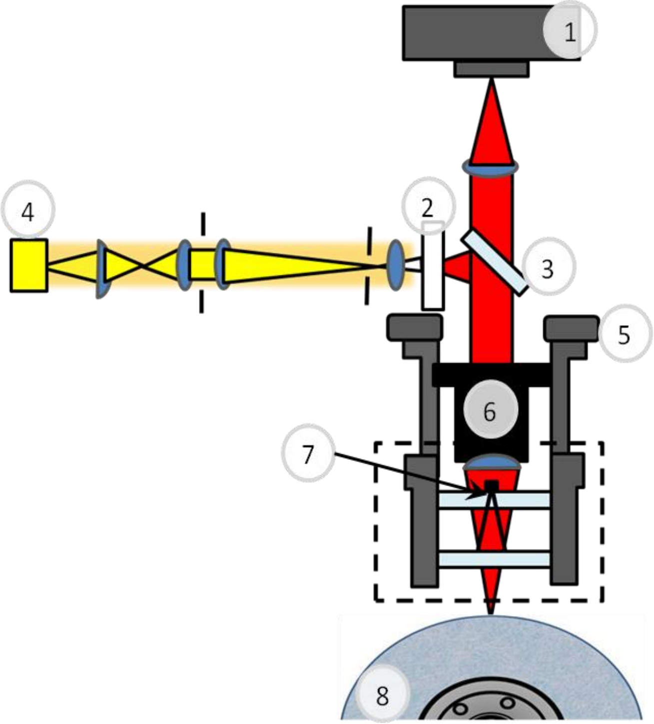

Figure 2.3 – Principle of interferometric profilometer- (1) CCD detector, (2) filter, (3) beam splitter, (4) light source, (5) PZT, (6) microscope objective, (7) reference surface, and (8) sample [46]

The concept is that a beam of light exiting a single source (light source after filter) is divided into two beams by a beam splitter. The basic operating principle is:

1. One beam is reflected from the reference surface and while the other one is reflected from the sample (grinding wheel surface).
2. During the measurement, the microscope objective is moved vertically by a piezoelectric transducer.
3. The two reflected beams are recombined by the beam splitter to produce interference fringes.
4. The imaging lens projects the interferogram onto the CCD camera.
5. The interferogram is analyzed to determine the surface height.

The function of the CCD detector records the intensity of the fringe pattern for the reference sample surface *I(x,y)* used to calculate the phase *Φ(x,y)*. The basic equation to measure the height *h* for each coordinate pair *(x,y)* is obtained with the phase *Φ(x,y)* using the equations [34]

$$h(x,y) = \frac{\lambda}{4\pi}\Phi(x,y) \tag{2.1}$$

$$I(x,y) = A + Bcos[\Phi(x,y) + \alpha_i] \tag{2.2}$$

where A is the average intensity, B is a constant, i is the axial shift position, and α is the controlled phase angle.

White light interferometry has been used by many authors [16], [46]–[48]. Yan *et al*. used a white light interferometer to measure and characterize a sample of a grinding wheel [46]. Cai and Rowe [16] compared the results of measuring a CBN grinding wheel using a stylus, interferometry, and laser triangulation measurement systems with the assistance of replica material due to the sample size limitations. The resulting surface roughness of the replica was about 60-90% of the value for the wheels based on the surface roughness of the grinding wheel [16]. Another limiting factor of using this type of equipment for measuring grinding wheels is that the vertical range is limited, so accurate measurement of surface of larger amplitudes are more difficult [34].

2.1.2.3 Confocal Microscopy

The concept of confocal microscopy is divided into two main including optical [4], [11], [48]–[50] and chromatic [20], [51], [52] systems. Hegeman used confocal microscopy to measure the grain base radius and grain protrusion heights [4]. Basic explanation of the fundamental concept of the confocal microscope is illustrated in Figure 2.4.

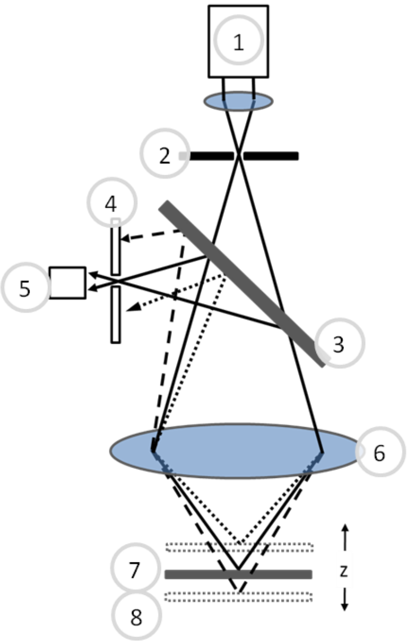

Figure 2.4 – Principle of optical confocal microscopy- (1) laser/light source, (2) illumination pinhole, (3) beam splitter, (4) confocal aperture/ detector pinhole, (5) detector, (6) objective lens, (7) focal plane, in-focus, and (8) focal plane, out-focus [4]

The optical confocal microscope works by the defocusing effect when light is reflected from the piece being measured and is described by Hegeman [4] as follows:

1. Light is emitted by white light source (or laser) and passes through the illumination pin hole.
2. After leaving the beam splitter, the beam is focused on the surface by the objective lens (solid line in Figure 2.4 indicates when specimen is focused and dashed when it is out of focus).
3. The reflected light passes back through the objective lens to the beam splitter.
4. Light is collimated by the confocal pinhole in the detector.

Chromatic confocal microscopy is a method of measurement that uses a confocal probe and lateral scanning apparatus. The confocal probe measures height (*z*-direction) and related light intensity while an optional stage allows line profile measurement (motion in the x-axis) or areal surface (motion in *x*- and *y*-axis). The chromatic probe method differs from the optical method by replacing the objective of the microscope with the chromatic objective and replaces the photo-detector with a spectrometer [53]. Theoretically, the chromatic confocal system is basically an optical profilometer similar to a stylus profilometer.

2.2 GRINDING WHEEL TOPOGRAPHY MODELS

Modeling of the grinding operation requires the consideration of the grinding wheel topography. Understanding the geometry of the individual abrasive grains, which are stochastically distributed and oriented on the grinding wheel surface leads to a better understanding of the dressing and grinding process. Typically, there are two principal strategies to obtain a topography model for a grinding wheel: i) using scanned information from a real grinding wheel surface topography, and ii) modeling the surface topography. In this chapter, existing grinding wheel models will be reviewed followed by a summary of the limitations of the current modeling methods.

There are two main types of models: empirical and physical. *Empirical models* use parameters that are computed mainly through statistical regression of experimental data. *Physical models* use parameters that are independent of the application and are more physically based. Additionally, grinding wheel topography models are categorized into three main types: one-dimensional (1D), two-dimensional (2D) and three-dimensional (3D). The main focus of this section is on two- and three-dimensional modeling techniques.

2.2.1 One-Dimensional Models

One-dimensional models are not covered in this thesis because they are unable to provide topographical details of the wheel surface. In general, the wheel surface is characterized by parameters such as surface roughness and the number of cutting edges that are exposed on the wheel surface [54]. In regards to the cutting edges, Verkerk *et. al* defined that cutting edges that are on the same grain (or near neighboring grains) may be considered as a single cutting edge since they do not have the chip clearance needed for chip formation [55].

2.2.2 Two-Dimensional Models

The majority of existing models falls into the two-dimensional modeling category. In two-dimensional models, the grains are described geometrically rather than empirically. In this modeling method, the grain size distribution, placement of the grain, and resulting protrusion height are commonly investigated [7], [8], [54]. The models covered include these by: i) Chen and Rowe [7], ii) Koshy *et al*. [8], and iii) *Baseri et al*. [56].

2.2.2.1 Chen and Rowe Model

Chen and Rowe [7] developed a physically-based predictive model to simulate the surface topography of grinding wheels during single point dressing. The dressing diamond is assumed to be parabolic shaped and the abrasive grinding grains in the model are assumed to be spherical grains with the diameter d_g calculated by [57]

$$d_g = 15.2\, M^{-1} \tag{2.3}$$

where *M* is the mesh size used in the manufacturing process of the grinding wheel. The evenly sized grains are then initially arranged in a simple cubic unit cell as illustrated in Figure 2.5.

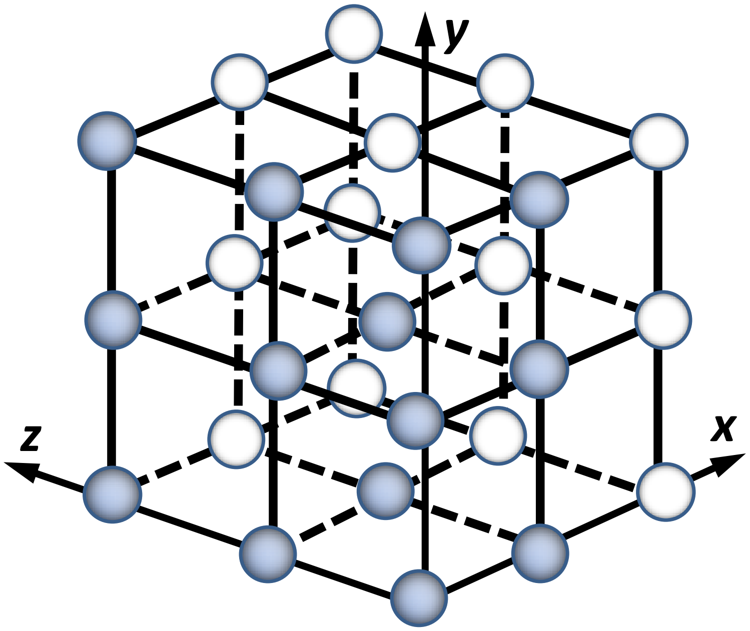

Figure 2.5 – Chen and Rowe's initial orientation of grains for simulation of grinding [7]

The grains are then three-dimensionally translated to a uniformly random placement within the grinding wheel using a geometric transformation as follows:

$$\left[G_{i,j,k}\right] = \begin{bmatrix} G_{i,j,k}^{x} \\ G_{i,j,k}^{y} \\ G_{i,j,k}^{z} \end{bmatrix} = \begin{bmatrix} G_{0,0,0}^{x} + i\Delta x + R_x \\ G_{0,0,0}^{y} + j\Delta y + R_y \\ G_{0,0,0}^{z} + k\Delta z + R_z \end{bmatrix} \tag{2.4}$$

where the spacing in *x,y,* and *z* directions are given by an average spacing of *Δx = Δy = Δz = Δ*. Spacing *Δ* is calculated from the density of grains in the grinding wheel and is mathematically expressed as

$$\Delta = \left(\frac{\pi d_g^3}{6V_g}\right)^{\frac{1}{3}} \tag{2.5}$$

where the grain volume packing density *Vg* is given by:

$$V_g = 2(32 - S) \tag{2.6}$$

with *S* representing the grinding wheel's structure number. R_x, R_y, and R_z are the random distances in the respective orientations and have values between zero and the spacing calculated in Equation 2.5. The total volume of the grains in one cell is calculated by

$$V_{g,SC}^{cub} = \frac{1}{6}\pi d_g^3 \tag{2.7}$$

To prevent granular overlap, the condition

$$d\left(G_{i,j,k}, G_{i',j',k'}\right) > d_g \tag{2.8}$$

must be satisfied where $d(G_{i,j,k}, G_{i',j',k'})$ is the distance between the centers of neighboring abrasive grains of the simulated grinding wheel.

The model takes the dressing diamond-to-wheel interaction into consideration when mapping the final contour of the grinding wheel as illustrated in Figure 2.6. The shape of the abrasive grain after dressing is considered random and is based on the geometry of the dressing tool due to fracture of the grains on the wheel surface [7]. Figure 2.6a represents an undressed grinding wheel illustrating the expected dressing trace that the dressing diamond will follow. Figure 2.6b then illustrates the actual topography contour versus the expected dressing trace. The model follows actual experimental results more accurately by taking bond cutting and grain fracture into consideration as well.

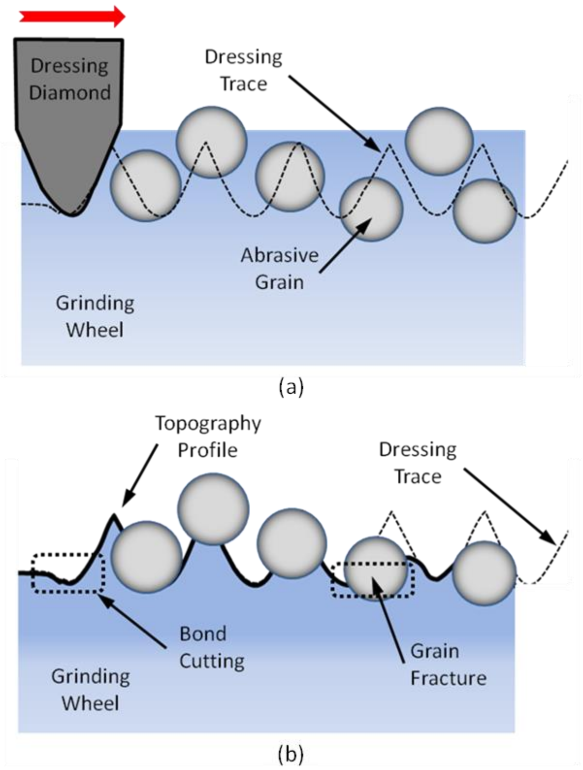

Figure 2.6 – Diagram of Chen and Rowe simulated grinding wheel surface. (a) undressed wheel topography, (b) dressed wheel topography [54]

The dressing tool follows a periodic function along the x-axis, $z_g(x)$, mathematically expressed as

$$z_g(x) = f(x) + h[\sin(\omega x + \alpha) + 1] \tag{2.9}$$

where the function $f(x)$ is the grain surface resulting from the diamond dressing path. The rest of the equation is the sine wave function with the random frequency ω (fracture frequency) and random initial angle α (fracture angle) superimposed on the cutting edge shape. The amplitude of the sine wave h is the degree of grain fracture and is expressed as

$$h = k\frac{A_{dg}U_d}{f_d} \tag{2.10}$$

where A_{dg} is the cut area of one dressing pass representing the cross sectional area of the diamond engaged in the grain and U_d is the overlap ratio. The proportionality factor k is chosen by trial and error to match simulation to experimental results. The final simulated grinding wheel surface profile is illustrated in Figure 2.7.

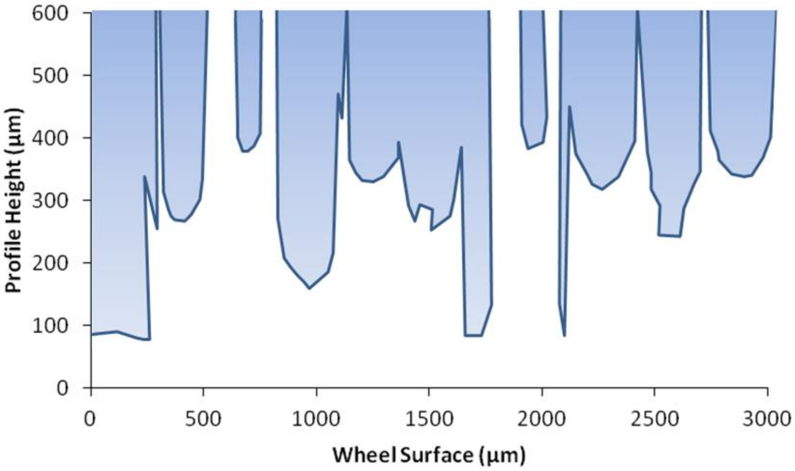

Figure 2.7 – Example of final simulated wheel surface contour from Chen and Rowe's model [7]

2.2.2.2 Koshy *et al.* Model

The two-dimensional model developed by Koshy et al. [8] is an expanded version of their one-dimensional model [58]. This model involves a stochastic simulation of a metal/resin-bonded diamond grinding wheel to predict the static planar grain density, which is the percentage area due to the abrasives on the wheel surface, and the abrasive protrusion height distribution.

The shapes of the grains are assumed to be spherical and the diameters of the grains are assumed to follow a Gaussian distribution about the mean abrasive grain diameter. The simulated abrasive diamond grains are randomly distributed in the volume of a cube representing the bond material with side l as illustrated in Figure 2.8. The x, y, and z coordinates of each grain center is uniformly distributed between (-0.1 d_g) and (1+0.1d_g). It is necessary to ensure that grain overlap does not occur and this is accomplished using Equation 2.11 where j is from 1 to i - 1.

$$\sqrt{(x_i - x_j)^2 + (y_i - y_j)^2 + (z_i - z_j)^2} \geq \frac{d_{gi}+d_{gj}}{2} \tag{2.11}$$

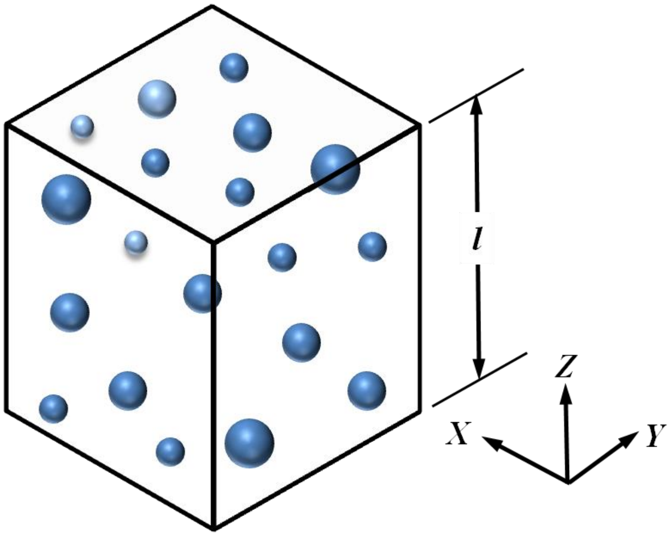

Figure 2.8 – Koshy *et al*. schematic representation of the simulated grinding wheel structure [8]

The diamond grains above the surface are identified and must satisfy the following condition [8]

$$abs(H - z_i) < \frac{d_g}{2} \tag{2.12}$$

The protrusion height P_h of an exposed grain, as shown in Figure 2.9 is defined by

$$P_h = z_i + \frac{d_g}{2} - H \tag{2.13}$$

where H is the bond surface height and z_i is the vertical height component of the grain center . The main output of the model is the distribution of the diamond grain protrusion height of a dressed wheel, which is shown to be uniform and the spacing between the exposed grains is shown to follow a gamma distribution.

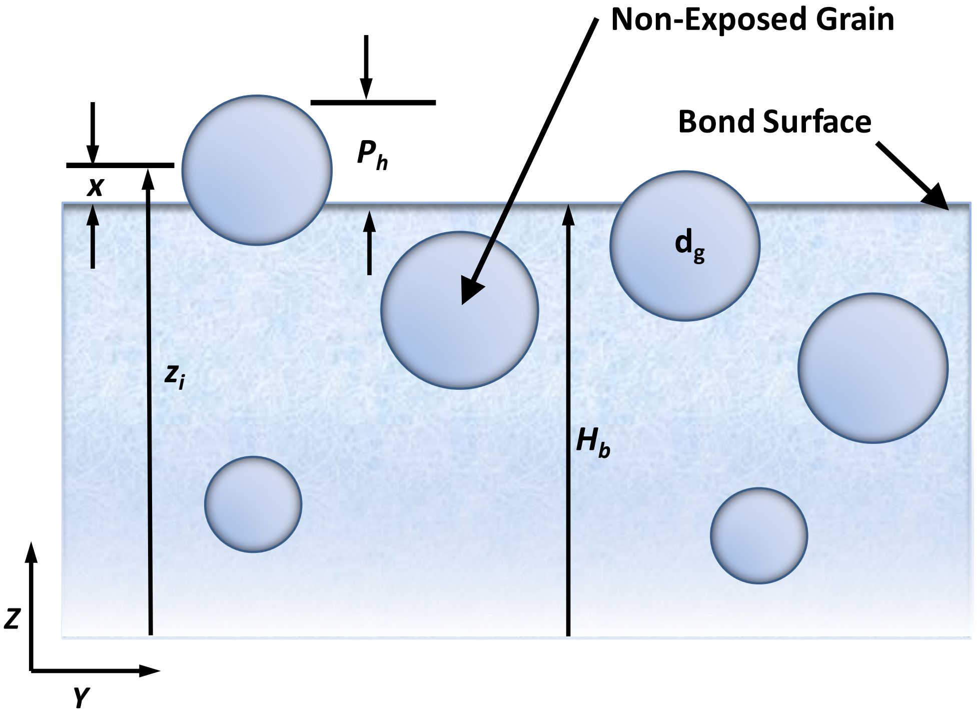

Figure 2.9 – Koshy *et al*. scheme for identifying protruding abrasive grain [8]

2.2.2.3 Baseri *et al*. Model

Baseri *et al*. [56] developed a model to predict the grinding wheel surface topography by a diamond disc dresser. The main output of model is the number of active grains per unit area and the average slope of grains in the grinding wheel. The model assumes that the grains are of spherical shape their size follows a Gaussian distribution.

The abrasive grains are randomly distributed in the bond material with coordinates (x_m, y_m). The initial step in their model is to calculate the number of grains in the area of concern by first calculating the grains per unit length using [56]

$$N_l = \frac{{V_g}^{1/3}}{d} \tag{2.14}$$

where d is the mean grit diameter and Vg is the volume fraction of grit in the wheel, which is calculated using [57]

$$V_g = 2(32 - S)\% \tag{2.15}$$

where S is the structure number of the wheel. It is assumed that the grains of diameter d are located initially in uniform distribution as shown in Figure 2.10.

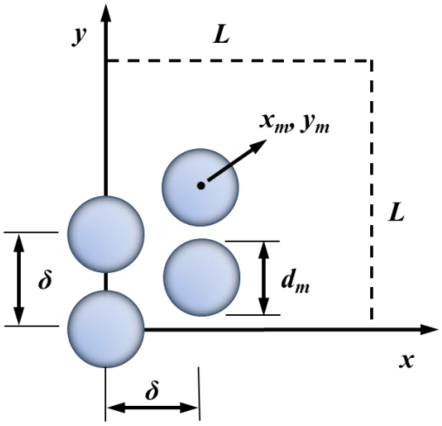

Figure 2.10 – Baseri *et al*. initial layout of abrasive grains on the wheel [56]

The distance between the grains is given by

$$\delta = \frac{1}{N_l} \tag{2.14}$$

The coordinates of each grain in a square of side L of the wheel section are given by

$$x_m = i\delta + R_x \tag{2.15}$$

$$y_m = y_0 + j\delta + R_y \tag{2.16}$$

where i and j are between 0 and the integer value of L/δ. Rx, Ry are random numbers between 0 and δ - d. The variable y_0 is zero when i is even and it is $\delta/2$ when i is an odd number. This algorithm creates the needed cross hatch grain pattern of abrasive grains. A MATLAB program was used to determine the random grain sizes and their coordinates resulting in a spatial distribution similar to Figure 2.11.

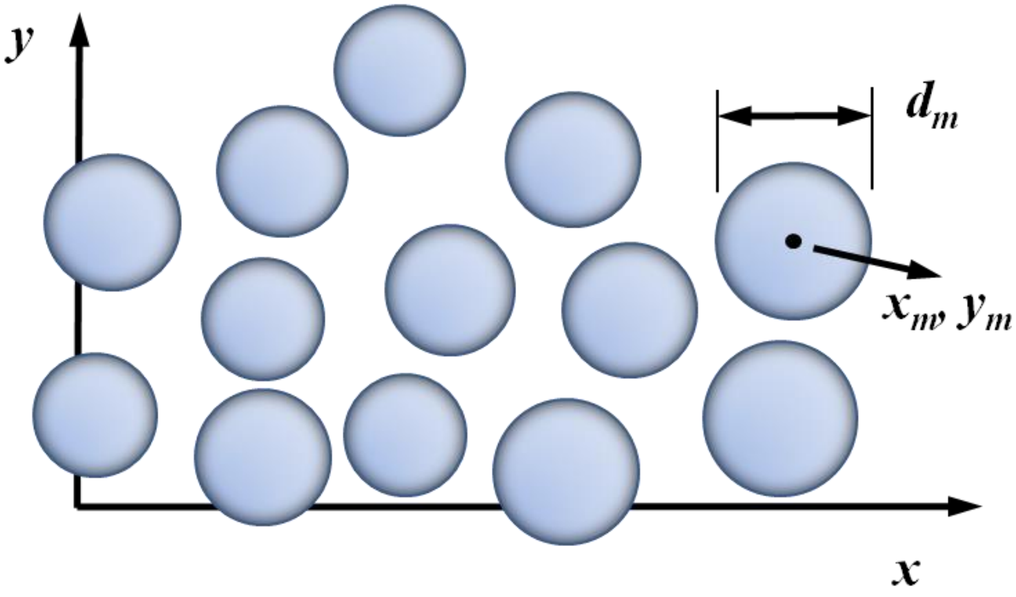

Figure 2.11 – Baseri *et al*. abrasive grain layout after randomized placement and sizing [56]

A dressing model is then applied to the simulated undressed grinding wheel surface topography to simulate the post-dressed surface topography. The model used is a modified version of Chen and Rowe's model [7] to create a sinusoidal surface with random surface mathematically represented by

$$Y_f = Y_d + \left[e_1 \cdot a_g^{e2} \cdot s_d^{e3} \cdot q^{e4} \cdot (1 - P_b)\right](\sin(\psi x) + 1 \qquad (2.17)$$

where e_1, e_2, e_3, and e_4 are constants and ψ is a random frequency given as

$$\psi = \frac{5\pi}{d_m} \qquad (2.18)$$

These five parameters are determined by matching the simulated and experimental results of surface roughness. Y_d is the dresser tip trace, which is mathematically represented by

$$Y_d = y_k + \sqrt{r^2 - (x - x_k)^2} \qquad (2.19)$$

where r is the dresser tip radius and (x_k, y_k) represents the wheel coordinate system of the center of the dressing tip. The x coordinate is expressed as

$$x_k = [0.5 + int\left(\frac{x}{s_d}\right)]s_d \qquad (2.20)$$

$$x_k = a_d - r \qquad (2.21)$$

with s_d is the cross-feed rate of the dresser and a_d is the depth of cut of the dressing tool. The modeling of the interaction between the rotary dresser and the surface of the grinding wheel then considers the probability of bond fracture based on the work by Peklenic *et. al* [59]. The model is then applied to an alumina wheel to simulate the surface shown in Figure 2.12.

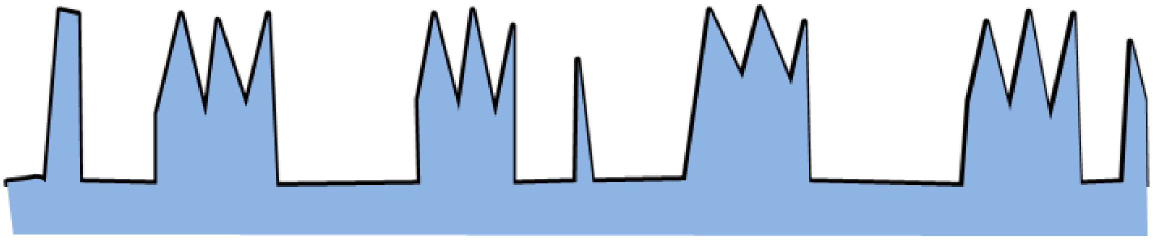

Figure 2.12 – Baseri *et al*. simulation of dressed wheel surface [56]

2.2.3 Three-Dimensional Models

In three-dimensional models, not only the grain position and shape are described as three-dimensional objects, but the simulated wheel surface topography is represented in three-dimensions [54]. The previous models have used volumetric information for input into their topography model but yield only two-dimensional outputs such as that shown by Chen and Rowe in Figure 2.7 and by Baseri *et al*. in Figure 2.12. The three-dimensional topography models discussed in this section include the work by i) Hegeman [4], ii) Feng et al. [60], and iii) Darafon [51]. Three dimensional models including simulation of dressing are very limited and the only one found in this literature review was by Darafon [51] while the other two were included since three-dimensional simulation of grinding wheel surface topography is limited.

2.2.3.1 <u>Hegeman Model</u>

Hegeman [4] developed a model to predict the grinding wheel topography by randomizing the arrangement of three-dimensional ellipsoidal grain geometries simulating a diamond grinding wheel. This model is one of the earliest works to simulate the resulting grinding wheel surface in three-dimensions. The grain geometrical shape function in the grinding wheel global coordinate system is mathematically represented as

$$x^{gr}(x,y) = r_g^z \sqrt{1 - \left(\frac{x - x_g^c}{r_g^x}\right)^2 - \left(\frac{y - y_g^c}{r_g^y}\right)^2} \tag{2.22}$$

where $(x_g^c, y_g^c, z_g^c = 0)$ is the grain center location and r_g^x, r_g^y, and r_g^z are the grain axis radii in *x*, *y*, *z* directions, respectively. The randomized simulated texture and shape of the abrasive diamond grain is then additionally controlled by the periodic function to simulate the effect of dressing by using

$$z^{fr}(x,y) = \cos(\widehat{\omega_x}x + \widehat{\alpha_x}) + \cos\left(\widehat{\omega_y}y + \widehat{\alpha_y}\right) \tag{2.23}$$

where $\widehat{\omega_x}, \widehat{\alpha_x}, \widehat{\omega_y}$ and $\widehat{\alpha_y}$ are random numbers with the wheel surface located on the plane of $z = 0$. A stochastic model of the wheel topography is created using information obtained from measurements given in Table 2.1. The main measurement equipment used are a scanning electron microscope (SEM) and a confocal optical microscope. The confocal microscope was mainly used to characterize the diamond grains while the SEM was used to determine the grain density of the grinding wheels.

Table 2.1 – Required wheel parameters for Hegeman model [4]

Parameter	Symbol	Acquisition Method
Grain Density	C_A	Scanning Electron Microscope
Grain Base Radius	$r_g^x = r_g^y$	Confocal Scanning Optical Microscope
Grain Protrusion Height	r_g^z	Confocal Scanning Optical Microscope

A Monte Carlo approach was used to place the grains on the simulated grinding wheel surface in a two-dimensional lattice layout as illustrated in Figure 2.13. The grains are placed within the lattice cells at a random location within the dimensions l_x and l_y. To prevent geometric overlap, it is assumed that only one grain occupies each cell.

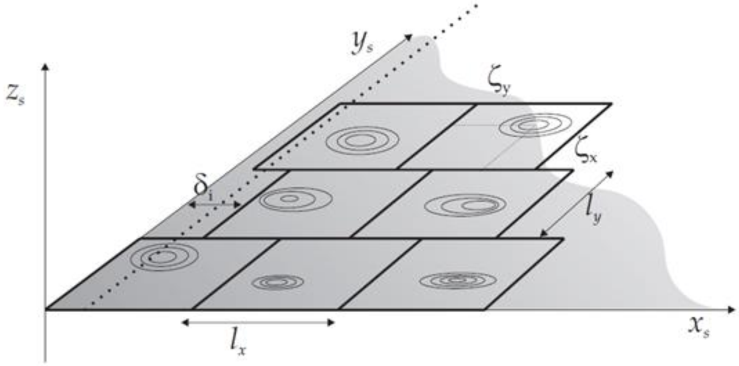

Figure 2.13 – Random lattice for grain placement in Hegeman model [4]

Combining the protrusion height and spatial distribution of the grains result grains in the simulated grinding wheel surface is shown in Figure 2.14. The main objective of the model was to simulate the interaction of the diamond grinding wheel and the workpiece surface but does not include dressing.

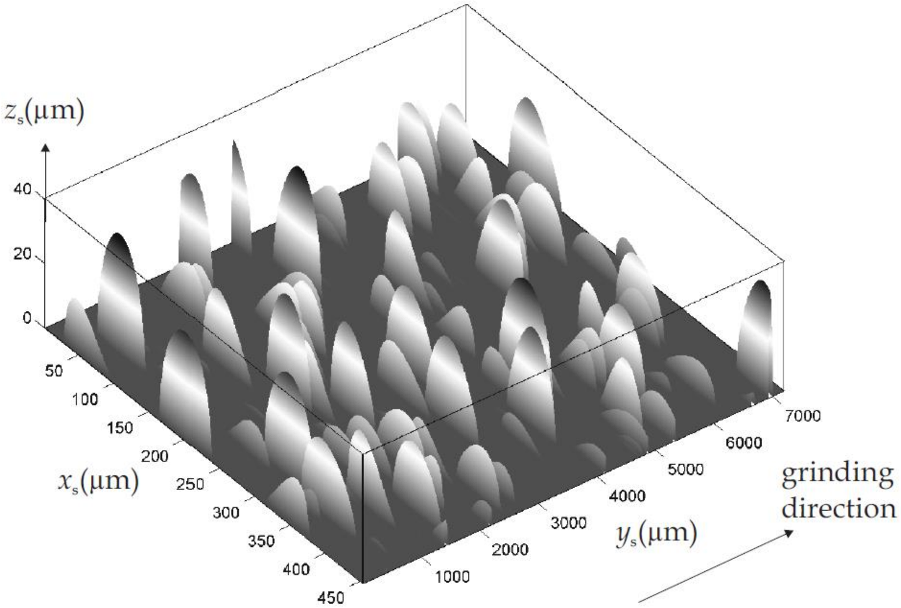

Figure 2.14 – Simulated surface topography of Hegeman model [4]

2.2.3.2 Feng *et al*. Model

Feng *et al*. [60] developed a model to simulate the three-dimensional grinding wheel surface topography. The abrasive grains in the grinding wheel were modeled as conical grain tips embedded in a bonding material. The model considered wheel structural properties, grain shape, angle distributions of the cutting edges, and bonding material. It is assumed that the abrasive grain tips follow a normal distribution in the height direction. The main output of the model is a three-dimensional map of the wheel surface. The effects of dressing are not considered in the simulation of the grinding wheel.

The grains are modelled as a conic shape as shown in Figure 2.15. The tip of the grain is simulated as a taper to include both the angle and diameter of the abrasive grain used in the model using the following equation

$$x^2 + y^2 = \tan^2\theta \cdot \left(\frac{d}{2} - z\right)^2 \quad \text{with} \quad \left(\frac{d \cdot \tan^2\theta}{2(\tan^2\theta + 1}\right) \le z \le \frac{\mathrm{d}}{2} \qquad (2.24)$$

where the cutting edge angle *2θ* follows a Gaussian distribution given by

$$f_c(\theta) = \frac{1}{\sqrt{2\pi\sigma_c}} e^{\frac{1}{-2\sigma_c^2}(\theta - \bar{\theta})} \qquad (2.25)$$

where σ_c and $\bar{\theta}$ are related to the friability of the abrasive grain crystal structure and the grinding condition.

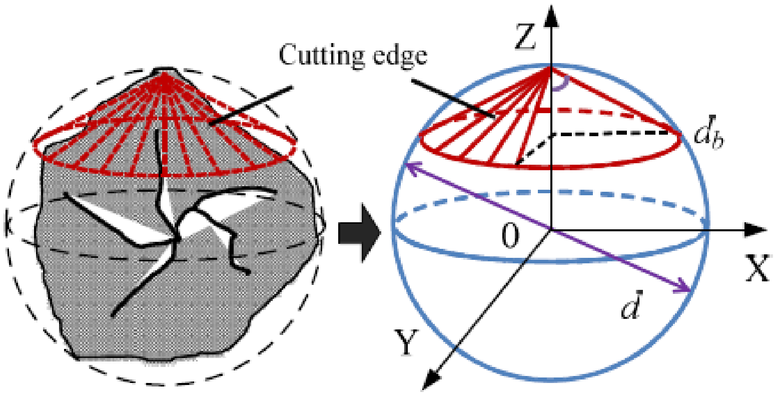

Figure 2.15 – Conic model for shape of cutting edge on the grain of Feng *et al*. model [60]

The protrusion height (*z*-direction) of the abrasive grain follows a Gaussian distribution and the grain centers are initially placed on a two-dimension lattice structure as shown in Figure 2.16 and then randomly translated in the *x*- and *y*-directions using the following equations

$$x_0 = r_x S_g/2 \tag{2.26}$$

$$y_0 = r_y S_g/2 \tag{2.27}$$

where x_0 and y_0 are the grain center coordinates, r_x and r_y are random numbers equally distributed between -0.5 and 0.5, and S_g is the average distance between two adjacent grains.

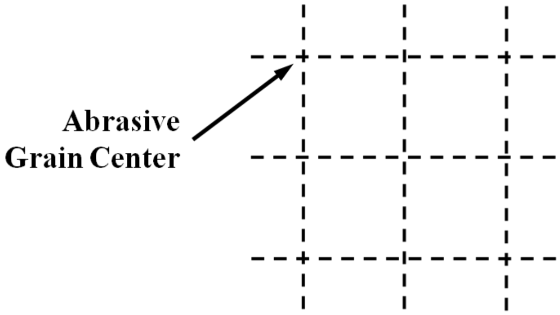

Figure 2.16 – Grain layout of Feng *et al*. model [60]

The unique model created by Feng *et al* simulates the bonding material as shown in Figure 2.17. The grain-in-bond curve is indicated by the red line and is determined by the grain peak *C*, grain center *B*, and transition between the bonding material and grain *E*. The sinusoidal curve function representing the bond surface is mathematically given by

$$z(x) = -A \cdot cos\left(\frac{2\pi}{S_g} \cdot x\right) + c \tag{2.28}$$

where c is the distance between grain center and the origin ($c = z - d$), A is the amplitude ($A = d/2 - c$) and z is the height of the grain tip.

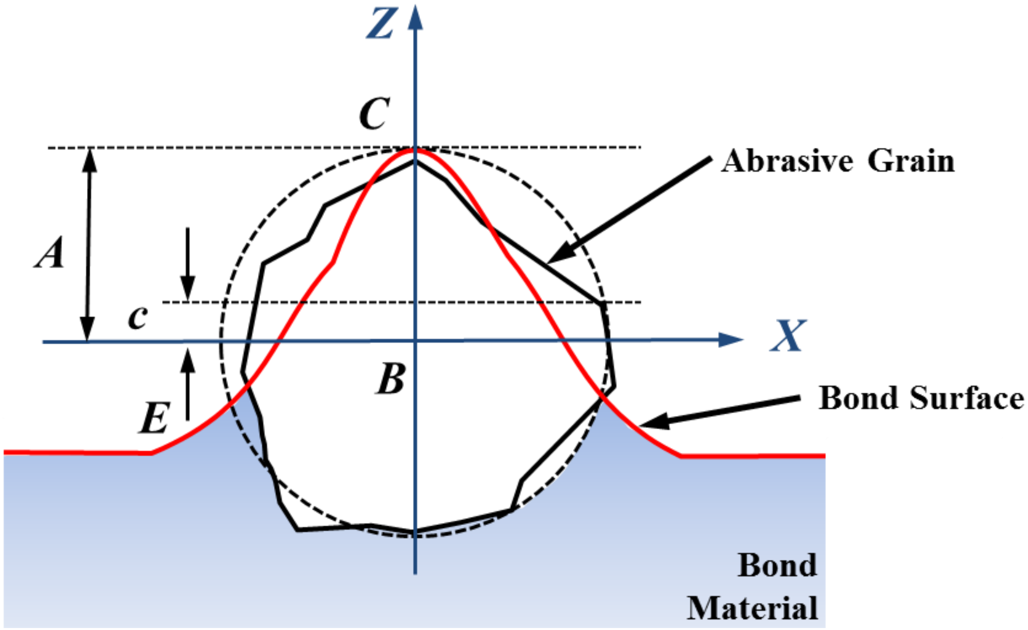

Figure 2.17 – Bond creation in Feng *et al*. model [60]

Figure 2.18 shows the simulated three-dimensional grinding wheel topography created by the model. Figure 2.18a illustrates the grain placement of the simulated surface and Figure 2.18b is the resulting three-dimensional surface with the addition of the bonding.

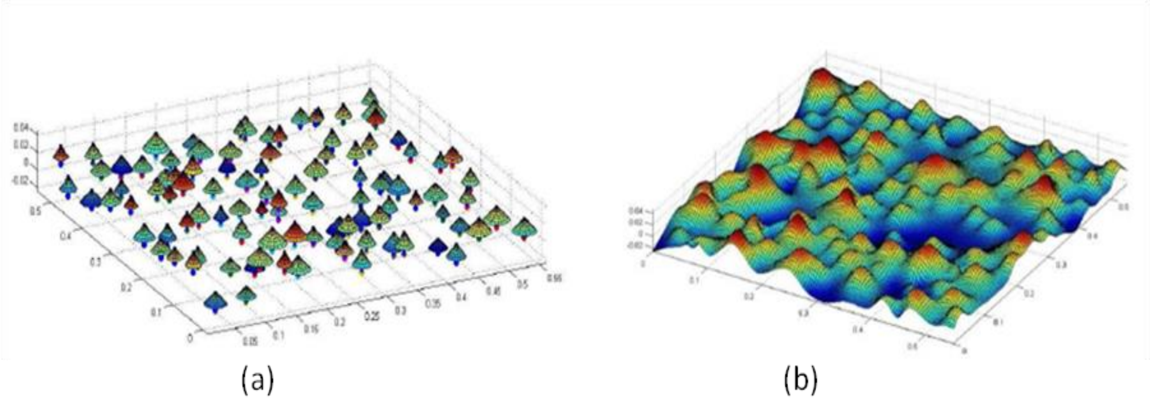

Figure 2.18 – Simulated wheel topography of Feng *et al*. model. (a) topography with conic grains, (b) topography with bonding material [60]

2.2.3.3 Darafon Model

Darafon [51] recently introduced a three-dimensional wheel surface topography model that stochastically maps the surface of an aluminum oxide grinding wheel based on a modified version of the model by Koshy *et al*. [8]. In this methodology, the abrasive grains are packed within the volume instead of just the surface area of the grinding wheel, as illustrated in Figure 2.19, to achieve the initial grain packing density. The figure on the left illustrates the initial configuration of the grains obtained by Equation 2.3 and the figure on the right shows how the grains appear when spacing is randomly changed as shown in Figure 2.8. If a grain interferes with another grain or is outside the wheel's boundary, it is moved back until it touches the other grain or the wheel border via a process known as the *shaking process.* This is continued until the grain distribution is as homogenous as possible as shown on the right side of Figure 2.8.

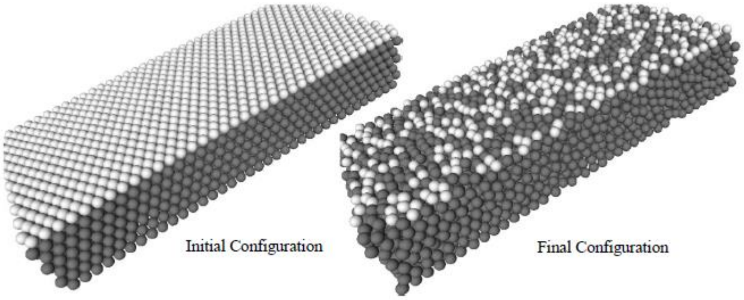

Figure 2.19 – Grain packing of Darafon model [51]

In this model, the grain protrusion height is assumed to follow a uniform distribution and the spatial separation is assumed to follow a gamma distribution while using the *shaking process*. After the grains have been "shaken," the grain size is adjusted to account for the actual (normal) distribution of grains typically found in grinding wheels [8], [61] and then converted to a grinding wheel shape as shown in Figure 2.20.

Grain packing resulted in a number of grains with corresponding sizes and locations in three-dimensions. This information is then used to create the three-dimensional wheel model as shown in Figure 2.20. It is first necessary to section the wheel with the cutting plane as illustrated in Figure 2.20 to generate a two-dimensional slice of the simulated grinding wheel.

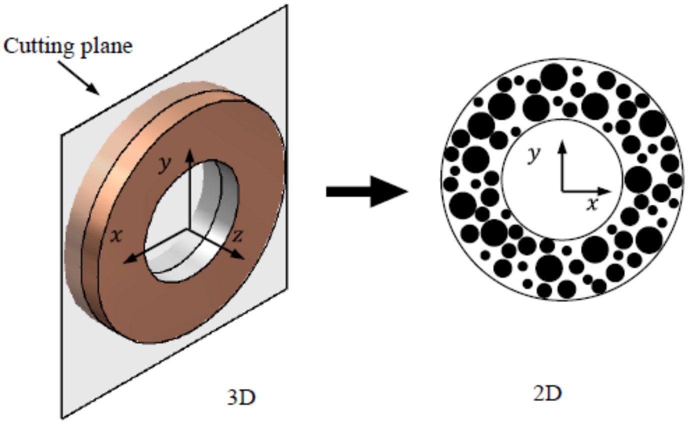

Figure 2.20 – Grinding wheel grain packing of Darafon model [51]

Each slice of the grinding wheel must satisfy

$$R_g + \frac{d_g}{2} > H \tag{2.29}$$

where H is the minimum surface height and R_g is the distance between the grain center (x_c,y_c) and the wheel center (0,0) and can be calculated by

$$R_g = \sqrt{x_c^2 + y_c^2} \tag{2.30}$$

The periphery of the grinding wheel is simulated using the equation

$$y = \max\left(\sqrt{H^2 - x^2},\ \ y_c^i + \sqrt{\left(R_g^i\right)^2 - \left(x - x_c^i\right)^2}\right) \tag{2.31}$$

where i is the exposed grain number and the other variables are illustrated in Figure 2.21. The resulting two-dimensional profile results in a cylindrical shape as shown in Figure 2.21b with point P(x_p,y_p) which has a polar coordinate of (R_p,θ_p).

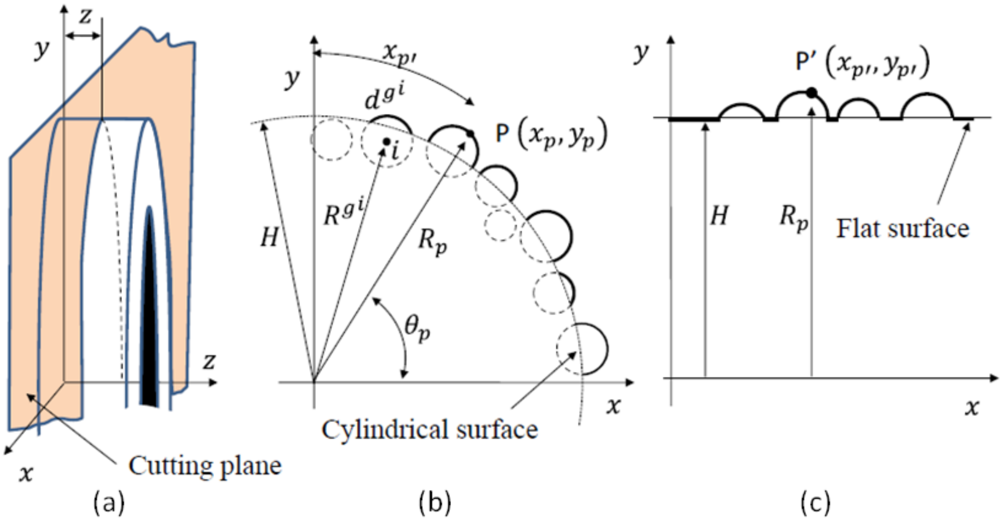

Figure 2.21 – Converting from cylindrical surface to flat surface in Darafon model [51]

The final step is to convert the cylindrical profile into a straight profile as shown in Figure 2.21c using the equations

$$x_{p\prime} = R_p \; X \; \theta_p\left(\sqrt{x_p^2 + y_p^2}\right) \tan^{-1}\left(\frac{x_p}{y_p}\right) \tag{2.32}$$

$$y_{p\prime} = R_p \tag{2.33}$$

The *z* component of all points in each cutting plane is the distance between the cutting plane and the x-y plane. Figure 2.22a shows an example of a 2mm x 2mm patch of the converted surface of the grinding wheel in three-dimensions before the dressing operation.

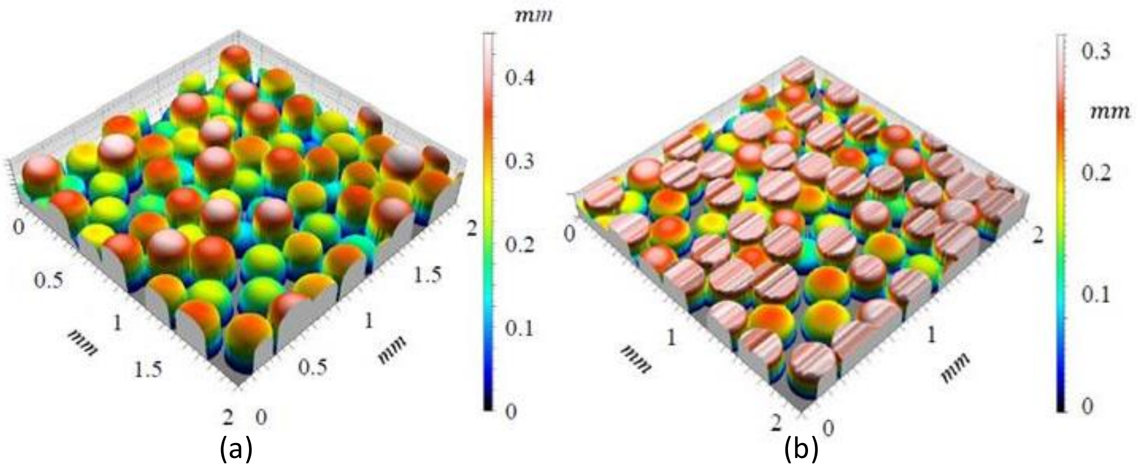

Figure 2.22 – Darafon model simulated wheel topography. (a) undresesd wheel, (b) dressed wheel with medium dressing condition [51]

A simulated dressing process is applied to the simulated wheel surface using a modified dressing model presented by Chen and Rowe [7] to create the surface shown in Figure 2.22b. This model was used to calculate both the amplitude and the frequency of the fracture of the individual grinding grains.

2.3 DEFICIENCIES

2.3.1 Measurement Methods

Measurement of surface features is broken into two main categories of contact and non-contact methods. The correct measurement method has a large impact on the entire analysis when analyzing microscopic surface features [45].

2.3.1.1 Contact Measurement

In the world of measurement techniques, the term *contact measurement equipment* usually refers to systems that use a stylus that mechanically traces the profile of the surface. Multiple wheel surface topography measurement and characterization techniques have been employed in the past including two-dimensional [56], [62] and three-dimensional [35], [36], [39], [63] stylus surface profilometry, which generally result in low resolution of the surface and also suffer from limitations of contact metrology [23].

Stylus profilometry methods are capable of measuring the profile shape of grinding wheel and detecting the shape, but have flaws such as slow detection speed, low accuracy, and the styli are easily damaged by the hard and abrasive materials that will affect the measurement accuracy by distorting the data [51]. The wear on the tip acts as a low pass filter, preventing asperities that are smaller than the radius of the tip being accurately resolved as illustrated in Figure 2.23 [23]. The main drawback of 3D stylus instruments is time. Measurement times are extremely high, a 4 x 4 mm area with a 1000 x 1000 point matrix may take as much as 3 hours to complete. Finally, some additional unavoidable source of errors in both methods is the conversion of the mechanical signal (given by the stylus tip) to the electrical signal during the trace along with the conversion of this continuous, analogue signal to a digital input into the computer software [34].

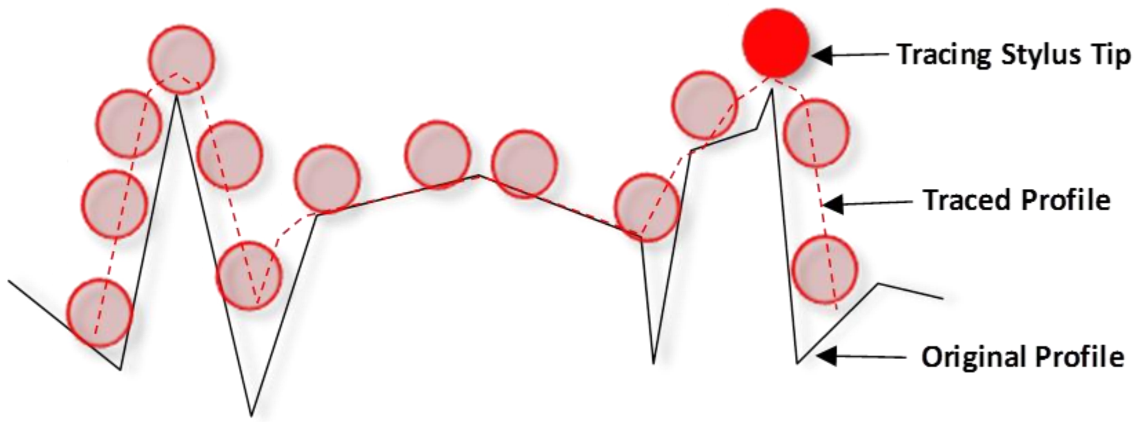

Figure 2.23 – Effect of stylus tip radius on measurement results [23]

2.3.1.2 Non-Contact Measurement

Non-contact measurement methods summarized in this chapter range from conventional optical microscopes to advanced white light interferometric methods. Measurement instruments have finite vertical and horizontal measurement ranges for optimum use and certain aspects of their physical properties (probe size and geometry, transducer sensitivity, movement error scan length, datum, scale resolution etc.) also limit their range of measurement [34]. The following section explains the limitations of the different metrology methods and offers a new technique that has not been reported to measure surfaces of SG grinding wheels.

Although the reviewed non-contact methods seem to be more suitable for the measurement of the grinding wheel topography, all the non-contact techniques (with the exception of the work by Weingaertner and Boaron [43] and Lachance *et al*. [45] and Darafon [51]) have restrictive measurement volumetric boundaries to measure an entire grinding wheel surface. These methods measure only very small grinding wheels or require the destructive testing of grinding wheels making their use impractical. Hedgemen [4] experimented with over coming this limitation by using the imprint methods without success. He experimented with Tecnovite 4000 which consisted of polyester resin and anti-shrinking powder with particles of approximate diameter of 1µm in attempts to extract parameters to measure the surface of the grinding wheel. This method proved to be unsuccessful to determine individual grain shape descriptors but could acquire some parameters such as grain concentration.

2.3.2 Modeling Methods

Throughout the history of studying grinding wheel, there have been many models introduced to simulate the surface of grinding wheels. It is important to accurately represent the surface topography of the grinding wheel for the most accurate output of the simulation. Measuring the whole grinding wheel is a time-consuming activity while a realistic analysis of the grinding process requires a large amount of wheel surface measurements to accurately represent the grinding wheel. The main emphasis of the literature review was on two- and three-dimensional modeling methods.

The two-dimensional work covered include models by Chen and Rowe [7], Koshy *et al.* [8], and Baseri *et al.* [56]. A two-dimensional modeling method is limited based on the definition presented earlier by Doman that the resulting topography is two-dimensional such as that illustrated in Figure 2.7 and Figure 2.12. Three-dimensional models yield a more realistic output of the wheel surface. The three-dimensional topography models discussed in this section include work by Hegeman [4], Feng *et al.* [60], and Darafon [51].

Independent of dimensions, there are certain attributes of existing models that need to be improved to more accurately represent the wheel including i) geometry of the abrasive grain, ii) simplified distribution assumptions, iii) limited number of models representing vitrified bonded seeded-gel (SG) or even conventional aluminum oxide grinding wheels.

Understanding the geometry of individual abrasive grains, which are stochastically distributed and oriented on the grinding wheel surface will lead to a better understanding of the dressing process. The shape of the abrasive grain is an important factor during the dressing process resulting from the interaction of the dressing. Blocky (or a spherically shaped tip) will need more force to penetrate a surface and will be less likely to fracture compared to a higher-angled jagged shaped tip [64].

Many researchers have modeled the surface of the grinding wheel using simple shape abrasive grains [8], [65]–[67]. Cooper and Lavine [65] modeled the abrasive grain as a truncated cone while Warnecke and Zitt [66] meshed the grinding wheel surface with polyhedrons. Other researchers preferred representing the abrasive grains as spheres [8], [68]–[70]. The main advantage of using simplified geometry is that the information required for the simulation (such as nominal diameter of the abrasive grains, distance between grains) can be easily calculated from the grinding wheel specification. This over simplification overlooks the fact that the shape of the abrasive grains is often very complex in actual grinding wheels.

Regardless of the grain shape, the location of the grain is important and needs to be placed accurately in the volume of the grinding wheel. The placement of the grain in the volume of the grinding wheel depends on many factors including the type of grain, bond type, and structure of wheel. The stochastic nature of the grain placement are divided into two main categories including along the *z*-axis (height distribution) and the *x*-,*y*-axis (spatial distribution). The majority of authors have assumed that the placement of the grain along the z-axis follows a Gaussian distribution [60], [71]–[73]. Spatial distribution has been assumed as discrete uniform random [4], [67] or simply evenly spaced in all three-dimensions [7], [74].

Recent efforts in three-dimensional grinding wheel surface characterization using non-contact optical scanning techniques focus on either conventional aluminum oxide [1]–[3] or super-abrasive wheels such as diamond [4]–[6] or CBN [7]–[12], [35] wheels. However, limited characterization work on seeded-gel grinding wheel surface topography has been reported. The models that concentrate on non-conventional wheels resulted in surface topographies similar to Figure 2.14 for a diamond resin bonded wheel and are not useful for conventional wheels with porous vitrified bonded abrasive grains. The dressing operation gradually removes the bond material from around the diamond resulting in an increase of the protrusion height above the surface of the grinding wheel. The diamond will dislodge when the grain is unable to be retained by the bonding material during the interaction of the dresser or workpiece material.

2.3.3 Generation of Grinding Wheel Surface Topography

The surface of the grinding wheel changes as a result of the interaction of the diamond dresser and abrasive grains. The technology of surface metrology has also advanced in recent years and now allows for more precise methods for measuring the complex surface texture of grinding wheels. Past studies often directly evaluate the effect of dressing conditions on the final ground workpiece roughness, bypassing the impact on wheel topography, and not explaining what is actually happening to the grinding wheel surface. Some of the models concentrate on the grinding forces [12], [35], [75] and the majority covered in the literature review concerning the workpiece interaction (workpiece surface roughness) [1], [29], [51], [56], [76]–[79]. The interaction of the grinding wheel surface topography is often overlooked since the dressing features are transferred to the workpiece surface, but cannot be easily detected on the wheel surface [7]. The wheel topography and the dressing conditions are important to consider is since they have a large influence on the grinding performance including the grinding forces, power consumption, cutting zone temperatures, and also the surface finish of the workpieces [36].

Few works covered in the literature review have covered the topic of understanding the generation of a seeded-gel (SG), or even also limited to conventional, wheel surface topography as a result of single point dressing to a great extent using advanced three-dimensional measurement instrumentation. Two, of the few, examples of researchers studying the change of the surface topography included work by Nguyen and Butler [35] and Darafon [51].

Nguyen and Butler [35] observed the effect of rotatory dressing on the surface topography of a CBN wheel by measuring the "coarseness" using *Sq* with a Talyscan 150 3D stylus system. Along with coarseness, the wheel was characterized as a function of density of summits *Sds* and summit curvature *Ssc* indicating the density of cutting edges and sharpness, respectively. More recent work by Darafon [51] studied the effects dressing feed of single point dressing on a conventional grinding wheel. Darafon concentrated on cutting edges formation (density, spacing, and protrusion height) using image processing techniques. The grinding wheel surface was measured using a white chromatic sensor acting as an optical three-dimensional "stylus" system.

2.4 SUMMARY

This chapter has reviewed existing research concentrated on the measurement and modeling of the surface topography of grinding wheels. Although some works have succeeded in mapping the wheel surface, the results have not been extended to realistically represent the grinding wheel surface after the interaction of the diamond dresser with the abrasive grains on the surface of the grinding wheel. After reviewing the past methodologies utilized to measure and model the resulting surface topography features, there appears to be a need for a system that measures the surface of the grinding wheel surface and then to accurately perform surface mapping and predicts the changes in the surface features in a realistic manner. From the above review and summary of past work, it can be concluded that:

- There is a need to investigate three-dimensional measurement methods to further characterizing grinding wheel surface topography.
- There has been limited work performed on using suitable measurement equipment to characterize seeded-gel (SG) grinding wheels including aspects such as:
    - Wheel: grain density, surface texture height, and grain spatial separation.
    - Grains: realistic shape and size.
- There has been limited work realistically modeling the surface topography of conventional-type grinding wheels using more advanced characterization information.
- There is a need to obtain a better understand how the three-dimensional surface topography transforms into a new surface during single point dressing operations and how the surface texture changes under different dressing conditions.

The rest of this thesis describes the development, experimental characterization, and modeling the surface topography of grinding wheels and how it changes during the single point dressing process.

3. CHARACTERIZATION

The effects of single point dressing on the surface topography of a seeded gel (SG) ceramic grinding wheel are investigated. First, new wheel and grain characterization techniques including X-ray micro-tomography (μCT) are introduced to obtain a better understanding of the micro surface topography of the SG grinding wheel. A special wheel indexing and relocation apparatus is designed and used to analyze changes in wheel surface topography at a given location before and after dressing. In addition, statistical distributions of the key parameters (e.g. grain density, grain size, grain protrusion, number of sides of grain, grain spacing) are determined and analyzed.

Multiple wheel surface topography measurement and characterization techniques have been employed in the past including 2D [56], [62] and 3D [35], [36], [39], [63] stylus surface profilometry, which generally result in low resolution of the surface and also suffer from the associated limitations of contact metrology [23]. Past studies often directly evaluate the effect of dressing conditions on the final workpiece roughness and bypass the impact on wheel topography, therefore not explaining what is actually happening to the grinding wheel surface [37]. Recent efforts on three-dimensional grinding wheel surface characterization using non-contact optical scanning techniques focus on either conventional aluminum oxide [1]–[3] or super-abrasive wheels such as diamond [4]–[6] or CBN [7]–[12]. However, limited characterization work on SG grinding wheel surface topography has been reported. In this chapter, three-dimensional characterization of a SG grinding wheel's micro topographical features such as the statistical distributions of grain protrusion, grain density, grain spacing and the modification of some of these characteristics during single point dressing is carried out using non-contact three-dimensional surface metrology. In addition, X-ray micro-tomography is used to characterize individual SG grain properties such as grit size distribution, grain shapes, and grain spacing. SEM was used to characterize distribution of number of sides (facets) and grain aspect ratio.

3.1 CHARACTERIZATION OF SEEDED GEL (SG) GRINDING WHEEL

Precision grinding wheels are often difficult to characterize due to the stochastic nature of abrasive grains, which are randomly placed on the wheel surface during manufacturing. The scanning electron microscope (SEM) image in Figure 3.1 demonstrates the complexity of the SG grinding wheel surface.

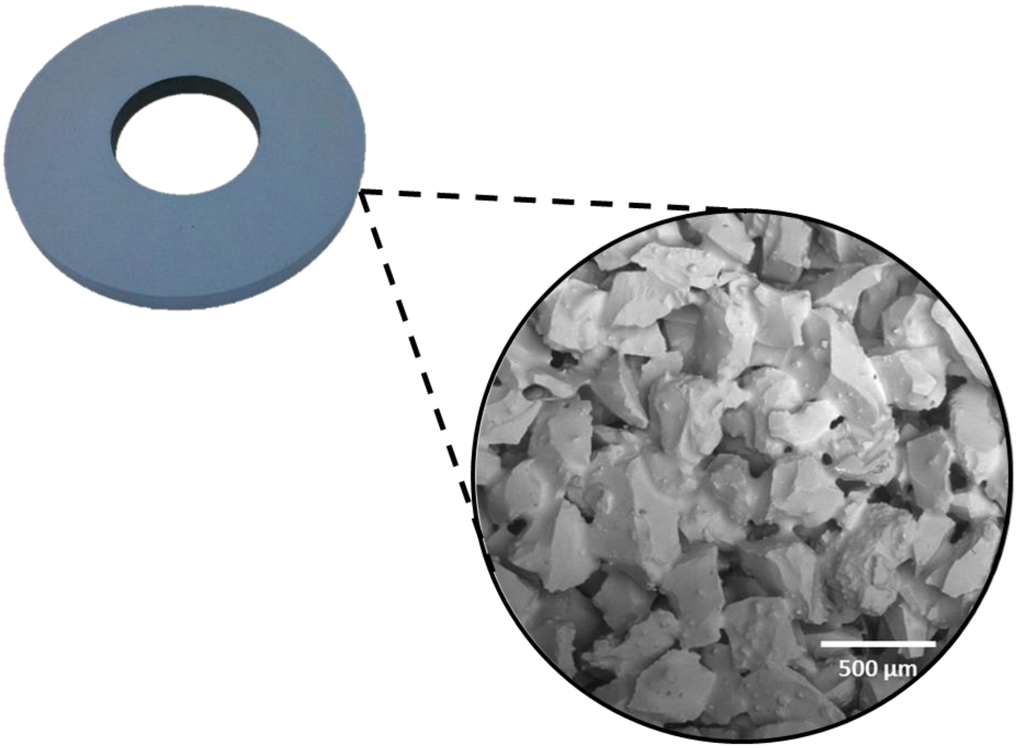

Figure 3.1 – SEM image of SG grinding wheel

This section focuses on static characterization of a vitrified bonded SG alumina grinding wheel (5SG60-KVS). Three main types of characterization instruments are used including optical surface metrology equipment (Alicona IFM G4g; specifications listed in Table 3.1), a scanning electron microscope (SEM, Hitachi S-3700N VP), and a GE Preclinical eXplore Locus micro-tomography (µCT) instrument (equipment and measurement services provided by ImageIQ). The wheel characterization is broken into two main components including characterization of the wheel surface and characterization of the individual grits/grains.

Table 3.1 – Experimental Measurement equipment characteristics

Parameters	Specifications
Instrument Type	Alicona IFM G4
Scanning Area	1.1579x2.8445mm
Scan Size	1232x1626 points
Sampling Distance	1.75 µm
Magnification	5x

The grinding wheel is made up of abrasive grains, bond material, and porosity. In this thesis, the SG grinding wheel characterization includes grain density (grains per unit area), grain height distribution, and grain spacing as illustrated in Figure 3.2.

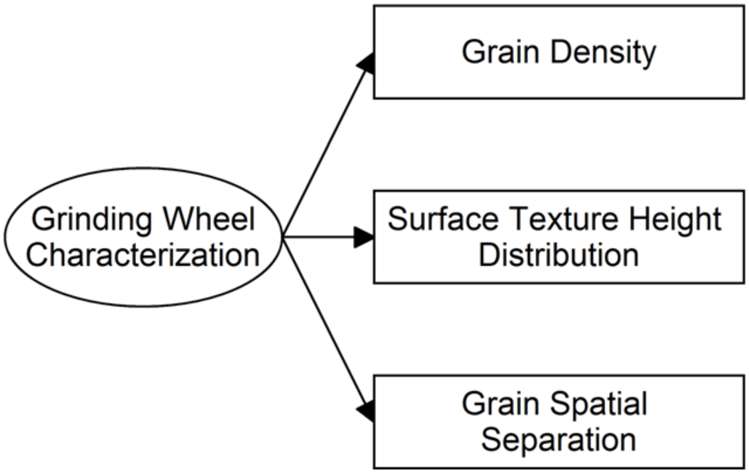

Figure 3.2 – Grinding wheel characterization attributes

3.1.1 SG Background Information

The concept of utilizing abrasive grains consisting of sub-micron size crystalline particles was introduced in the early 1980's by the 3M Company. The manufacturing process of the grain involves converting a colloidal dispersion or hydrosol containing goethite ($A1_20_3 \cdot H_20$) in a mixture with solutions or other sol precursors to a semi-solid gel to restrain the mobility of the components, drying to a glassy state, crushing to the required grain size, and firing at about 1300°C [80]. The 3M Company introduced this *sol-gel* under the trademark name of *Cubitron* and used it in coated abrasive fiber discs [81].

Norton modified and applied the new technology to create the current *SG* technology with application to grinding wheels by modifying the process by having the gel "seeded" with submicron alpha alumina particles before drying [80] to control the grain size. SG is created by first precipitating MgO to 50 nm sized alumina-magnesia spinel seed crystals in a precursor of boehmite. The gel is then dried, granulated to the designated size, and sintered at 1200°C [81]. The resulting *seeded gel* (SG) abrasive grain consists of sub-micron size crystal structures, which will more likely experience micro-wear instead of breaking-off into large pieces or leading to total dislodgement of the complete grain from the bonding system of the grinding wheel. This technology creates a grinding wheel that is self-sharpening, or otherwise known as friable, since the micro-fractures of the grit constantly expose new sharp cutting edges. The main differences between the grains are that the SG is slightly harder (21 GPa) than Cubitron (19 GPa) [81] and some suggest that SG wheels last longer during grinding operations but Cubitron is more free-cutting [81].

Due to cost restrictions, seeded-gel (SG) grains are often combined with aluminum oxide grits resulting in a modified conventional grinding wheel with increased fracture toughness while maintaining the hardness characteristics. The majority of combinations are commonly available in 10, 30, and 50% and are classified by Norton as 1SG, 3SG, and 5SG respectively. The wheel used in this study was a 5SG wheel indicating 50% seeded gel content with the remainder being made up of conventional aluminum oxide.

Seeded gel (SG) grinding wheels are still considered conventional grinding wheels. They traditionally perform better than conventional aluminum oxide wheels and can still be trued and dressed with single point dressers compared to superabrasive wheels such as CBN and diamond, which require more expensive rotary dressers. When grinding workpieces, SG grinding wheels reduce power consumption, increase removal rates, provide higher grinding ratios, and reduce the chances of thermal burn [17], [80].

Figure 3.3 shows scanning electron microscope (SEM) images comparing loose seeded-gel and conventional aluminum oxide abrasive grains. The geometric properties of both grains are similar and are assumed to be the same in the modeling section of this thesis (see Chapter 5) since wheel workpiece interaction is not modeled. The main difference is that the SG grains appear to be smoother. This characteristic is most likely due to the manufacturing process since defects from crushing are avoided in the creation of SG grains.

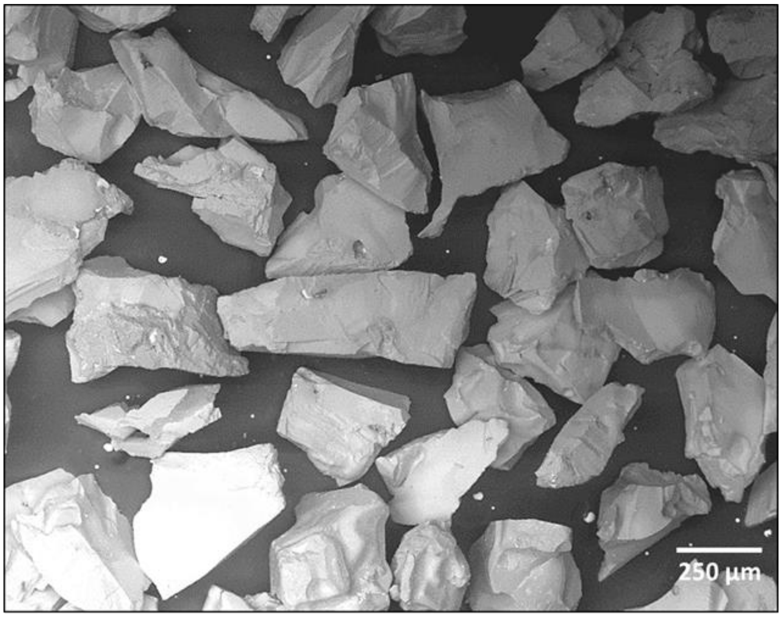

(a) Aluminum Oxide Grains

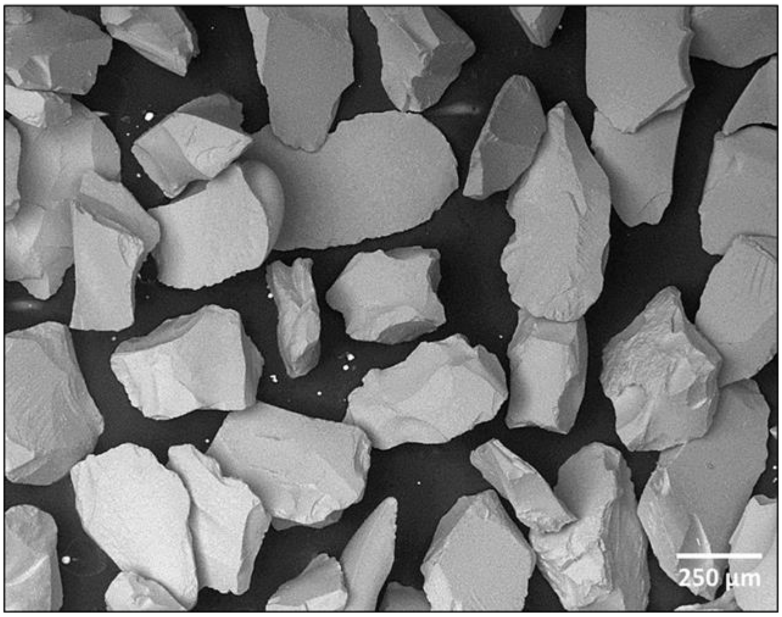

(b) Seeded Gel (SG) Grains

Figure 3.3 – SEM comparison of aluminum oxide and SG abrasive grains

3.1.2 Grain Density

To calculate the grain density, it is necessary to first calculate the grains per unit length within the wheel, which is given by [56]

$$N_l = \frac{{V_g}^{1/3}}{d} \tag{3.1}$$

where d is the mean grit diameter and V_g is the volume fraction of grit in the wheel and is calculated using [57]

$$V_g = 2(32 - S)\% \tag{3.2}$$

where S is the structure number of the wheel. The abrasive grain size of a grinding wheel is determined by the number of openings per unit length in a sieve. The mean grain diameter can be determined as [61]

$$d = 28.9g^{-1.1} \tag{3.3}$$

with g as the nominal grain size. Hou *et al.*'s [61] work also provides tables of the maximum and minimum grain diameters based on sieve size. The average number of grains per unit area is then calculated by squaring the grains per unit length [56]

$$N_s = N_l^2 \tag{3.4}$$

3.1.3 Surface Texture Height Distribution

The SG grinding wheel surface was scanned using the Alicona instrument. Due to the stochastic nature of the grinding wheel surface, thirty-four scans of the surface were made. It should be noted that some wheel topography studies assume that the heights of abrasives on the grinding wheel surface follow a normal distribution [31], [71], [82],

[83]. One aspect of the current work is to evaluate the validity of this assumption for the SG wheel. Figure 3.4 illustrates a typical height distribution of the vitrified bond SG grinding wheel used in this work. Rockwell Arena Input Analyzer software was used to fit the statistical distributions to the surface height measurements. Contrary to the commonly assumed Gaussian distribution, the data fit to the histogram of heights follows a negatively skewed beta distribution. The negative skewness of the grit height distribution indicates that there are more valleys than peaks. The general probability density function of the beta distribution is given by

$$f(x) = \frac{x^{\beta-1}(1-x)^{\alpha-1}}{B(\beta,\alpha)} \tag{3.5}$$

for $0 < x < 1$ where β and α are the shape parameters and are positive real numbers and *B* is the complete beta function given by

$$B(\beta,\alpha) = \int_0^1 t^{\beta-1}(1-t)^{\alpha-1}dt \tag{3.6}$$

The range of the distribution is generally from 0 to 1, but the sample X can be transformed to the scaled beta sample *Y* with a range from *a* to *b* by using the equation

$$Y = a + (b-a)X \tag{3.7}$$

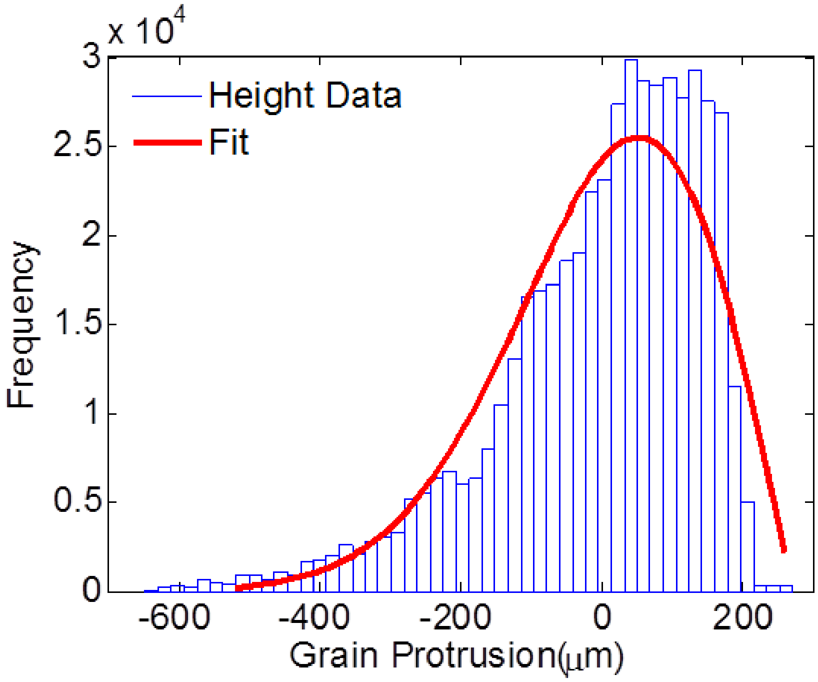

Figure 3.4 – Representative height distribution of SG wheel

3.1.4 Grain Spatial Distribution

Due to the random nature of grain placement during manufacturing of a multi-layered grinding wheel, it is important to accurately understand the actual distribution of grain spacing. A small portion of the SG grinding wheel was evaluated using micro-tomography (µCT) and the sequence of analysis employed is illustrated in Figure 3.5. A GE Preclinical eXplore Locus micro-CT machine was used to *slice* the wheel in 20 µm increments to produce the results shown in Figure 3.5a.

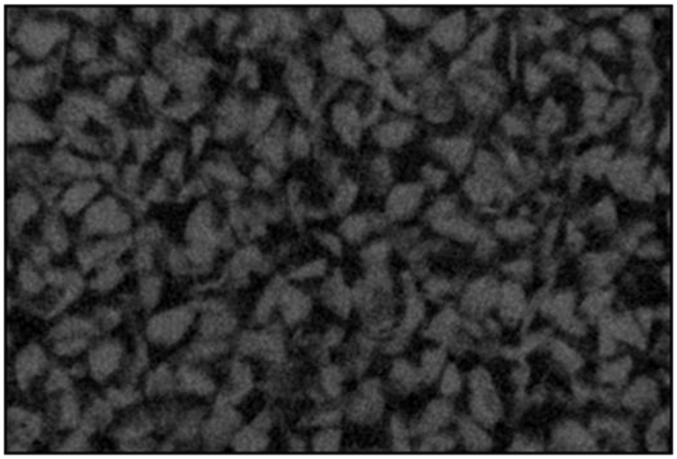

(a) µCT Scan Image

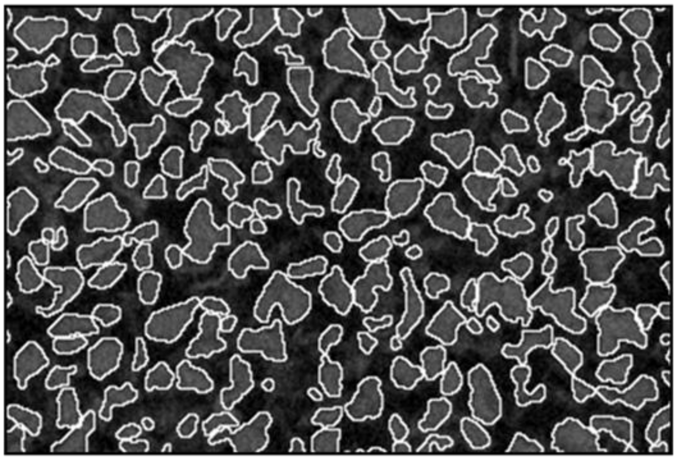

(b) Grain Segmentation

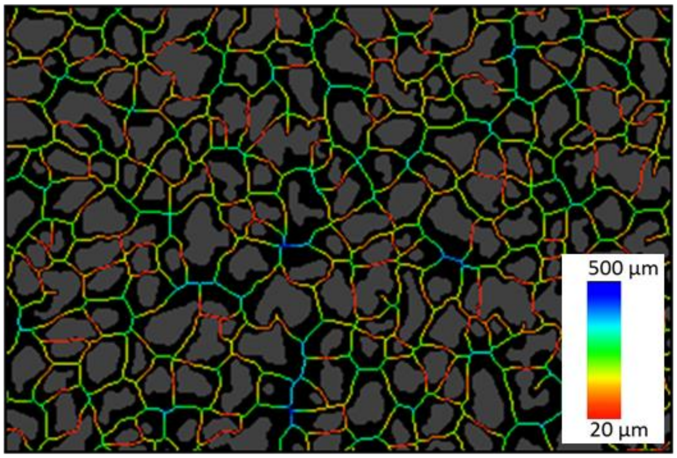

(c) Grain Spacing

Figure 3.5 – µCT scan results

Segmentation of each volume’s axial slices was performed using an automated segmentation algorithm to distinguish the difference between the grains, resulting in the images shown in Figure 3.5b. Spacing between the abrasive grains was then calculated and a resulting pseudo-colored overlay map per slice qualitatively displays the grain spacing in Figure 3.5c. The resulting distribution of grain spacing was found to follow the beta distribution (with shape parameters of α=1.53 and β=7.63) with positive skewness indicating that the grains tend to be closer together and, at times, almost touch each other as is evident from Figure 3.6.

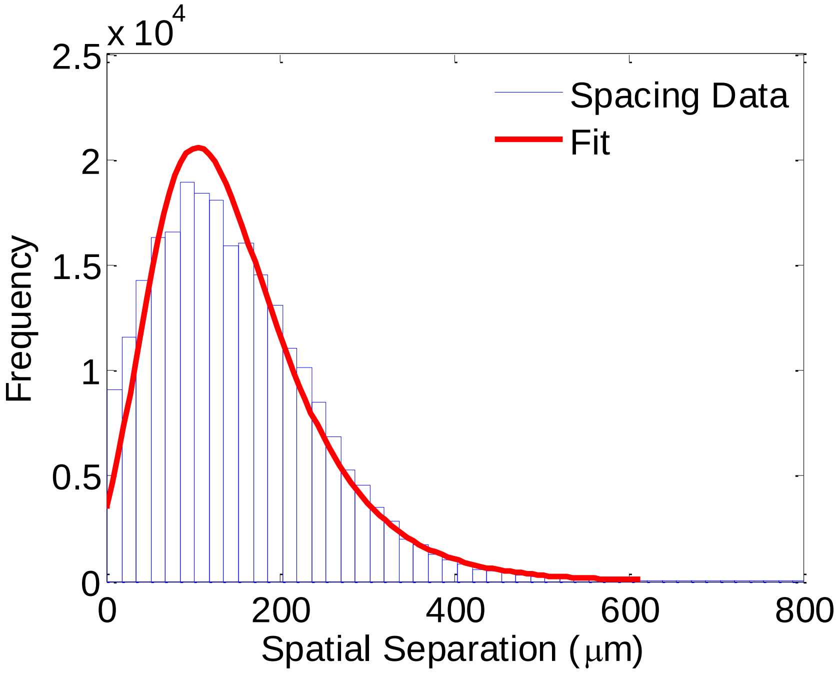

Figure 3.6 – Representative grain spacing distribution of SG wheel

3.2 CHARACTERIZATION OF INDIVIDUAL ABRASIVE GRAINS

Characterization of individual grains is often overlooked since most modeling and characterization studies of the grinding wheel make simplistic assumptions such as representing the grain as a sphere [8]. The main individual abrasive grain attributes considered in this study include grain shape, size, number of sides, and aspect ratio (Figure 3.7).

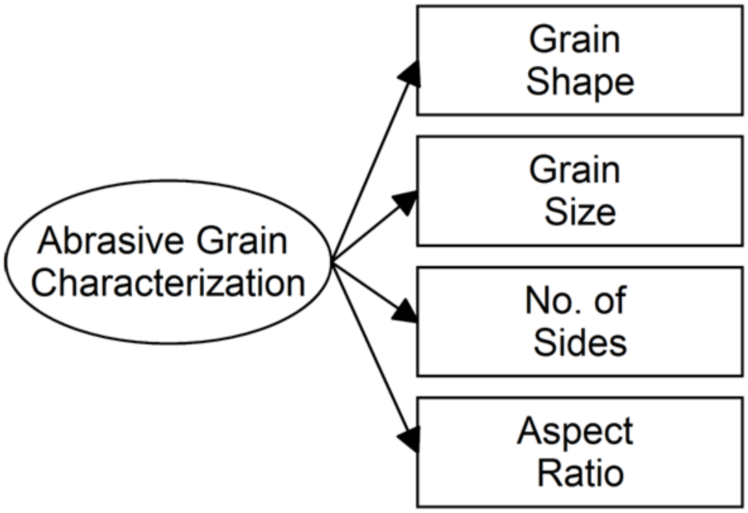

Figure 3.7 – Abrasive grain characterization attributes

3.2.1 Grain Shape

The shape of the grain has an enormous impact on the grain strength, grinding performance, and packing characteristics that impact wheel formation and manufacture [81]. Grain shapes consist of complex geometries and are often oversimplified as conical, elliptical, or spherical in wheel topography modeling studies, e.g. [64]. Figure 3.8a shows an SEM image of individual 60 grit SG grains and Figure 3.8b shows images of individual SG grains obtained from the µCT scans similar to other recent work on CBN grinding wheel characterization [84]. It is clear from these images that the actual shape of the grains is considerably more complex than commonly assumed. Based on these results, a polyhedral model for the grain shape is clearly more appropriate. Other researchers have also drawn similar conclusions based on three-dimensional analysis of grit shapes, albeit for super-abrasive wheels [12], [66], [84]–[86].

(a) SEM Image of Grains

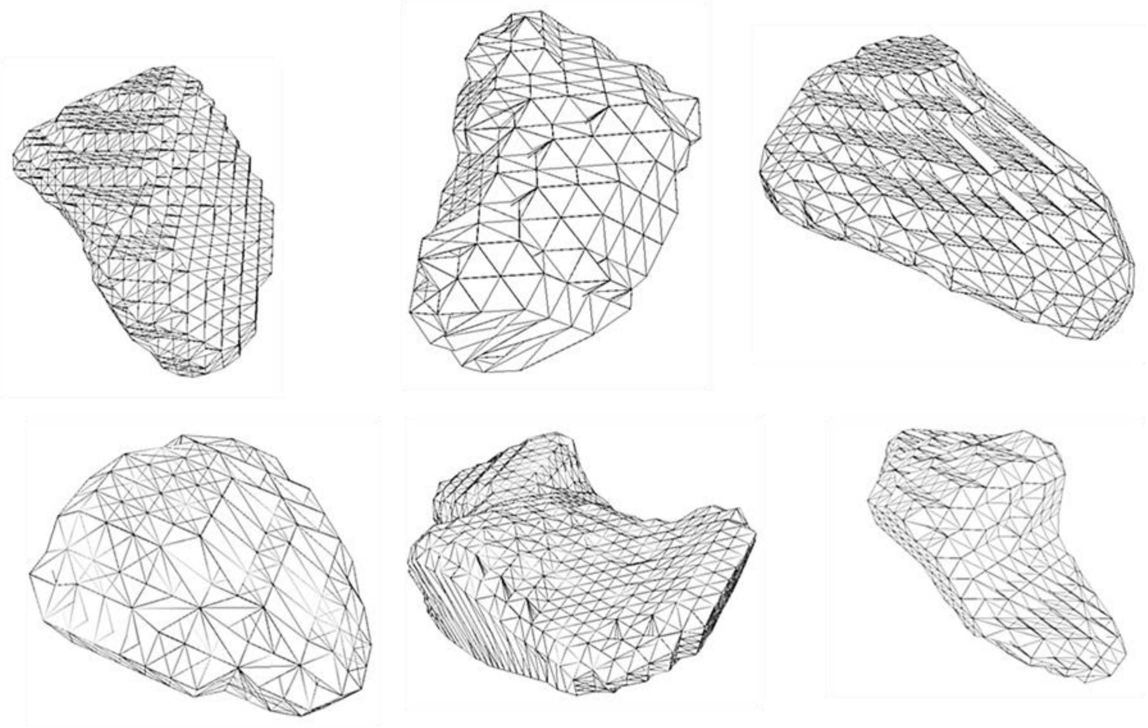

(b) µCT Scan of Grains

Figure 3.8 – Individual abrasive grains

3.2.2 Grain Size

The micro-tomography measurements provided additional characterization information that enabled the validation of the grain density formula and assumptions such as Gaussian distribution of grain diameters commonly made in wheel topography modeling studies [11], [61], [82]. Figure 3.9 shows the SG wheel grain diameter distribution obtained from the micro-CT scans. It clearly follows a normal distribution with a mean value of 242 µm. Table 2.1 compares the experimental findings with the corresponding theoretical values obtained from Equations 3.1 to 3.4. It is clear that the theoretical calculations compare quite well with the measured SG grain characteristics.

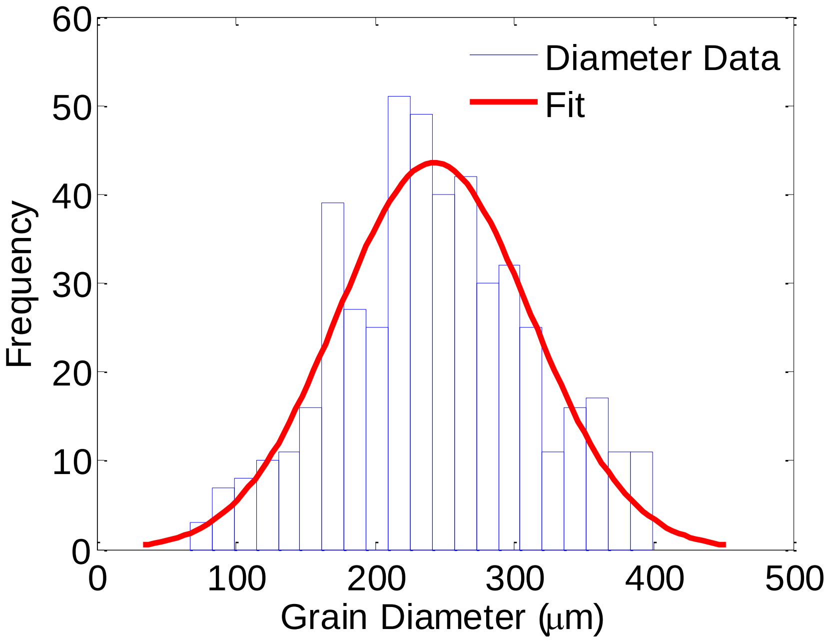

Figure 3.9 – Representative grain diameter distribution of SG wheel

Table 3.2 – SG grain characteristics comparing theoretical versus experimental attributes

Parameter	Theoretical	Experimental
Volume Fraction, V_g (%)	40	46
Grain Size, d (µm)	231 ± 22	242 ± 63
Grain Density, N_s (mm^{-1})	10	6

3.2.3 Number of Facets

The µCT scans could not be used to calculate the number of sides of an abrasive grain due to the limited resolution (20µm) of the machine used. Consequently, SEM images were used to manually count the approximate number of sides (facets) of SG grains. The number of sides obtained from the SEM images ranged from four to ten with a mean value of seven. The resulting distribution is shown in Figure 3.10 and is seen to follow a gamma distribution with a shape parameter k of 0.663 and a scale parameter θ of 4.58, which has the following general form

$$f(x) = \frac{\beta^{-\alpha} x^{\alpha-1} e^{-x/\beta}}{\Gamma(\alpha)} \tag{3.8}$$

for $x > 0$ and where α and β are the shape parameters and Γ is the complete gamma function given by

$$\Gamma(\alpha) = \int_0^\infty t^{\alpha-1} e^{-t} dt \tag{3.9}$$

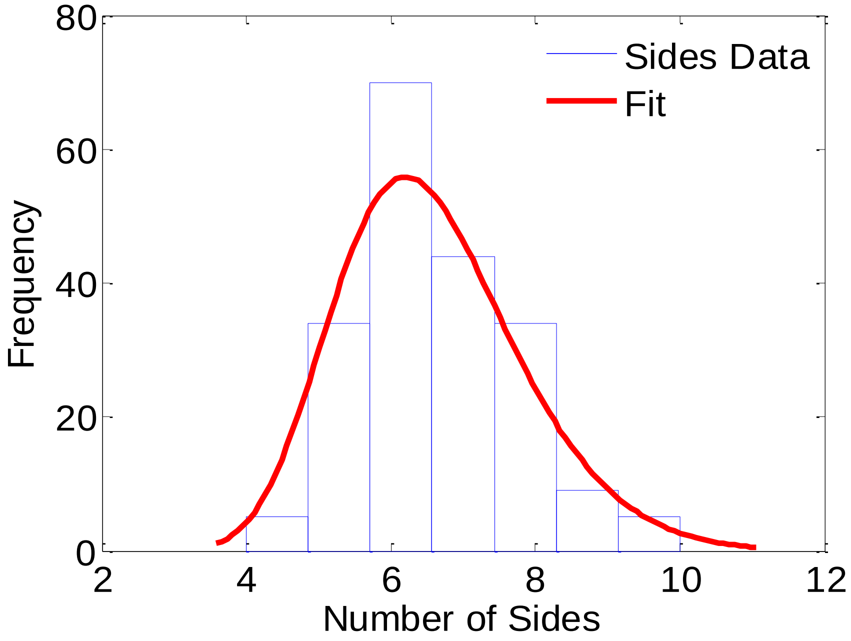

Figure 3.10 – Distribution of number of sides

3.2.4 Aspect Ratio

The abrasive grains in a SG grinding wheel are randomly formed and shaped in manufacturing and come in multiple aspect ratios. Past studies of three-dimensional grinding wheel characterization [12], [81], [84], [87] have focused mostly on super-abrasive wheels. In contrast, there is limited information on the grain aspect ratios of SG wheels. Figure 3.11 shows SEM images of individual 60 grit SG grains, which reveal both high and low aspect ratios. A blocky (low aspect ratio) grain will generally be far stronger than an angular, sharp-cornered grain [88]. Measurement features in the SEM software were used to determine the aspect ratios for a number of SG wheel grains resulting in the histogram shown in Figure 3.12. The measured aspect ratios range from 1:1 to 1:7 and are found to follow the Weibull distribution with a shape parameter *k* of

1.11 and a scale parameter λ of 1.08. The Weibull distribution has the following mathematical form for its probability density function

$$f(x) = \alpha\beta^{-\alpha}x^{\alpha-1}e^{-(x/\beta)^{\alpha}} \tag{3.10}$$

for x > 0 and where α is the shape parameter and β is the scale parameter. It should be noted that the grain diameter referred to in the grain size characterization presented earlier (section 3.2.2) is the smaller of the two grain dimensions since the longer dimension can penetrate through the sieve.

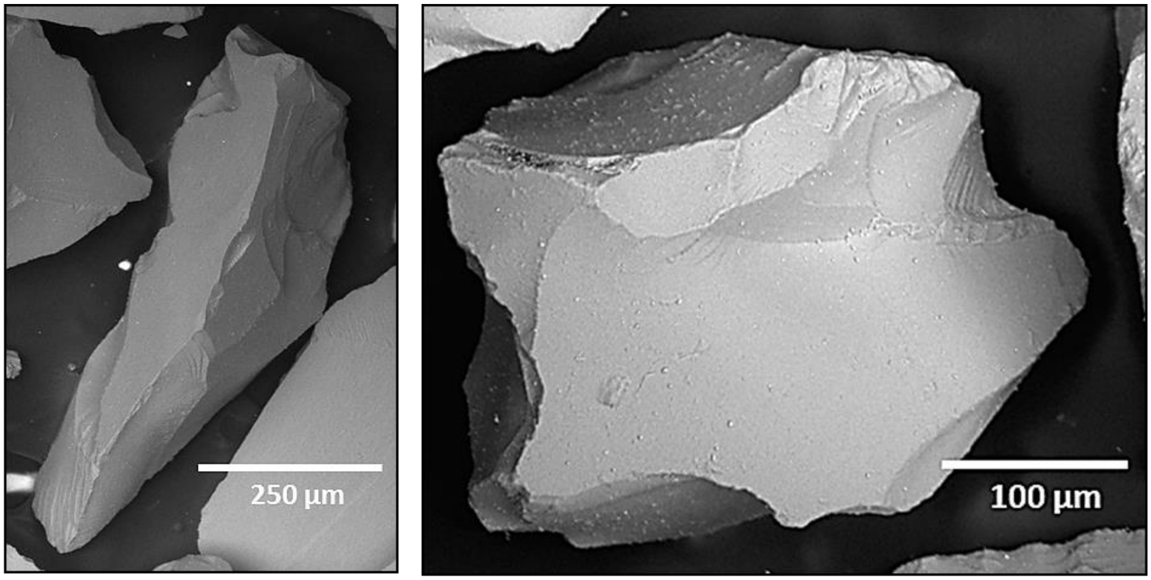

(a) High Aspect Ratio (b) Low Aspect Ratio

Figure 3.11 – Typical grain aspect ratios

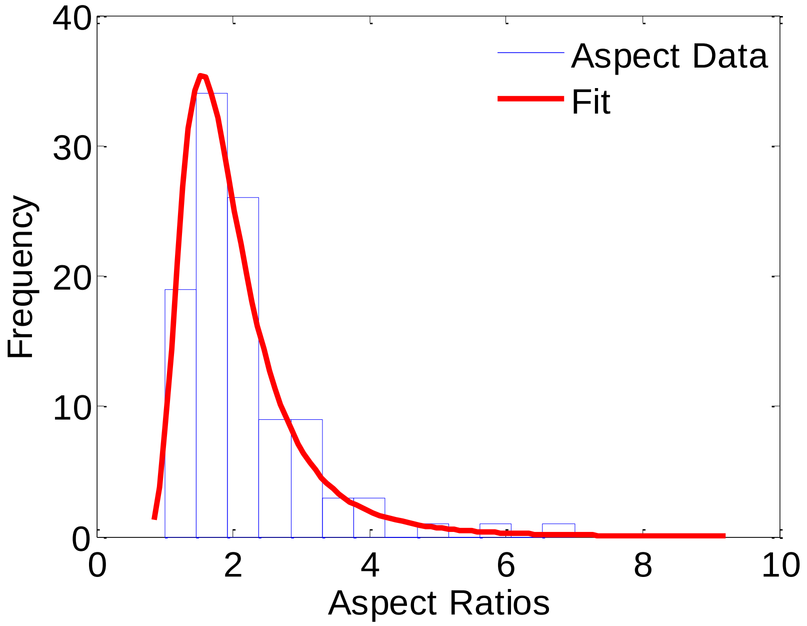

Figure 3.12 – Grain aspect ratio distribution

3.3 SUMMARY

The objective of this chapter was to present a detailed study of the micro topographical characteristics of a seeded gel (SG) grinding wheel and the abrasives making up the wheel surface. Three-dimensional micro-coordinate metrology equipment, scanning electron microscopy (SEM), and micro-tomography (µCT) were used to quantitatively establish the statistics of grain height, grain density, and spacing and individual grain characteristics such as grain shape, grain size, number of facets, and aspect ratio. The results showed that the SG wheel surface height distribution follows the beta distribution rather than the commonly assumed Gaussian distribution. The grain spacing was shown to also follow the beta distribution. Visual counting of the grain facets revealed that the number of sides of a grain follows the gamma distribution. The grain aspect ratio was shown to follow the Weibull distribution.

4. DRESSING EXPERIMENTS

Single point dressing of seeded gel grinding wheels was performed to understand how the grinding wheel surface topography changes as a function of dressing conditions and is summarized in this chapter. The findings of experimental trials along with proper characterization of the grinding wheel are important factors in creating the stochastic model in Chapter 5. The key inputs to the model found from experimentation mainly concentrate on the distribution of the grain protrusion above the surface of the grinding wheel surface. Additionally, changes in the bearing area and volume parameters are studied as a function of the dressing conditions.

4.1 EXPERIMENTAL TRIALS

Single point diamond dressing experiments were performed on a Toyoda GL3P-25SII cylindrical grinder (Table 4.1) and measured using three-dimensional optical surface measurement instrumentation (Alicona IFM G4). A standard Norton BCSG10M7 1 carat SG Dodec diamond was used for single point dressing (Figure 4.1).

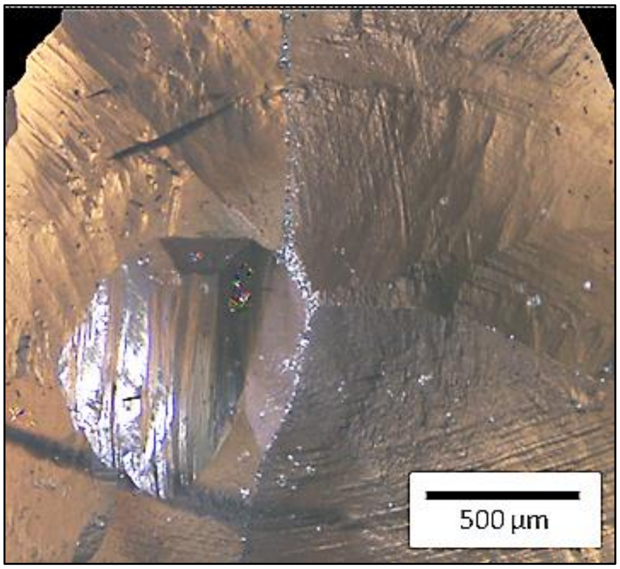

Figure 4.1 – Fresh diamond dresser

A custom wheel indexing apparatus, shown in Figure 4.2, was designed and built to facilitate precision relocation of the grinding wheel surface to enable optical comparison of the pre- and post- dressing wheel surface topography while varying the dressing infeed and lead conditions in the experiments.

Figure 4.2 – Experimental setup used to measure grinding wheel surface topography. (1) optical surface measuring instrument, (2) wheel indexer, (3) grinding wheel

4.2 EXPERIMENTAL SETUP

The grinding wheel dressing trials were performed on a seeded gel grinding wheel using a stationary single point diamond dresser mounted on a cylindrical grinding machine. The surface of the grinding wheel was measured with focus variation surface topography measurement equipment (Alicona IFM G4) before and after the dressing process to compare and contrast the changes in the three-dimensional surface texture of the grinding wheel. The dressing equipment used in the experiments is summarized in Table 4.1 and covered in greater detail later in the chapter.

Table 4.1 – Dressing equipment

Parameters	**Specifications**
Grinding Machine	Toyoda GL3P-25SII
Dressing Type	Single Point Diamond
Coolant	5% Conc. TRIM SC520
Dresser	1 Carat SG Dodec Diamond
Lead Angle	10°
Drag Angle	0°
Wheel Type	5SG46-JVS
Wheel Diameter	305 mm (12 in.)

4.2.1 Single Point Diamond Dresser

There are different ways of dressing a grinding wheel including the main categories of stationary and rotary dressing. The type of dresser used in this study was a stationary single point dresser. The dressing parameters varied in the experiments are the infeed and lead of the dressing diamond as illustrated in Figure 4.3 and were chosen since these parameters along with the shape of the diamond dresser govern the dressing process [7]. The infeed is the depth of cut, or the amount the diamond protrudes into the grinding wheel, while the lead is the rate at which the diamond traverses across the grinding wheel periphery. The diamond tip is typically inclined at an angle of 3° to 15° (10° in this study) to the grinding wheel surface normal, and is known as the lead angle β, and at a drag angle φ of 0° to 30° (0° for the current experiments) to the face of the rotating grinding wheel. These ranges of lead and drag angles of the diamond dresser ensure that optimal dressing occurs without excessive heating or wearing of the dressing tool [89].

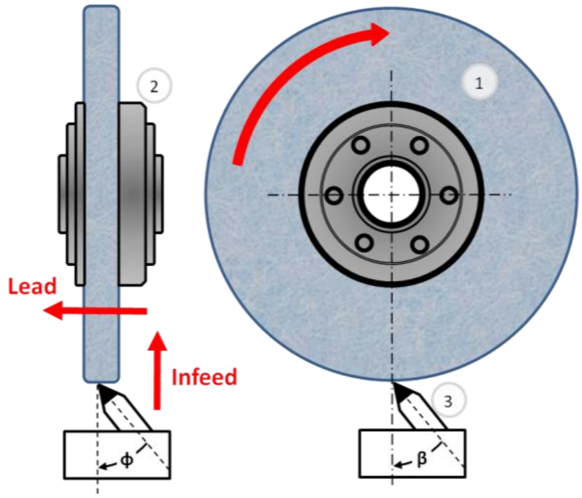

Figure 4.3 – Single point dressing angles. (1) grinding wheel, (2) grinding wheel hub, (3) single point dresser controlling angles of diamond (drag angle, φ=0° and lead angle, β=10°)

4.2.1.1 Dressing Infeed

The dressing infeed, sometimes referred to as the depth of cut, is the amount the dresser tip engages into the surface of the grinding wheel during the dressing process. In theory, the dressing forces will increase as a result of increased infeed which tends to crush the wheel surface and produce a sharper wheel topography [1].

4.2.1.2 Dressing Lead

The dressing lead in the stationary dressing process is the distance travelled by the tip of the single point dresser across the wheel periphery per wheel revolution. Dressing lead is mathematically represented by the equation [1]

$$s_d = \frac{\pi d_s U_d}{v_s} \tag{4.1}$$

where d_s is the grinding wheel diameter, U_d is the cross feed velocity of the dresser across the grinding wheel surface, and v_s is the grinding wheel peripheral speed.

4.2.1.3 Dressing Overlap Ratio

The overlap ratio relates the width of the contact area of the diamond dresser to the dressing lead as the diamond traverses across the surface of the grinding wheel. The overlap ratio is mathematically expressed as

$$U = \frac{b_d}{s_d} \tag{4.2}$$

with b_d as the width of the diamond dresser contact area with the grinding wheel as illustrated in Figure 4.4 . The contact width in the current experiments was monitored and used in this calculation.

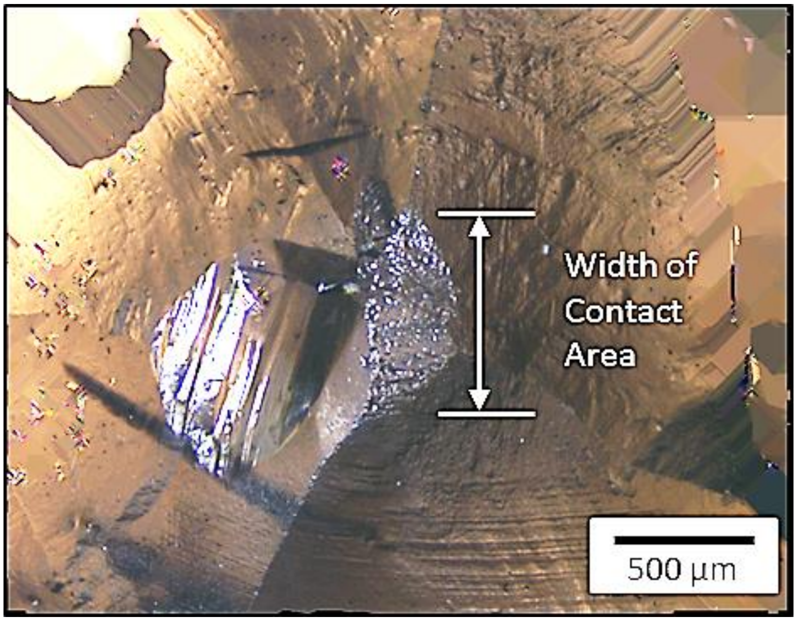

Figure 4.4 – Diamond dresser contact width dimension

4.2.2 Cylindrical Grinder

There are several types of grinding machines used in the industry including surface, cylindrical, and creep-feed grinding machines. The grinding machine used in this study was a Toyoda GL3P-25SII cylindrical grinder. The main parts of the grinder include the

i) base, ii) work table, iii) dresser, iv) grinding wheel/spindle, v) coolant supply, and vi) controller as illustrated in Figure 4.5. It is important that the grinding machine base be very rigid and stable to withstand the loads of the grinding process and maintain trueness of the workpiece. The work table function is to hold the workpiece while the diamond dresser (mounted to rear of table) traverse across grinding wheel face. The grinding wheel is attached to the spindle and applies the infeed (depth of cut) into the workpiece or diamond dresser. All movements of the grinding machine axis are computer numerically controlled (CNC) by the computer (controller) of the system.

Figure 4.5 – Precision grinding machine. (1) machine base, (2) workpiece slide table with work head, (3) dresser mounted on back of slide table, (4) grinding wheel, (5) coolant nozzle, (6) controller of grinding machine

4.2.3 Surface Texture Measurement Equipment

Focus variation based surface metrology techniques are a relatively new measurement method that enable the measurement of areal surface topography using optics with limited depths of field and vertical scanning [90]. It offers multiple advantages [91] including:

- Measurement of surfaces with steep flanks up to 80°
- Measurement of surfaces with strongly varying reflection properties
- Measurement of surfaces with fine (from 10nm) or high roughness

The grinding wheel surface texture created by the dressing process was measured using an Alicona IFM G4 optical micro coordinate and surface finish measurement equipment utilizing focus variation with the scanning parameters summarized in Table 4.2. The use of the machine's largest 5x magnification optic enables a field of view of 2.175 x 2.858 mm area of the grinding wheel surface. The manufacturer advertises that the 5x optics provides a sampling distance of 1.75 µm, best vertical resolution of 410 nm, and a minimum measurable three-dimensional roughness of (*Sa*) of 600 nm.

Table 4.2 – Measurement equipment characteristics

Parameters	**Specifications**
Instrument Type	Alicona IFM G4
Scanning Area	2.175x2.858 mm
Scan Size	1232x1626 points
Sampling Distance	1.75 µm
Magnification	5x

The Alicona measurement unit is illustrated in Figure 4.6. The main components of the system include the head unit, optic turret, x-y stage, risers, and the built in isolation table. The risers supply the necessary clearance to fit the 305 mm (12 in.) grinding wheel. The x-y stage and built-in isolation table were not used in the current experiments since the custom wheel indexing apparatus was utilized. Note that the Alicona equipment and indexing unit were both mounted on an additional isolation table to ensure negligible impact of floor vibrations during the measurement process.

Figure 4.6 – Three-dimensional micro-coordinate measurement equipment (Alicona IFM G4) to map grinding wheel surface topography. (1) head unit, (2) optics turret, (3) x-y stage, (4) risers, (5) isolation table, and (6) emergency stop button

The head unit is one of the most important components of the measurement equipment and is illustrated in detail in Figure 4.7. The left image is a zoomed-in view of the head unit while the right image illustrates the internal functions of the focus variation type of measurement equipment. The basic components of focus variation equipment include the optical system, illumination source, CCD sensor to detect focus, and a driving unit for the focus search. White light is generated from the LED light source and transmitted through the semi-transparent mirror and objective lens to the grinding wheel surface. The light is then reflected in multiple directions and collected by the objective and projected through the semi-transparent mirror and tube lens to the charge-coupled device (CCD) sensor.

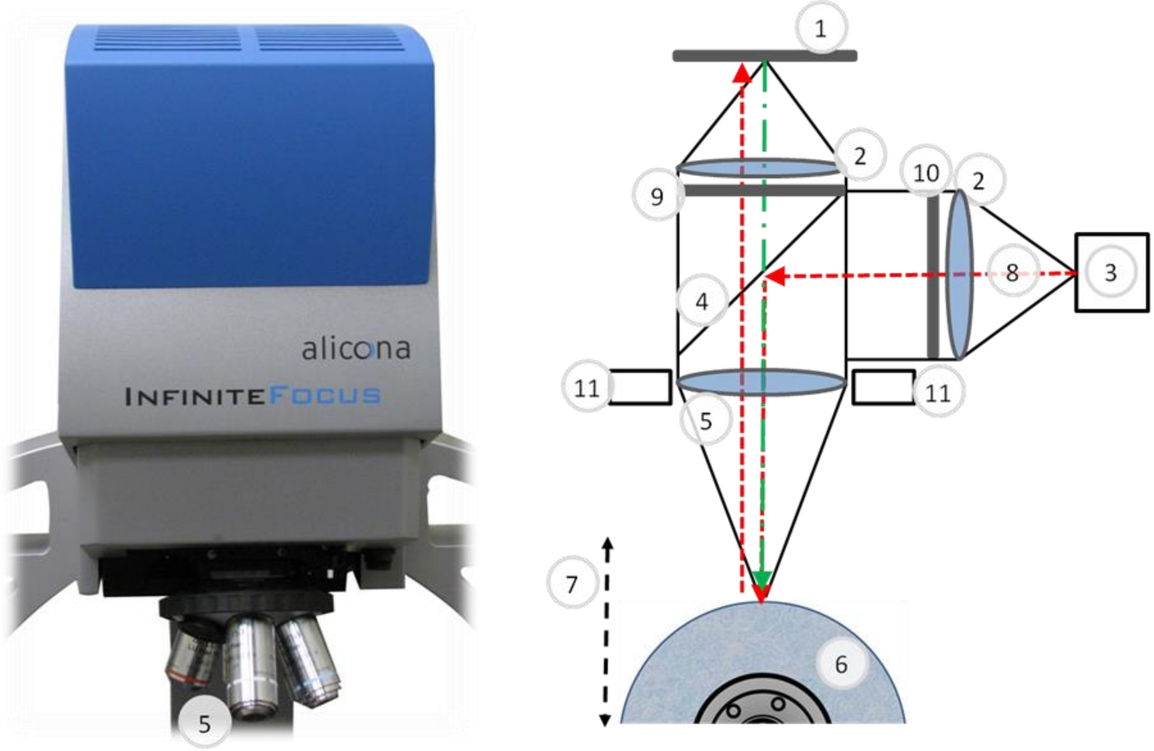

(a) Alicona Head **(b) Function of Focus Variation**

Figure 4.7 – Schematic diagram of focus variation measurement equipment. (1) CCD sensor, (2) lenses, (3) white light source, (4) semi-transparent mirror, (5) objective lens with limited depth of field, (6) grinding wheel sample, (7) vertical movement with driving unit, (8) light rays from the white light source, (9) optical analyzer, (10) optional polarizer, and (11) optional ring light

A typical live view of the SG wheel surface and the resulting scanned image of the surface are shown in Figure 4.8. Individual SG grains observed in Figure 4.8a are the white features while the aluminum oxide grains appear transparent. Figure 4.8b is a top view of the resulting scan of the same area.

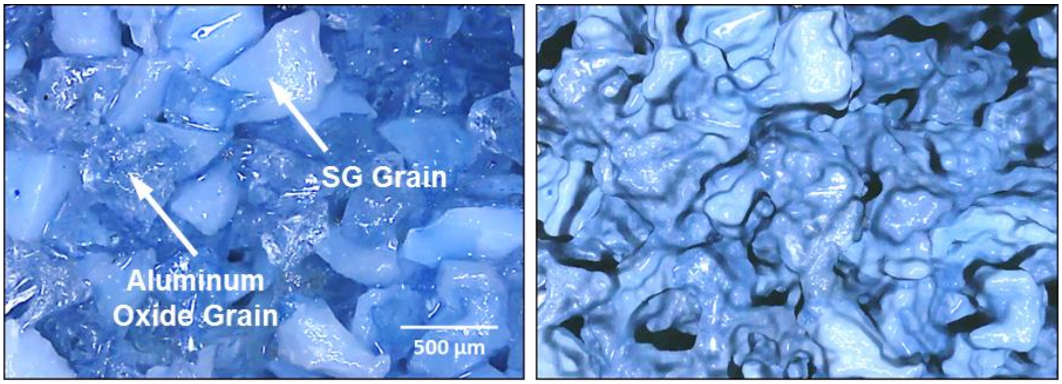

(a) Live view of grinding wheel surface (b) 2D View of scan

Figure 4.8 – Live and scanned images of SG grinding wheel surfaces

4.3 DESIGN OF EXPERIMENTS

A full factorial design of experiment (DOE) was used while varying the dressing lead and infeed at the three different levels listed in Table 4.3. The DOE chosen produces a full factorial design across the factor variables, infeed (µm) and lead (mm/rev), and the basic experimental plan is listed in Table 4.4. The levels of infeed included 13, 25, and 50 µm while the lead levels comprised of 0.15, 0.15, and 0.25 mm/rev. The experimental runs are randomized and were repeated three times. The measured wheel texture parameters were then averaged and used in further analyses. The spindle speed of 1672 RPM, resulting in a surface speed of approximately 27 m/s, was held constant throughout the experiments and was chosen to suit future workpiece grinding studies.

Table 4.3 – Experimental design

Parameter	Specification
Design Type	General Full Factorial
Replications	3
Factors	Infeed, Lead
Levels, Infeed	13, 25, 50 µm
Levels, Lead	0.05, 0.15, 0.25 mm/rev
Overlap Ratio	16,5,3
Spindle Speed	1672 RPM

Table 4.4 – Experimental plan

Run	Infeed (r, µm)	Lead (mm/rev)
1	13	0.05
2	13	0.15
3	13	0.25
4	25	0.05
5	25	0.15
6	25	0.25
7	50	0.05
8	50	0.15
9	50	0.25

4.4 EXPERIMENTAL PROCEDURE

Figure 4.9 summarizes the experimental procedure followed. It was first necessary to prepare the grinding wheel surface prior to the dressing tests. Wheel preparation consisted of initial static balancing, wheel truing, and then performing another static balance after circularity of the wheel had been restored. Before the dressing experiments, the wheel surface was *initialized* by making several passes of the single point diamond dresser at a low lead (0.0229 mm/rev) and a gradually reducing infeed (ranging from 25.4 to 6.35 µm) [29]. The purpose of initializing the wheel is to start each dressing condition with a similar surface for proper comparison and is taken to represent an undressed wheel.

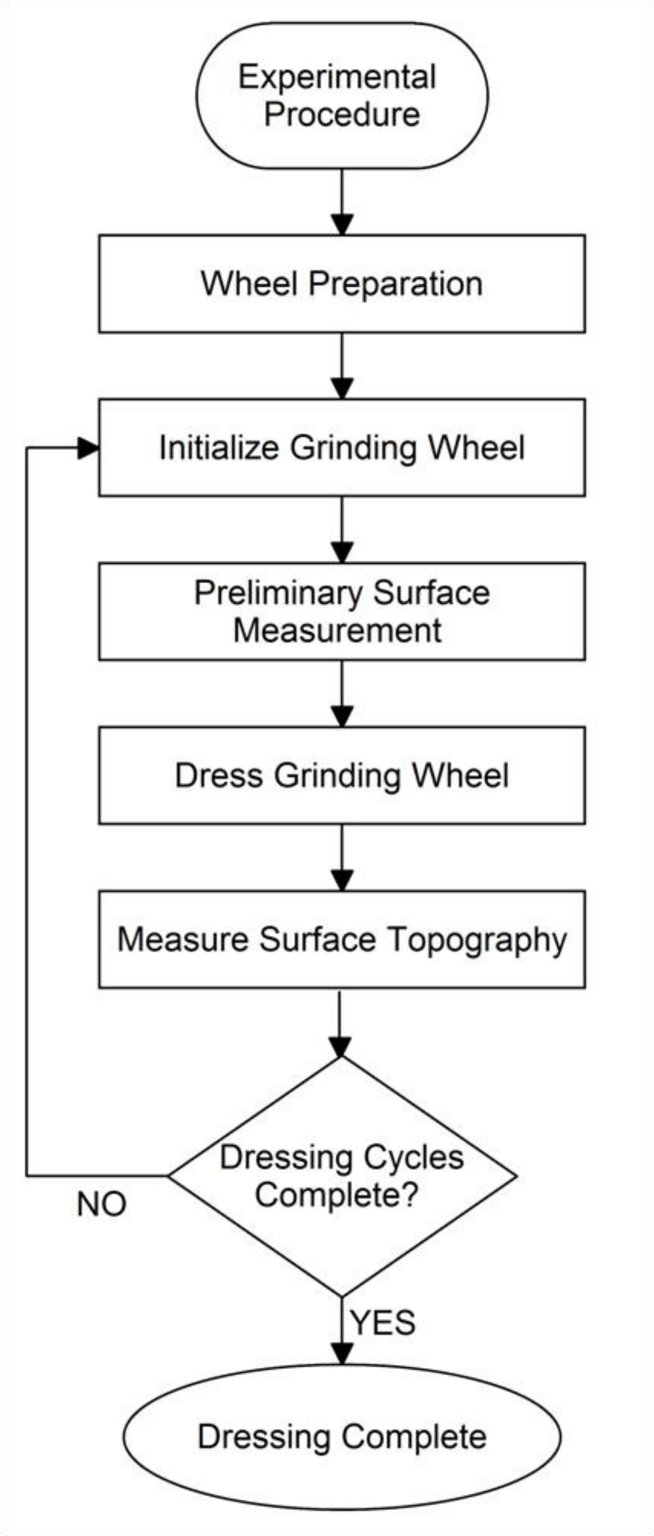

Figure 4.9 – Experimental procedure

The wheel topography was scanned using the Alicona instrument before and after each dressing experiment. The wheel topography and the associated texture parameters were measured at 30 random locations around the wheel circumference and the four quadrants of the wheel, yielding a total of 34 measurements per dressing condition. All 34 measurements were averaged to obtain texture parameter values for the particular experimental run. This process was randomly repeated for the nine different dressing conditions and replicated 3 times for a total of 27 distinct experimental runs.

4.5 RESULTS

It is expected that SG grinding wheels will wear less and keep the abrasives sharp compared to conventional corundum grinding wheels. This stems from the fact that the SG abrasive grain consists of sub-micron size crystalline particles that can easily separate from the abrasive grit by attritious wear during grinding [80] and thereby increase the friability of the grit.

4.5.1 Dressing Tool Wear

The wear land of the single point dresser started at a width of 660 µm (generated in preliminary testing) and wore approximately 230 µm over the 27 experimental trials as shown in Figure 4.10 (additional images for the experiments, divided by repetition of DOE, are given in Appendix A). The width of the dressing tool is an important factor since it affects the overlap ratio as previously mentioned.

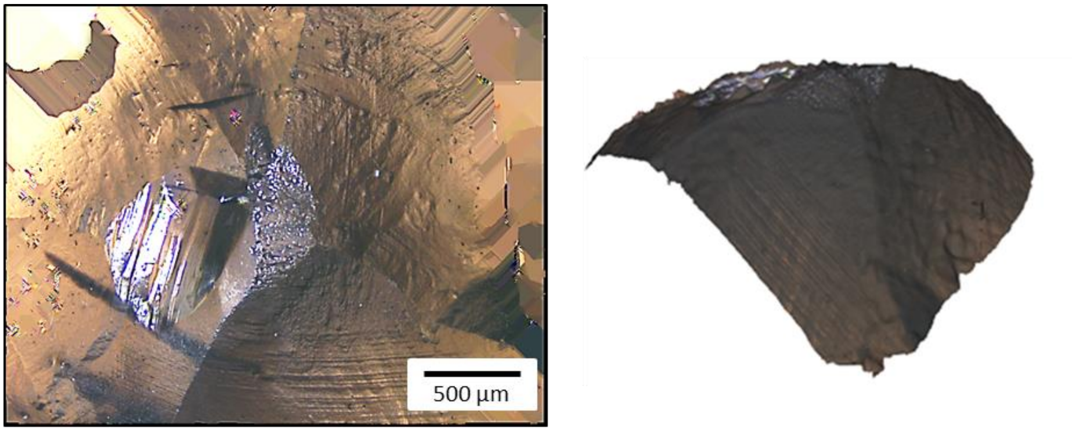

(a) Initial diamond dresser geometry

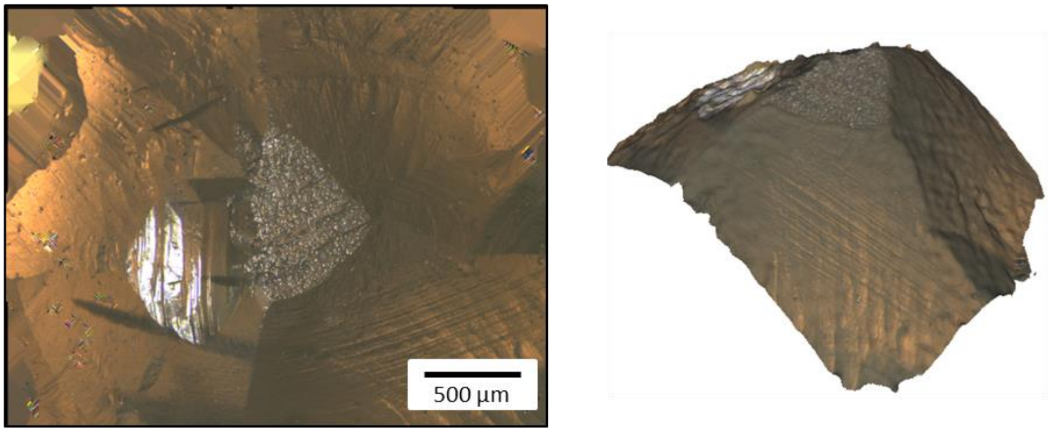

(b) Final diamond dresser geometry

Figure 4.10 – Diamond dresser wear

4.5.2 Change in Surface Topography

4.5.2.1 Grinding Wheel Wear Mechanisms

The resulting wheel surface topography created during the dressing process is due to the interaction of the dressing diamond and the abrasives/grits and bonding material that make up the wheel. Researchers have recognized the existence of three distinct wear mechanisms in dressing: grain fracture, bond fracture, and attritious wear [92]–[94]. Grain fracture includes both micro-and macro-fracturing while bond fracture refers to total grain dislodgement, which can decrease the planar grain density [8]. Micro-fracture occurs when small sections of the abrasive grain break off while macro-fracture occurs when a large portion of the grain separates during interaction with the dressing diamond. Attritious wear results in the flattening or dulling of the abrasive grains by rubbing against the workpiece surface (or diamond dresser in the present experimental study) [92].

4.5.2.2 Grain Cutting Theory

The function of dressing a grinding wheel is to modify the wheel surface topography so as to optimize the grinding wheel grain shape which interacts with the workpiece material during the grinding process. In early grinding research, the dressing process was modeled as the single-point dressing diamond cutting through the abrasive grains generating a thread profile on the surface of the grinding wheel [95]. This cutting theory assumes that the resulting grinding wheel surface pattern transfers to the workpiece surface during the grinding process. This "grain cutting theory” has been assumed by many researchers since the surface profile of the ground workpiece can often be directly attributed to the dressing process [95]–[97]. The theory suggests that the theoretical peak-to-valley height R_{pv} of the resulting thread profile on the wheel can be is mathematically represented as [7]

$$R_{pv} = \frac{S_d}{2\,tan\,(\frac{\theta}{2})} \tag{4.3}$$

where θ is the dressing diamond tool tip angle and S_d is the dressing lead as the diamond moves across the wheel surface per wheel revolution. Early researchers investigated the accuracy of the cutting theory using stylus measurements of the grinding wheel surface and found that the workpiece surface profiles showed clear dressing features on the ground surface, but could not detect any pattern on the surface of the wheel [89]. It was suggested that this was probably because any grooves produced in the wheel by the dressing process were very small compared to the roughness of the wheel [89].

4.5.2.3 Topography Formation

Later investigations were performed by examining the grain debris produced during the dressing process [98]. The investigations showed that the entire weight of the material dressed off the grinding wheel (vitrified bonded) consisted of particles larger than the dressing depth but smaller than the abrasive grains of the grinding wheel. This finding demonstrates that grain and bond fracture is occurring during the interaction of the diamond dressing tool with the grinding wheel surface and is producing large fragments closer to the size of the grains, which suggests grain dislodgement may be occurring during the dressing process. This theory assumed that bond fracture is responsible for determining how many active grains remain on the wheel surface, and the morphology of these grains is mainly controlled by grain fracture [98].

Another theory suggests that the dressing process consists of gross fracture and leveling effects explained by macro and micro actions [57], [89]. The macro action splits grains or breaks bonds giving the gross characteristics of the wheel surface topography, resulting from dressing parameters and the diamond tool shape. The micro fractures of the grain surface generate new cutting edges, which depends on the dressing parameters and the friability of the abrasive grains.

The precision relocation apparatus, illustrated in Figure 4.11, enables an interesting visual analysis of the microscopic changes in wheel topography due to dressing, which can be clearly seen by comparing the colored contour maps of the pre- and post-dressing surfaces in Figure 4.12. The images and contour maps show clear evidence of micro and macro fracture of the grains along with instances of total grain dislodgement. Figure 4.12 compares the pre- and post-dressing surface topography of a specific quadrant of the SG wheel surface used in the current study for a representative dressing condition of 50 μm infeed and 0.25 mm/rev lead. The corresponding overlap ratio is 3.

Figure 4.11 – Precision indexing apparatus to align grinding wheel for pre- and post- grinding measurements. (1) indexing head, (2) precision hub adapter/locator, (3) base pivot for loading/unloading wheel, and (4) grinding wheel

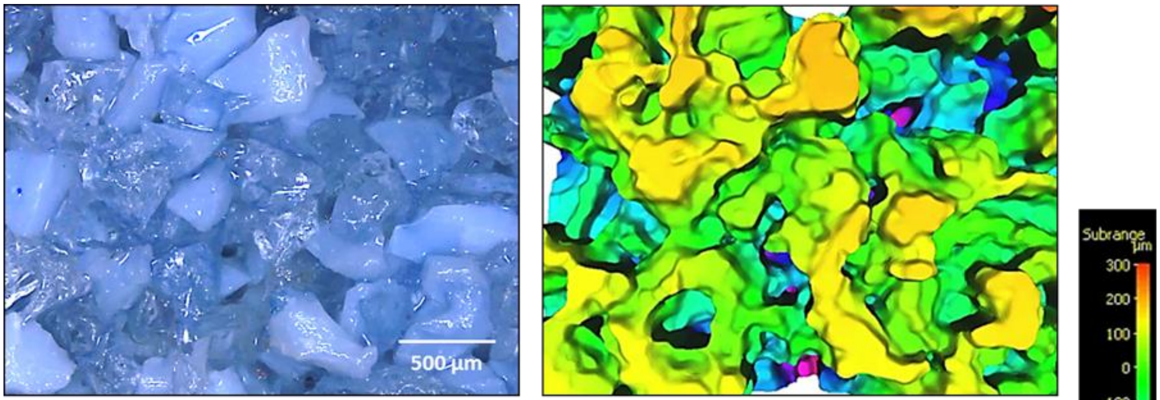

(a) Pre-dressing surface topography

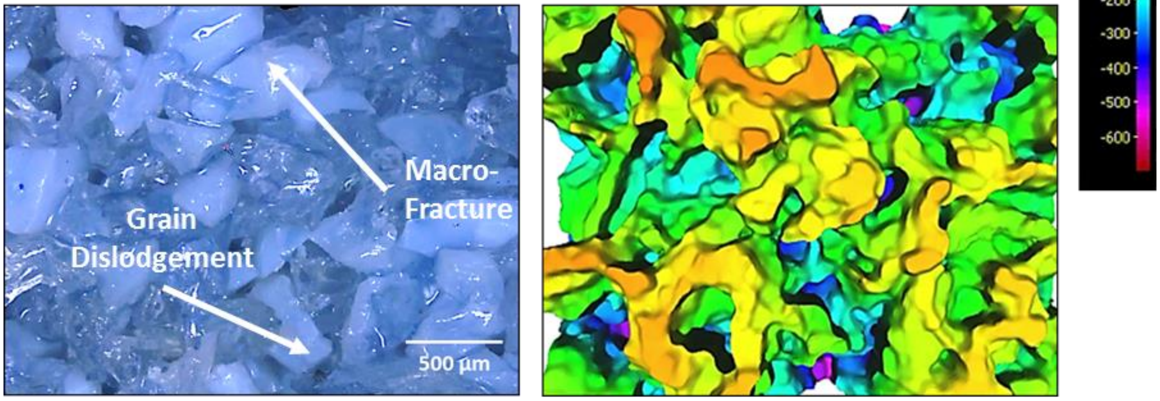

(b) Post-dressing dressing topography

Figure 4.12 – Representative pre- and post-dressing surface topography comparison. Dressing 50 µm infeed and 0.25 mm/rev lead; overlap ratio of 3

4.5.3 Measured Parameters

The grinding wheel surface texture created by the dressing process was measured using the Alicona optical micro coordinate and surface finish measurement equipment utilizing focus variation to study the effects of infeed and lead. The concerned measured parameters are listed and described in Table 4.5. These parameters are used to experimentally characterize the surface topography of the grinding wheel and how it changes with dressing infeed and lead.

Table 4.5 – Experimentally measured amplitude, volume, and area parameters

Amplitude	**Definition**
Peak height, *Sp*	Maximum peak height of selected area
Skewness, *Ssk*	Skewness of selected area
Kurtosis, *Sku*	Kurtosis of selected area
Volume and Area	**Definition**
Reduced peak height, *Spk*	Mean height of the peaks above the core material
Core roughness depth, *Sk*	Height of the core material
Peak material component, *Smr1*	Fraction of the surface consisting of peaks above the core material
Peak volume, *Vmp*	Peak material volume of the topographic surface
Core volume, *Vvc*	Core void volume of the surface
Core material, *Vmc*	Core material volume of the topographic surface

4.5.3.1 Amplitude Parameters

The effects of dressing parameters on the maximum peak height *Sp* of the scanned surface are shown in Figure 4.13. The chart was created by averaging the maximum peak heights obtained by sampling the beta distributions of surface heights for each dressing condition 10,000 times to produce a statistically valid representation of the wheel surface. Note that the error bars are very small. It can be seen that, in general, the peak height increases with increasing lead and infeed.

Figure 4.14 shows a side-by-side comparison of the pre- and post-dressing grain height distributions for the aggressive dressing condition of 50 µm infeed and 0.25 mm/rev lead and an overlap ratio of 3. Both pre- (shape factor of $\alpha = 5.20$ and $\beta=2.20$) and post-dressing (shape factor of $\alpha = 4.56$ and $\beta=2.08$) grit height distributions exhibit a best-fit to the beta distribution.

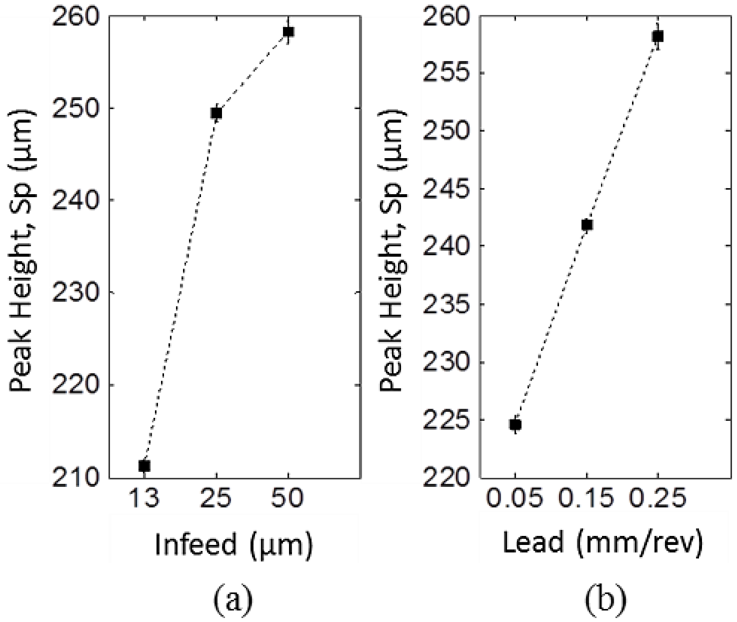

Figure 4.13 – Effects of dressing on peak height, *sp*. (a) effect of infeed, (b) effect of lead

The aggressive dressing condition changes the shape of the height distribution causing its skewness to become somewhat less negative and its kurtosis (peakedness) to decrease slightly. The change in height distribution is possibly due to grit loss arising from fracture and/or dislodgment of the entire abrasive grain when bond fracture occurs during the dressing process.

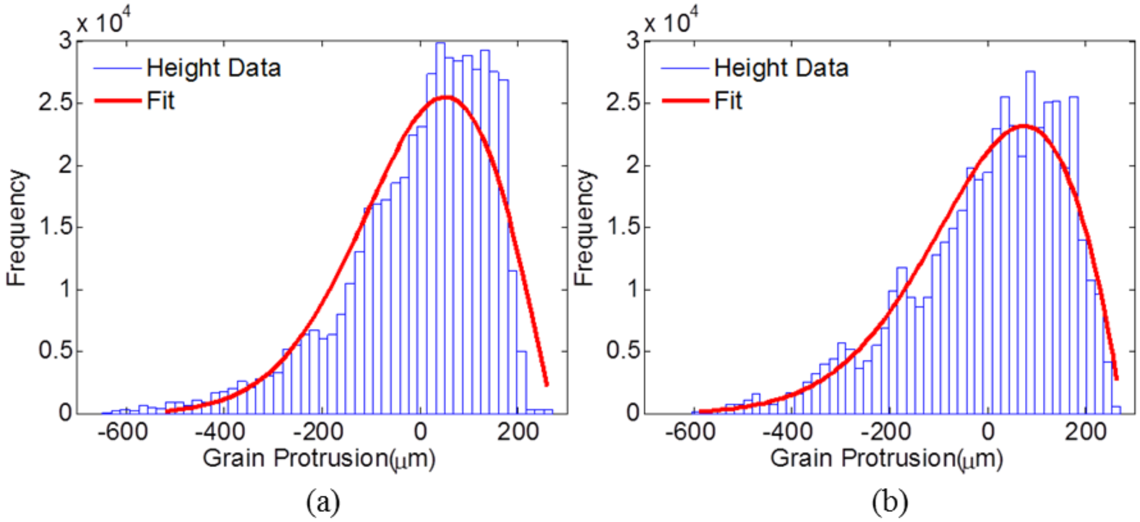

Figure 4.14 – Pre- and post-dressing height distributions for 50 µm infeed and 0.25 mm/rev lead and overlap ratio of 3

Figure 4.15 summarizes the effects of dressing parameters on the skewness and kurtosis of the surface height distribution. Each data point in the plot was generated using the following procedure. The beta distribution for the particular dressing condition was sampled 10,000 times to obtain surface heights that were used to compute the corresponding skewness and kurtosis parameters. The entire process was repeated 10,000 times and the overall mean skewness and kurtosis parameter values and their standard deviations were computed and plotted. This procedure ensures a statistically rigorous evaluation of the effects of dressing parameters on the shape parameters of the surface height distribution.

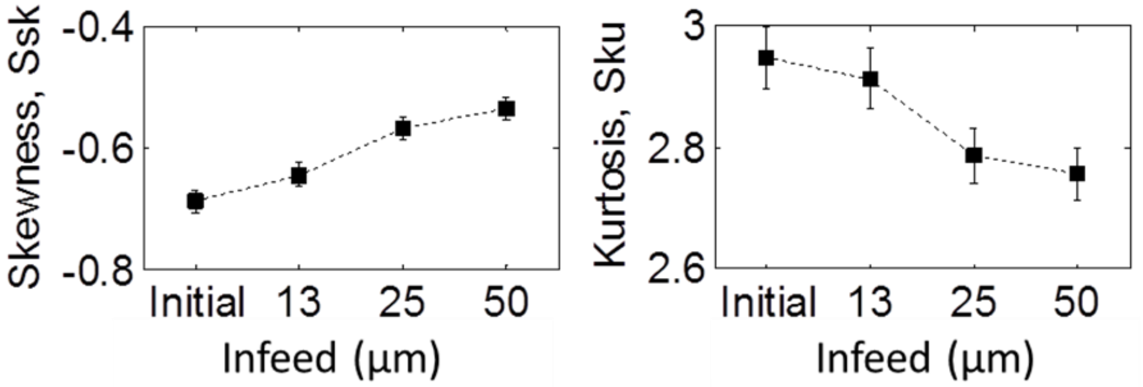

(a) Effect of Infeed

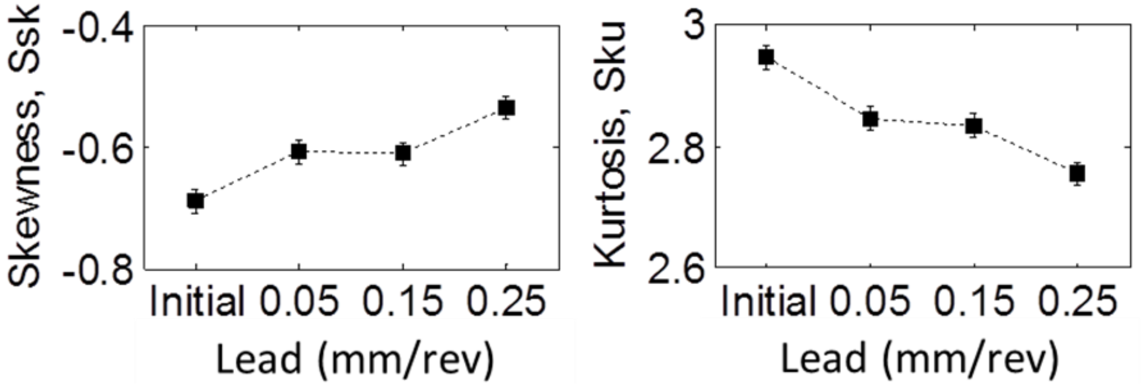

(b) Effect of Lead

Figure 4.15 – Quantitative effects of dressing parameters on the SG height distribution characteristics: (a) effect of infeed for lead of 0.25 mm/rev, (b) effect of lead for infeed of 50 μm.

Figure 4.15a illustrates the effect of infeed on the surface topography height distribution when holding the lead constant at 0.25 mm/rev and varying the infeed from 13 to 50 µm, compared to the initial wheel surface. The skewness becomes less negative with increase of infeed. It appears that there is a slightly larger change in skewness when the lead is varied from 13 to 25 µm than from 25 to 50 µm. The kurtosis is seen to decrease i.e. the distribution becomes less peaked with increase of infeed. These trends demonstrate how both infeed and lead have similar effects on the surface height distribution.

Figure 4.15b illustrates the effect of lead by holding the infeed constant at 50µm and varying the lead between 0.05 and 0.25 mm/rev. In this case, the skewness increases more aggressively from initial to 0.05 mm/rev and then 0.15 to 0.25 mm/rev (with minimal change from 0.05 to 0.15 mm/rev) compared to varying the infeed. The kurtosis experiences little change between 0.05 and 0.15 mm/rev but is affected when the lead is increased to 0.25 mm/rev. The foregoing results suggest that the surface topography is transforming from a dull, plateaued surface that would be expected to yield high grinding forces to a sharper surface topography that would increase the grinding efficiency.

Figure 4.16 illustrates how the shape and size of the surface height distributions vary with different dressing conditions and closely matches the results in Figure 4.15. Each case compares the effects of the infeed and lead to an undressed wheel height distribution after fine, medium, and course dressing conditions. The undressed wheel is also known as the *initialized* wheel in this study. In each case, the *initialize*d wheel appears to have the highest negative skewness and more positive kurtosis meaning that there are deeper valleys present on the wheel surface.

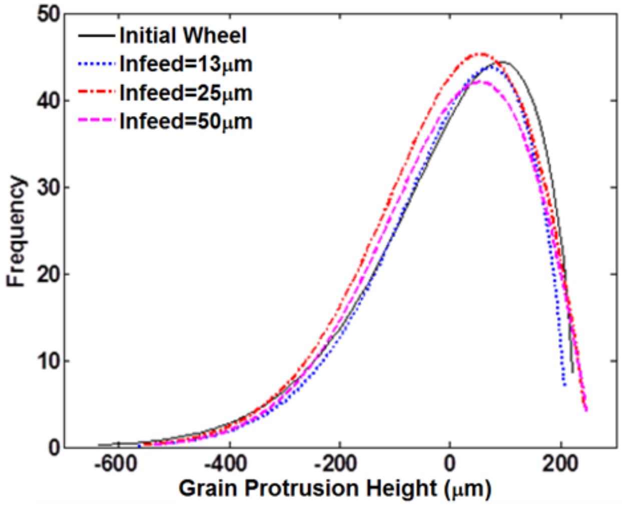

(a) Effect of Infeed (Lead held at 0.25 mm/rev)

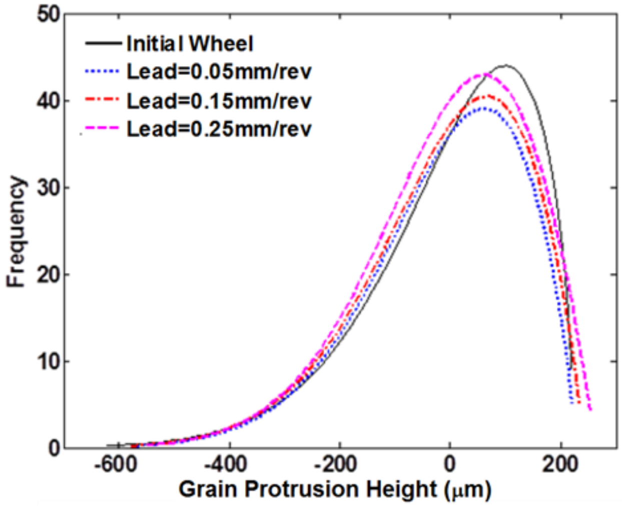

(b) Effect of Lead (infeed held at 50μm)

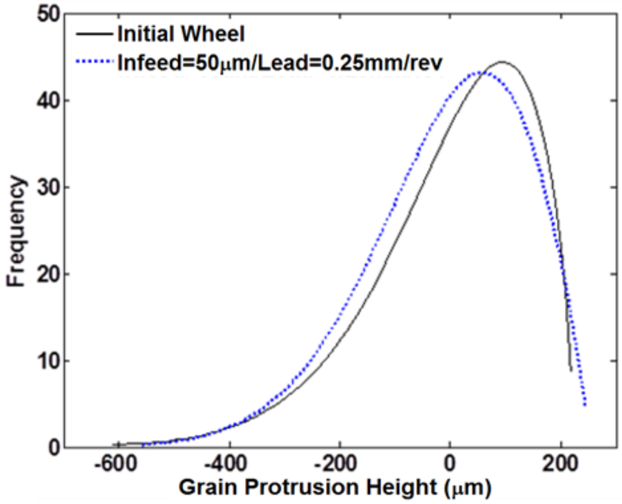

(c) Effect of Max. Infeed and Lead

Figure 4.16 – Effects of dressing parameters on the SG height distribution curve

Figure 4.16a qualitatively compares the height distribution of an undressed grinding wheel to the effect of the infeed dressing parameter when holding the lead constant at 0.25 mm/rev while increasing the infeed from 13 to 50 µm . The distribution shifts more to the left side of the plot indicating a more positive skewness when increasing the infeed dressing parameter, indicating a decreasing amount of grinding wheel material above the reference datum (peaks being removed). The trend appears more aggressively during coarse dressing compared to fine dressing. The distribution also becomes less peaked indicating a lower kurtosis during coarse dressing obtained by increasing the infeed.

Figure 4.16b illustrates the effect of lead by holding the infeed constant at 50µm and varying the lead between 0.05 and 0.25 mm/rev. The effect of infeed shifts the bulk of the material of the grinding wheel closer to the reference datum indicating the skewness becomes less negative. The distribution becomes less peaked with a coarser dressing parameter of 0.25 mm/rev confirming that the lead affects the skewness more than the kurtosis. The effects of maximum lead and infeed are illustrated in Figure 4.16c. This is the most aggressive dressing condition and demonstrates a slightly less negative skewness and a less peaked height distribution indicating a lower kurtosis.

4.5.3.2 Area and Volume Parameters

Figure 4.17 shows the schematic and definitions of the bearing area or the areal material ratio curve. The bearing area curve is derived from the areal material ratio curve based on the ISO 13565-2:1996 Standard. The linear areal material ratio curve parameters, otherwise called *Sk* family parameters, are derived from three sections of the areal material ratio curve: the peaks above the main plateaus, the plateaus themselves, and the deep valleys between the plateaus [88]. The volume parameters are generally a good indicator of wear and tribological properties of a surface. The bearing and volume parameter main effect plots for the experimental runs relating to the dressed grinding wheel surface topography are shown in Figure 4.18.

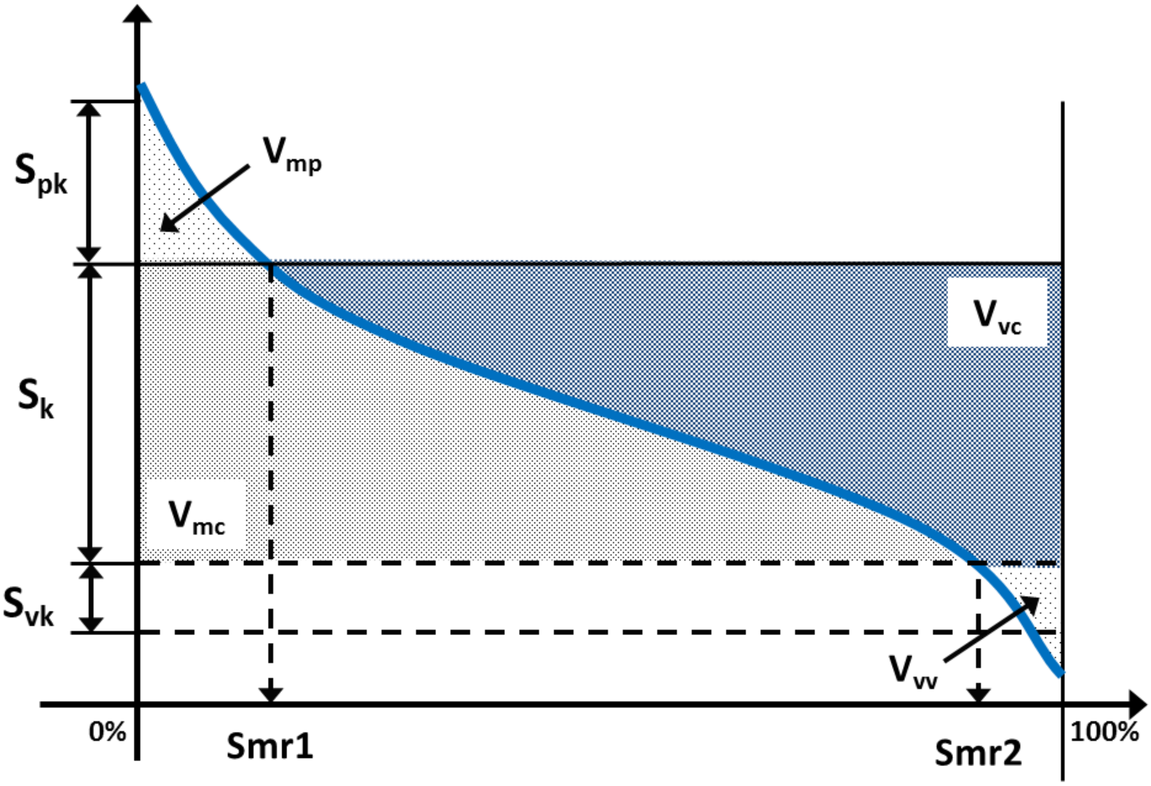

Figure 4.17 – Bearing and volume parameters

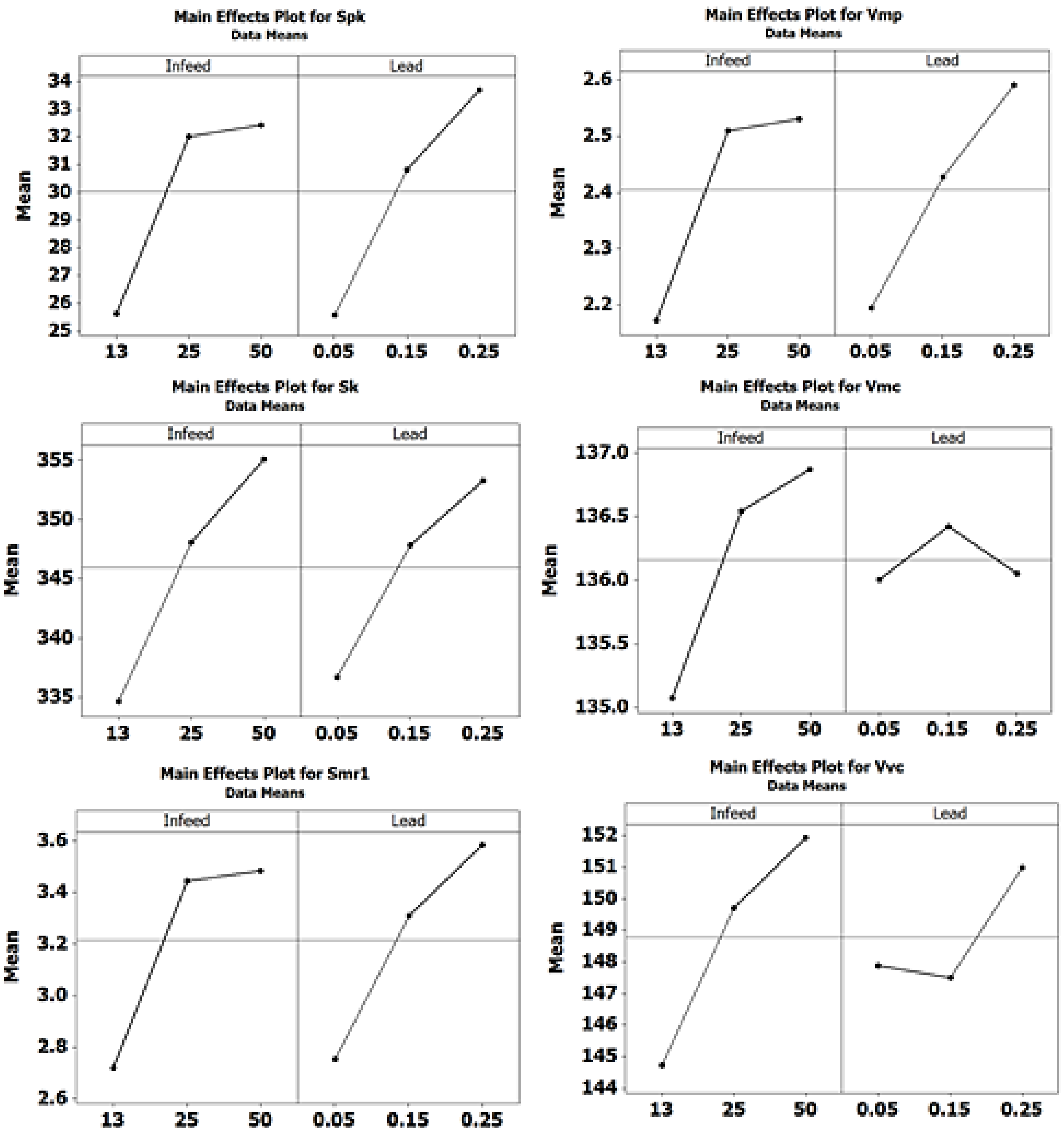

Figure 4.18 – Relevant bearing and volume area main effect plots

In regards to the bearing area parameters, it is logical that the dressing parameters of infeed and lead affect the peak height (*Spk*), core roughness depth (*Sk*), and the peak material component (S*mr1*) more than the valley height (*Svk*) and the lower fraction of the material component (*Smr2*) since the single point dresser interacts mainly with the surface of the grinding wheel. The parameters increase with increasing infeed and lead when the reference plane is re-calculated since the surface becomes rougher and more peaks are exposed after dressing. These parameters are also affected in different ways during aggressive dressing due to the following two phenomena. The first is macro-fracture when large sections break-off from the grain exposing fresh, sharp cutting edges. The second is total dislodgement of grains creating a void (or a valley) that impacts both the bearing and volume parameters. The *Sk* and *Vmc* parameters would generally not be expected to change much since there is little interaction of this region of the surface with the diamond dresser. The shift in the reference plane causes the *Spk*, *Vmp*, and *Smr1* parameters to change. The core material volume of the surface *Vmc* shows an interesting trend. Increasing the lead from 0.05 to 0.15 mm/rev increases its magnitude, but then lowers it when the lead is further increased to 0.25 mm/rev.

4.5.4 Resulting Surface Topography

Figure 4.19 shows three-dimensional views of the pre- and post-dressing wheel surfaces corresponding to the surface shown in Figure 4.12 and illustrates how the reference plane (gray section of Figure 4.19) adjusts and how the surface changes with the aggressive dressing condition. The pre-dressed (or initial) condition has more plateau structures as observed in Figure 4.19a, which will cause more rubbing than cutting during grinding leading to higher grinding forces [99]. Recall that the pre-dressing condition represents very fine dressing and is chosen to create an initial surface that acts as a ‘clean slate’ for each dressing test. The aggressive dressing condition transforms the dull grain structures into sharper cutting edges as seen in Figure 4.19b.

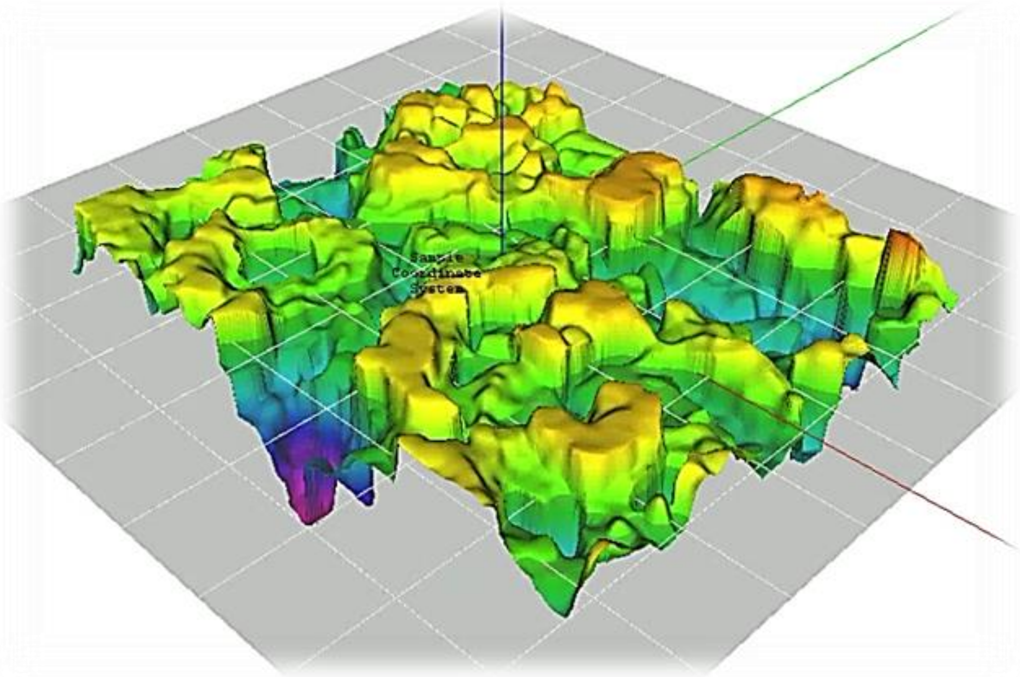

(a) Pre-Dressing

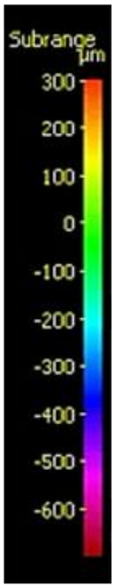

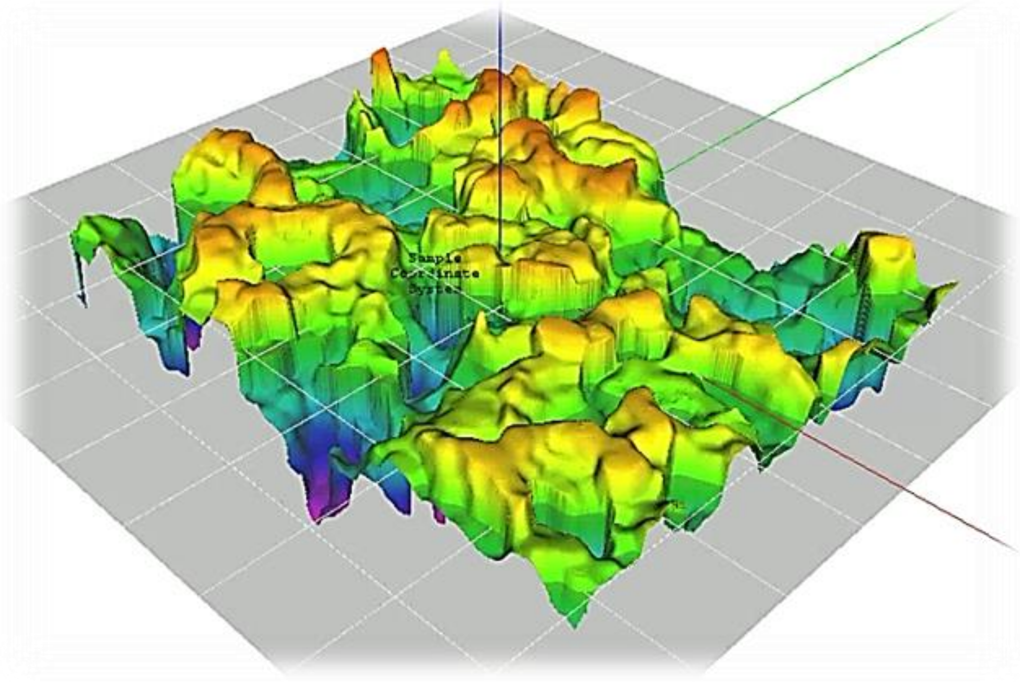

(b) Post-Dressing

Figure 4.19 – Three-dimensional view of wheel surface for 50 µm infeed and 0.25 mm/rev lead

4.6 SUMMARY

A full factorial DOE, of single point dressing, was utilized to determine the effects of the lead and infeed dressing parameters on the SG grinding wheel surface topography. The effects of the dressing parameters were determined by studying the changes in amplitude, volume, and area parameters of the grinding wheel surface topography throughout the experimental process. The custom precision wheel relocation apparatus enabled visualization of the micro geometric alterations of the wheel surface as a function of dressing.

The amplitude parameters chosen to describe the surface during the dressing process are best summarized by the surface texture height distribution. The change in dressing conditions affects the shape of the surface texture height distribution, which follows a negatively skewed beta distribution with shape parameters of α and β that consistently change based on the dressing condition. Some other findings include that more aggressive dressing conditions increase *Sp* and *Ssk* while *Sku* decreases.

The lead dressing condition appeared to have a stronger influence on the area parameters along with the volume parameters. It was observed that the decrease of *Vmc* and increase of *Vvc*, during aggressive dressing conditions, show evidence of grain macro-fracture and dislodgment.

The single point dressing study showed that the infeed and lead have a significant effect on the SG wheel surface. These findings are expected to be very useful in formulating more accurate models of SG wheel surface topography and its generation during single point dressing.

5. WHEEL TOPOGRAPHY MODELING

To accurately model a grinding wheel, it is important to properly characterize the grinding wheel by its attributes including grain size and shape. It is then necessary to accurately distribute the simulated grains in both horizontal and longitudinal directions. The grinding wheel used in this study is composed of a large number of abrasive grains randomly placed in the wheel and these are held together by a ceramic glass binder.

5.1 TOPOGRAPHY MODEL OVERVIEW

This work introduces a stochastic model for the simulation of three-dimensional wheel surface topography under different dressing conditions with a focus on the first layer of a vitrified wheel using statistical descriptors found from experimental trials. Feasibility of this stochastic model is indicated by the validation of the comparison to the actual wheel in the validation chapter of this thesis.

A model is defined as the abstract representation of a process which serves to link causes and effects [100] and in the present context is basically establishing a relationship between the inputs and outputs to describe the effect of the dressing process on the wheel surface topography. Stochastic models are versatile numerical models used to simulate systems that are inherently probabilistic, through random sampling [8]. This technique is chosen since the micro-fracture and/or dislodgement of an abrasive grain from the bond is complex and depends on many random factors such as dressing load, extent of adhesion between the bond and the grain, and stress concentrations at the grain-bond interface [8].

The flowchart of the algorithm developed to simulate the wheel surface topography is shown in Figure 5.1. The creation of the wheel surface topography is divided into four main steps including: i) initialize the grinding wheel area of concern, ii) create individual grain geometry, iii) designate grain spatial orientation, and iv) fill the wheel topography with bonding material after the grains have been instantiated.

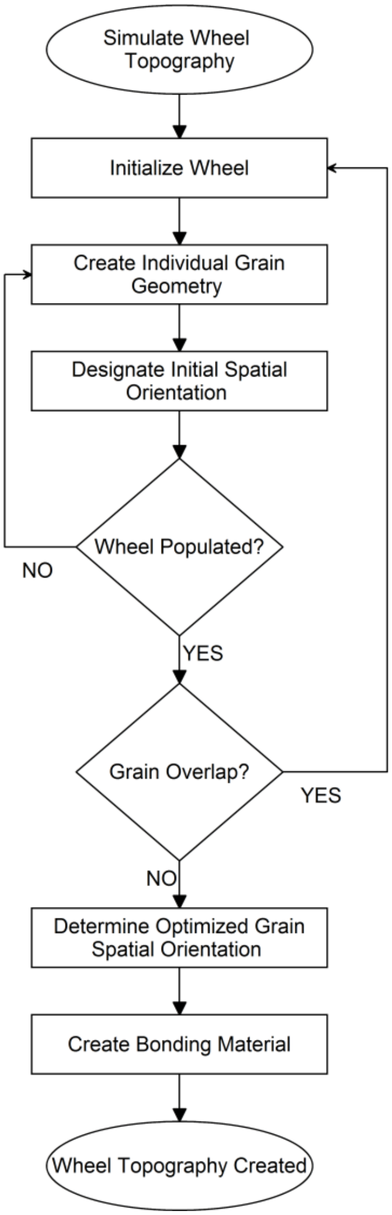

Figure 5.1 – Wheel topography algorithm

Initialization includes aspects of calculating the simulated grinding wheel specifications. This is then used to calculate the correct number of grains with the correct attributes, including size and shape. Spatial orientation places the created grains in an initial lattice type structure to be further optimized to the proper location in all three dimensions along with designated rotational control. Once populated, the bonding material in the space between grains is created. Each major level of the wheel surface topography algorithm is explained in detail in the following sections.

5.2 INITIALIZE MODELING AREA

It is first necessary to calculate the number of grains in the area of concern. The number of grains is determined by a number of factors including the length/width of the area along with contributors from the physical makeup of the grinding wheel being modeled. The rectangular area of concern used to model the wheel topography consists of a 2.2 mm x 2.8 mm region.

5.2.1 Grinding Wheel Specifications

The grinding wheel standard marking system provides the needed attributes about the grinding wheel and describes, via code, information regarding i) type of abrasive, ii) size of abrasive grain, iii) hardness of grinding wheel, iv) wheel structure number, and v) bond type. Figure 5.2 illustrates the marking system for conventional grinding wheels defined by the American National Standard Institute (ANSI) by Standard B74.13-1977. The particular wheel used in the experiments, modeling, and validation of this work was a 5SG46-JVS. This code is slightly different from conventional wheels and indicates that the wheel is:

- 50% SG grains and 50% Aluminum Oxide
- 46 grit abrasive
- Medium (J) grade
- Vitrified bond material

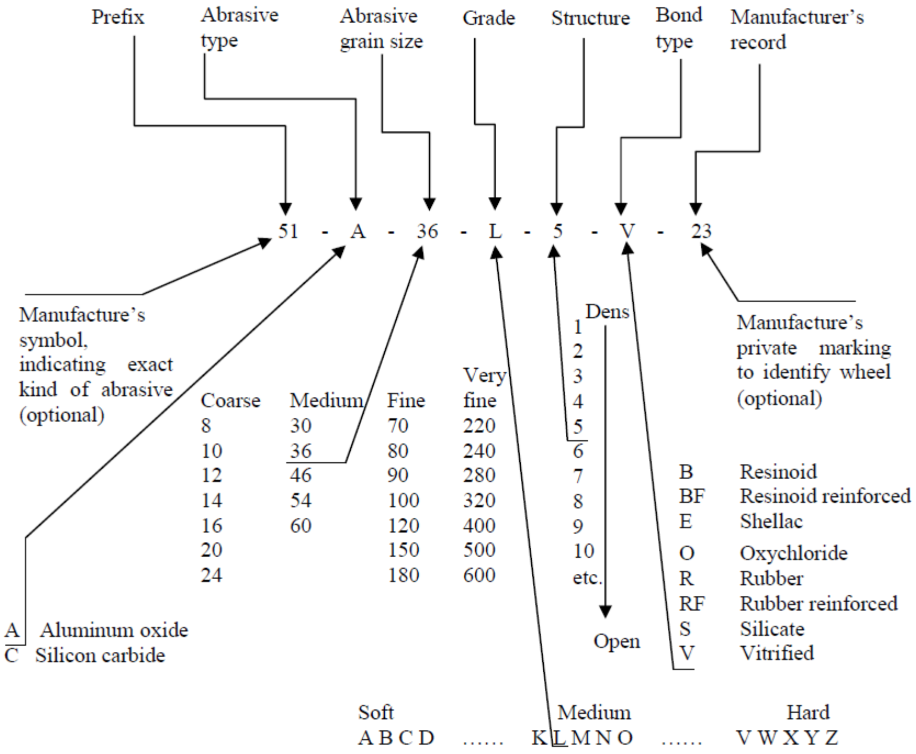

Figure 5.2 – Standard grinding wheel marking system [81]

The total volume of wheel consists of abrasives, the bonding material, and void space (porosity) between the grains. The grains and bonding material are illustrated in Figure 5.3a while the porosity is slightly more difficult to distinguish in two dimensions, so it is better represented in part b of the figure which shows a pseudo contour map of the wheel surface where the peaks and valleys are better illustrated. This information depends on the hardness and structure number of the standard marking system of grinding wheels.

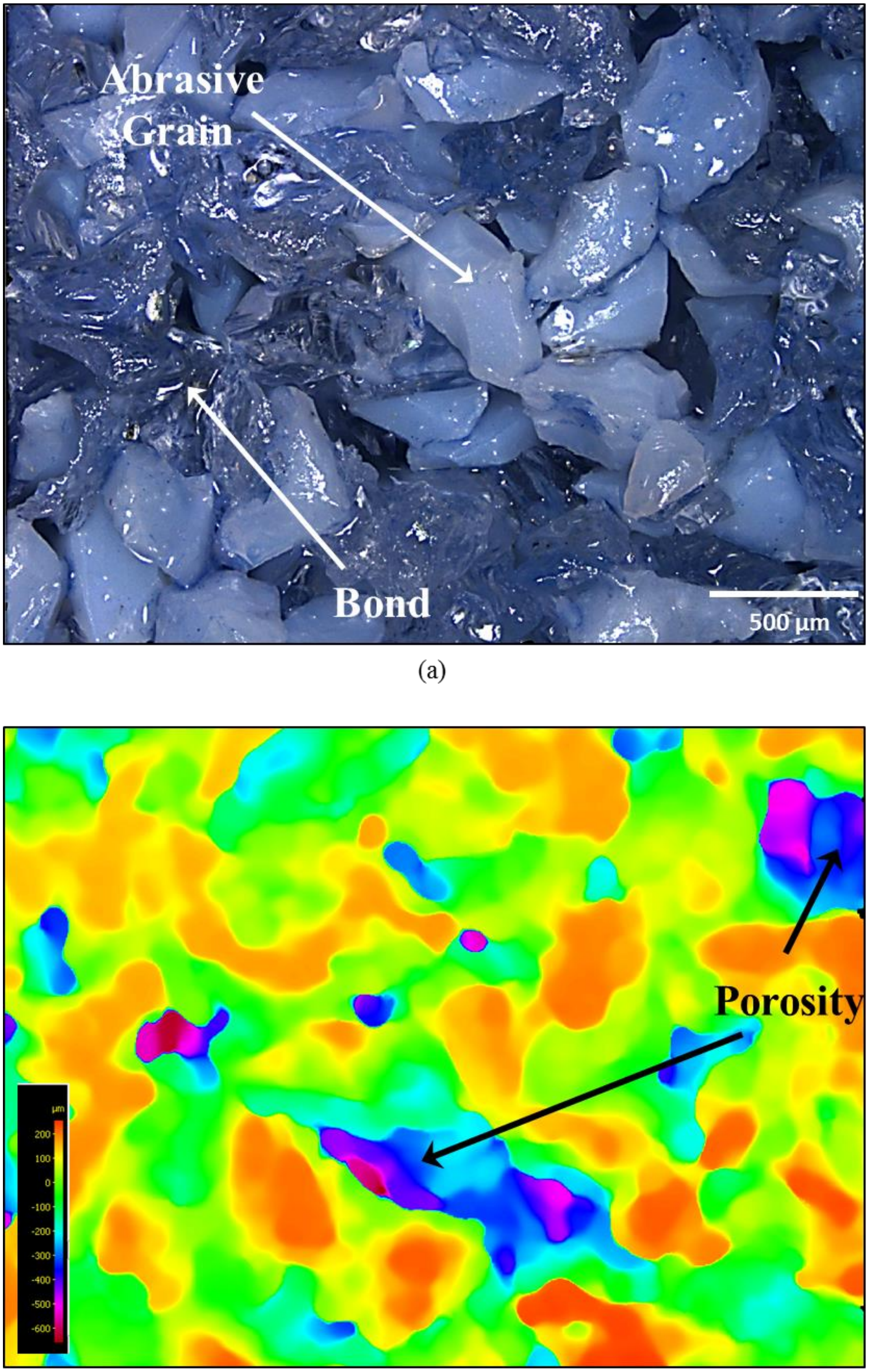

(a)

(b)

Figure 5.3 – SG grinding wheel composition

The wheel structure is specified by the relative proportions of grains, bond material, and voids between the bond and grains (otherwise known as volume percent). Wheel grade is a gauge of the bond materials' strength that holds the grain within the bonding material. The type of bond and volumetric proportion determines the wheel grade. Softer grade wheels are used for lower material removal and harder workpiece materials while harder grades are generally used for higher material removal and softer workpiece materials.

5.2.2 Number of Grains

The rectangular area of concern used to model the wheel topography consists of a 2.2 mm x 2.8 mm region, which was chosen to match the field of view of the Alicona focus variation equipment used in the experimental work. To calculate the average number of grains, it is necessary to first calculate the grains per unit length within the wheel given by [56]

$$N_l = \frac{{V_g}^{1/3}}{d} \tag{5.1}$$

where *d* is the mean grit diameter and V_g is the volume fraction of grit in the wheel and is calculated using [57]

$$V_g = 2(32 - S)\% \tag{5.2}$$

where *S* is the structure number of the wheel. The abrasive grain size of a grinding wheel is determined by the number of openings per unit length in a sieve. The mean grain diameter can be determined as [61]

$$d_{mean} = 28.9g^{-1.18} \tag{5.3}$$

with g as the nominal grain size. Hou *et al.*'s [61] work also provides tables of the maximum and minimum grain diameters based on sieve size. The average number of grains per unit area is then calculated by squaring the grains per unit length [56]

$$N_s = N_l^2 \tag{5.4}$$

The average number of grains per area N_s for this wheel ended up being 42 grains for the particular wheel simulated in this thesis using a structure number of 12 obtained from the manufacturer's literature. The next steps in the simulation are to create and characterize each of the 42 grains. After the grains are modeled, they will be placed within the volume of the simulated grinding wheel.

5.3 INDIVIDUAL GRAIN MODEL

The actual simulation of the topography of the grinding wheel begins with the creation of the individual abrasive grains. Two main considerations when creating grains are the size and shape of the grain, which are inseparable characteristics when describing particles with random and indeterminate shape [101]. To work effectively, particles suitable for use as abrasives must meet two criteria including: i) must be significantly harder (by at least 20%) than the workpiece material and ii) must possess size and shape attributes that promote material removal [6]. The grains of the SG wheel used in this work are modeled as polyhedrons.

5.3.1 Abrasive Grain Size

The individual grains are simulated by first determining the circumscribed diameter of the polyhedron, aspect ratio, and then calculating the number of sides. Usually grain sizes determine the resulting surface finish of the workpiece and should be considered when choosing the grinding wheel. Smaller size grains produce finer/smoother surfaces while larger grains produce higher material removal resulting in a coarser surface. The circumscribed diameter is confirmed to follow the Gaussian distribution as shown in Figure 3.9 of the characterization chapter and also assumed by many researchers [8], [61]. Figure 5.4 is a plot of the mean grain diameter versus the nominal grain size with a fitted line for mean grain diameter d_{mean} experimentally determined by Hou [61].

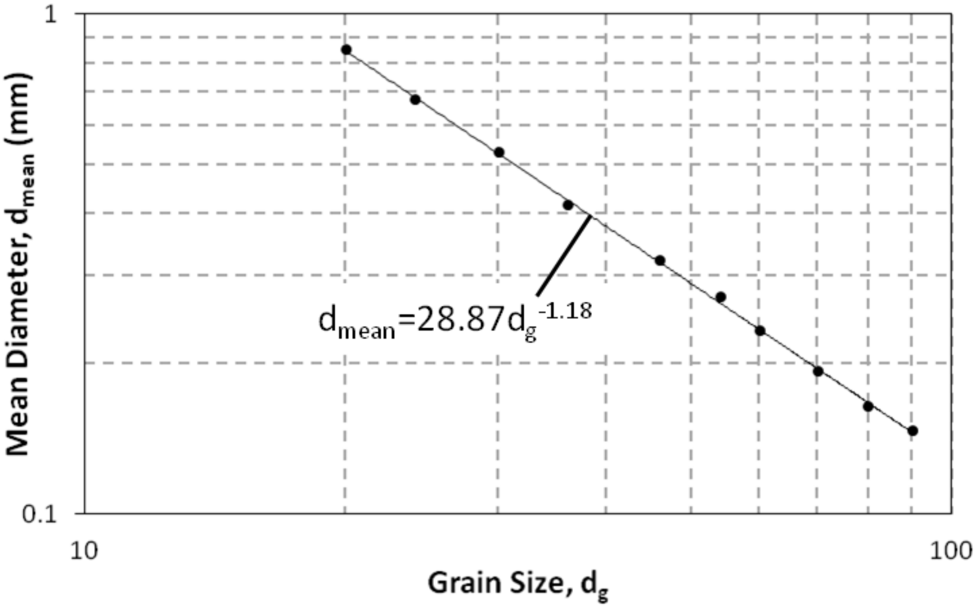

Figure 5.4 – Mean grain diameter versus nominal grain size [61]

The range of grain sizes is related to the wheel marking. The grain size listed in the wheel’s standards corresponds to the sieve used to sift the grain during the fabrication of the grinding wheel. The sieving process involves passing the abrasive grains through a stack of standard sieves consisting of a coarser mesh in the top to finer meshes in the bottom. Coarse grains range from 8 to 24, medium from 30 to 60, fine from 70 to 180, and very fine from 220 to 600. Sieving is generally used for sizing of conventional abrasive grains coarser than 240 grit size [56]. The grain used in the experiments and simulation was a medium 46 grain size. The related sieve size allows this model to have a grain diameter that follows a truncated normal distribution, meaning 99.7% of the grains in the grinding wheel have a size of (d_{gmin},d_{gmax}) [102] and is expressed as [8], [54]

$$P(d_{gi}) = \frac{A_1}{\sigma_g\sqrt{2\pi}} exp\left[-\frac{1}{2}\left(\frac{d_{gi}-d_g}{\sigma_g}\right)^2\right] \qquad d_g^{min} < d_{gi} < d_g^{max} \tag{5.5}$$

where d_g is the mean grain size and σ_g is the standard deviation of the grain size. The minimum and maximum of grain diameters is based on the sieve size for more popular grains and follows Table 5.1.

Table 5.1 – Size of sieve openings [61]

Grain Size (#)	20	24	30	36	46	54	60	70	80	90	100
Sieve Opening (mm)	0.938	0.762	0.589	0.476	0.354	0.291	0.255	0.211	0.178	0.152	0.142
d_{max} (mm)	0.938	0.762	0.589	0.476	0.354	0.291	0.255	0.211	0.178	0.152	0.142
d_{min} (mm)	0.762	0.589	0.476	0.354	0.291	0.255	0.211	0.178	0.152	0.142	0.114
d_{mean} (mm)	0.850	0.676	0.532	0.415	0.323	0.273	0.233	0.194	0.165	0.147	0.128

As stated earlier, there are 42 grains in the particular grinding wheel considered here. The circumscribed diameter for each grain is calculated by sampling a truncated Gaussian distribution using Equation 5.5. The minimum d_g^{min} and maximum d_g^{max} truncation limits are controlled by the grain size as listed in Table 5.1. For a grain size number of 46, the smallest grain would be 291 µm and the largest circumscribed diameter would be 354 µm resulting in a mean size of 323 µm. Now, once the circumscribed diameters are determined for each grain, it is necessary to characterize the grain shape.

5.3.2 Abrasive Grain Shape

The shape of the abrasive grain is very complex and must be modeled as accurately as possible for proper interaction since grain shape has an impact on the grain strength and grinding performance. It should be noted that using polyhedrons is not a new approach and has been used in other models [66], [84] .

One of the main attributes of the grain shape is its sharpness. Particle sharpness is related to shape and can be broadly defined as the geometrical property of an abrasive tip or body that influences the strain induced in the wearing surface under loaded contact [64]. The aspect ratio and number of sides (facets) of the grains are discussed in the following sections.

5.3.2.1 Aspect Ratio

The measured aspect ratios range from 1:1 to 1:7 and are found to follow the Weibull distribution with a shape parameter of 1.11 and a scale parameter of 1.08. Let X represent the aspect ratio. The probability density function of the Weibull distribution function is mathematically represented by [103]

$$f(x) = \left(\frac{\beta}{\theta}\right)\left(\frac{x-\gamma}{\theta}\right)^{\beta-1} e^{-\left(\frac{x-\gamma}{\theta}\right)^{\beta}} \tag{5.6}$$

where β is the shape parameter, θ is the scale parameter, and γ is a threshold parameter and all quantities are positive. The threshold parameter shifts the beginning point away from zero to allow the model to be used when it practically can’t begin at zero and was necessary for modeling the aspect ratio. The aspect ratio affects the size of grains and it is also assumed that the above stated grain diameter refers to the smaller dimension of the grain due to the fact that the grain can fall through the sieve when oriented along its length direction.

5.3.2.2 Number of Facets

The number of facets (sides) of the abrasive grain in the experimental trials ranged from four to ten with a mean value of seven and was found to follow a gamma distribution with a shape parameter β of 0.663 and a scale parameter η of 4.58. The gamma distribution probability density function is given by [104]

$$f(x) = \frac{1}{\eta\Gamma(\beta)}\left(\frac{x}{\Gamma}\right)^{\beta-1} e^{-\frac{x}{\eta}} \tag{5.7}$$

where η is the scale parameter, $\Gamma(\beta)$ is the gamma function evaluated at the shape parameter β given by

$$\Gamma(\beta) = \int_0^\infty t^{\beta-1}e^{-t}dt \tag{5.8}$$

The scale and shape parameters are both positive values for this distribution.

5.4 INDIVIDUAL GRAIN SPATIAL ORIENTATION

A wheel has a mass of geometrically undefined cutting points which are irregularly distributed on its working surface and which are presented to the workpiece at random orientations and positions. Past works have not quantitatively described the spatial orientation of grains on the wheel working surface. This is because it is very difficult to quantify the distribution of spatial attitude of grain cutting edges on the micron-scale wheel protrusion topography [105]. At this point of the model, the grains and simulated area have been calculated and created. Now it is time to orient them in space within the concerned area. The grains are first placed in an *initial* lattice type structure and then the spacing between the grains is *optimized*, following the algorithm previously presented in Figure 5.1, with the attributes following the experimental findings in Chapter 4. Determining the *initial* spatial orientation follows the steps illustrated in Figure 5.5 and is divided into two main categories: i) designating the grain height and ii) angle of rotation. The three-dimensional grains, represented as polyhedrons, are then converted into two-dimensional polygons, by projecting the grains onto the x-y plane, for final optimized grain placement within the grinding wheel. It is necessary to translate the polygons to the original lattice layout due to the new centroid of the projected polyhedron.

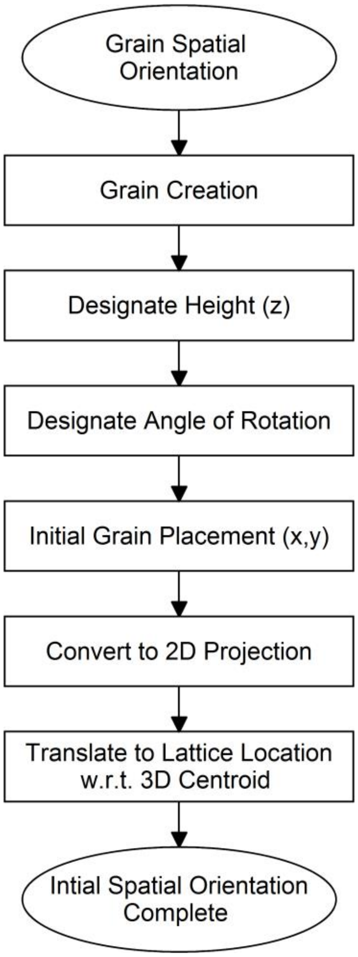

Figure 5.5 – Algorithm for initial spatial orientation

5.4.1 Height Designation

The next important step in the stochastic model is the grain spatial orientation in both the horizontal and vertical directions. The location in the vertical direction is determined, as explained in this section, and referred to as the height of the tip of the grain in the z-direction. The heights of the grains follow the negatively skewed beta distribution shown in Figure 5.6. The grain height distribution was determined from the grain protrusions measured using the Alicona instrument as described in the characterization chapter. Rockwell Arena Input Analyzer software was used to fit the statistical distributions to the surface height measurements. The probability density function of a generalized beta distribution defined on the interval [*L*,*U*] with the shape parameters *a* and *b* is given by [106]

$$f(x, a, b, L, U) = \frac{1}{(U-L)\cdot B(a,b)} \left(\frac{x-L}{U-L}\right)^{a-1} \left(1 - \frac{x-L}{U-L}\right)^{a-1} \tag{5.9}$$

with $0 < a$, $0 < b$, $L \leq x \leq U$. The beta function *B(a,b)* is then defined as

$$B(a, b) = \int_0^1 z^{-1} 1 - z^{b-1} dz \tag{5.10}$$

The parameters *a* and *b* are independent of each other and describe the shape of the distribution of height measurements of the grinding wheel.

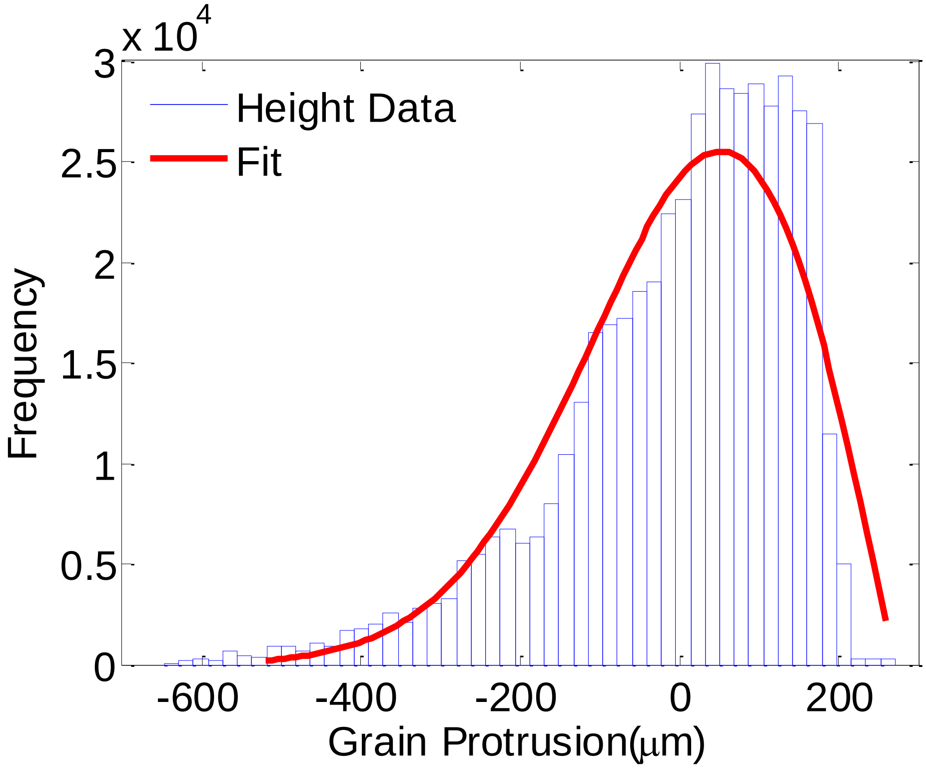

Figure 5.6 – Grain height distribution

The shape parameters *a*, *b* are then calculated by using the mean height value $\bar{z}$ and the variance of the distribution σ^2

$$a = \frac{\bar{z}}{\sigma^2}(\bar{z} - \bar{z}^2 - \sigma^2) \tag{5.11}$$

$$b = \frac{(1-\bar{z})}{\sigma^2}(\bar{z} - \bar{z}^2 - \sigma^2) \tag{5.12}$$

The values for *a*, *b* are found from the experimental trials for each dressing condition and are listed in Table 5.2.

Table 5.2 – Beta parameters

Condition	Min (L)	Max (U)	a	b
Undressed	-627	847	4.49	1.60
1	-620	831	4.54	1.71
2	-620	838	4.48	1.69
3	-619	831	4.55	1.75
4	-624	799	4.87	1.79
5	-610	840	4.50	1.93
6	-609	860	4.41	1.89
7	-608	833	4.46	1.81
8	-620	863	4.29	1.75
9	-598	858	4.52	2.01

The beta distribution is not a commonly used distribution to describe the amplitude distribution for grinding wheels but has been used to describe trends in machined surfaces [107], [108]. The beta distribution is a flexible distribution that can produce a unimodal, uniform, or bimodal distribution of points that can be either symmetrical or skewed.

It is possible to use an areal surface modification of Whitehouse's theory of replacing the mean height value with maximum peak *Sp* and the variance of the distribution with the maximum peak valley *Sv* [107] for the beta distribution shape parameters. This modification results in

$$a = \frac{Sv(SvSp - Sq^2)}{SzSq^2} \tag{5.13}$$

$$b = \frac{Sp(SvSp - Sq^2)}{SzSq^2} \tag{5.14}$$

where *Sz* is the maximum height of the selected area and *Sq* is the root mean square height of the selected area. The advantage of using Equations 5.13, 5.14 is that the beta distribution shape parameters can be calculated as a function of the areal height parameters.

The final simulated surface topography of the grinding wheel is influenced by the dressing conditions. The actual wheel topography is generated by the process of grit and bond fracture caused by the interaction of the dressing diamond and the grinding wheel. This model simulates the change of surface texture heights by controlling the beta distribution parameters, from Table 5.2, which vary with the dressing. Since the grains have been created and the height of each grain is determined, it is now necessary determine the angle of rotation for each grain and then establish the *initial* grain layout.

5.4.2 Angles of Rotation

In the actual wheel, the grains are randomly oriented relative to the normal to the wheel surface. Grain rotation is accomplished by rotating the grain axis of orientation using a stochastic distribution where the angles of rotation are assumed to follow a discrete uniform distribution determined using a random number generator. The rotational angles of roll, pitch, and yaw are visually defined in Figure 5.7. The resulting angles are ‘equally likely’ and are mathematically described by Krishnamoorthy [109]. The probability function of a discrete uniform random variable *X* is given by

$$P(X = k) = \frac{1}{N} \tag{5.15}$$

with $k = 1, \ldots$ N and the cumulative distribution function is given by

$$P(X \leq k) = \frac{k}{N} \tag{5.16}$$

The mean and variance of the discrete uniform distribution can be obtained using

$$\mu = \frac{k(k+1)}{2} \tag{5.17}$$

$$\sigma^2 = \frac{k(k+1)(2k+1)}{6} \tag{5.18}$$

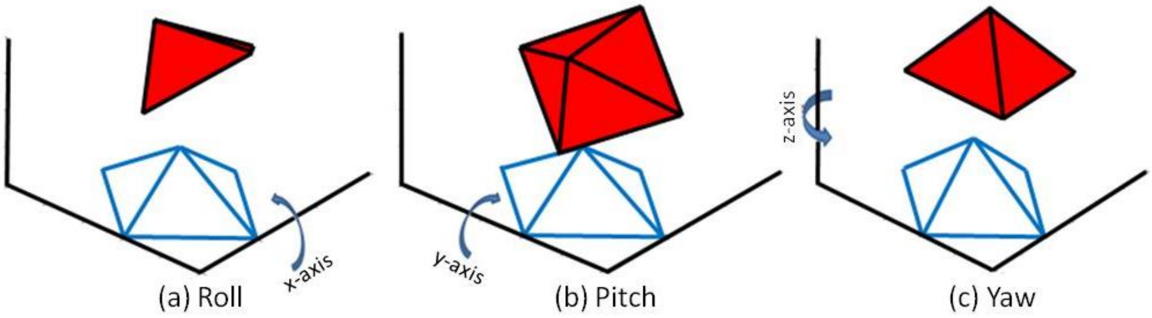

Figure 5.7 – Rotation control of grain

5.4.3 Initial Grain Placement

The grains are initially located in a regular lattice structure as shown in Figure 5.8a, similar to the model presented by Baseri [56]. The spacing between the grains δ_o of the initial grain layout is calculated by

$$\delta_o = \frac{1}{N_l} \tag{5.19}$$

where N_l is from Equation 5.1. The coordinates for each grain in the rectangular layout of sides L_x and L_y of the wheel section are given by

$$x_m = i\delta \tag{5.20}$$

$$y_m = y_0 + j\delta \tag{5.21}$$

where i, j are values between zero and integer values of L/δ. The layout of the rectangular simulated area is 2.8mm in the circumferential direction of the wheel and 2.2mm in the radial direction of the wheel. These dimensions were chosen to match the measurement equipment's field of view using 5x magnification optics. The simulation takes a different approach from this point onwards compared to Baseri [56] since he just varied the spacing by a random multiplication factor and then checked for grain overlap. In contrast, the approach used in this work is to apply spatial distribution based on information experimentally determined in the Characterization chapter and applied to the simulation in the following section.

5.4.4 Three-Dimensional to Two-Dimensional Transformation

To simplify the calculations, the geometry is first transformed into two-dimensional polygonal shapes by computing the convex hull of all sides of the three-dimensional projection of the grain on the $z = 0$ plane using a built-in MATLAB function. The result of this procedure is illustrated by the Figure 5.8b. Due to the new centroid location compared to the center of the origin of the grain geometry, the two-dimensional polygon is located at the designated x_i,y_i location resulting from Equations 5.20 and 5.21.

This completes the initial spatial orientation. The creation of the geometry has its origin at x_0,y_0 from Equations 5.20, 5.21 and the algorithm is looped through the grain creation process until the wheel surface is populated with the proper number of abrasive grains calculated in Equation 5.4.

Once the surface has been populated with the initial spatial orientation of grains (presently modeled as polygons), it is necessary to check the grains for overlap since two grains cannot occupy the same space. An algorithm was created to check the intersection of polygons by looking at the four closet neighbor's method. This means that the center grain looks at the cardinal directions (north, south, east, and west) and checks for intersection by using an algorithm incorporated a function that tests for overlap of polygons [110]. An example of this procedure for a particular grain is illustrated by the highlighted grains in Figure 5.8b where the grain of interest is black and its four neighbors are blue. If there is overlap, the grains are recreated and the surface area of concern is reconstructed with new geometries. This is generally not an issue, but high aspect ratio grains may cause overlap issues if they are in close proximity.

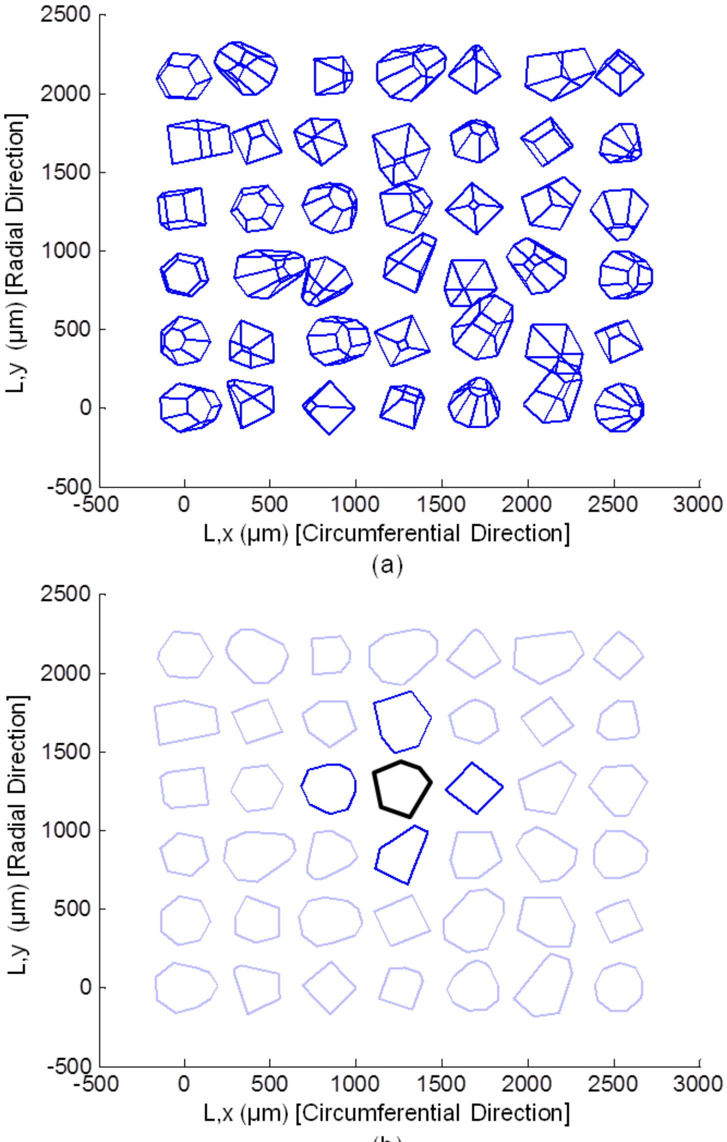

(a)

(b)

Figure 5.8 – 3D to 2D grain transformation

5.5 OPTIMIZED SPATIAL ORIENTATION

The previous sections oriented the simulated abrasive grains in a uniformly spaced lattice type layout. This section deals with optimization of the modeled wheel surface topography and follows the flowchart of the algorithm shown in Figure 5.9. This is an important aspect of the creation of the wheel surface when deciding the distance between abrasive grains on the surface of the grinding wheel. Some researchers just model the grains as uniformly spaced [7], [74]while others add some uniform random [4], [67] offset to the lattice structure of the grains. This research proposes a method of granular spatial separation based on actual measurements. A small portion of the SG grinding wheel was evaluated using micro-tomography (μCT). A GE Preclinical eXplore Locus micro-CT machine was used to optically slice the wheel in 20 μm increments. Spacing between the grains was calculated and found to follow a beta distribution with shape parameters of $\alpha = 1.53$ and $\beta = 7.63$.

There are three main steps in the creation of the optimized spatial distribution of the grains on the wheel surface. The main steps include: i) identifying and calculating the spacing between neighboring grains, ii) sampling the beta distribution and translating the grains to their new locations, and iii) and transforming the polygons to their original three-dimensional geometry.

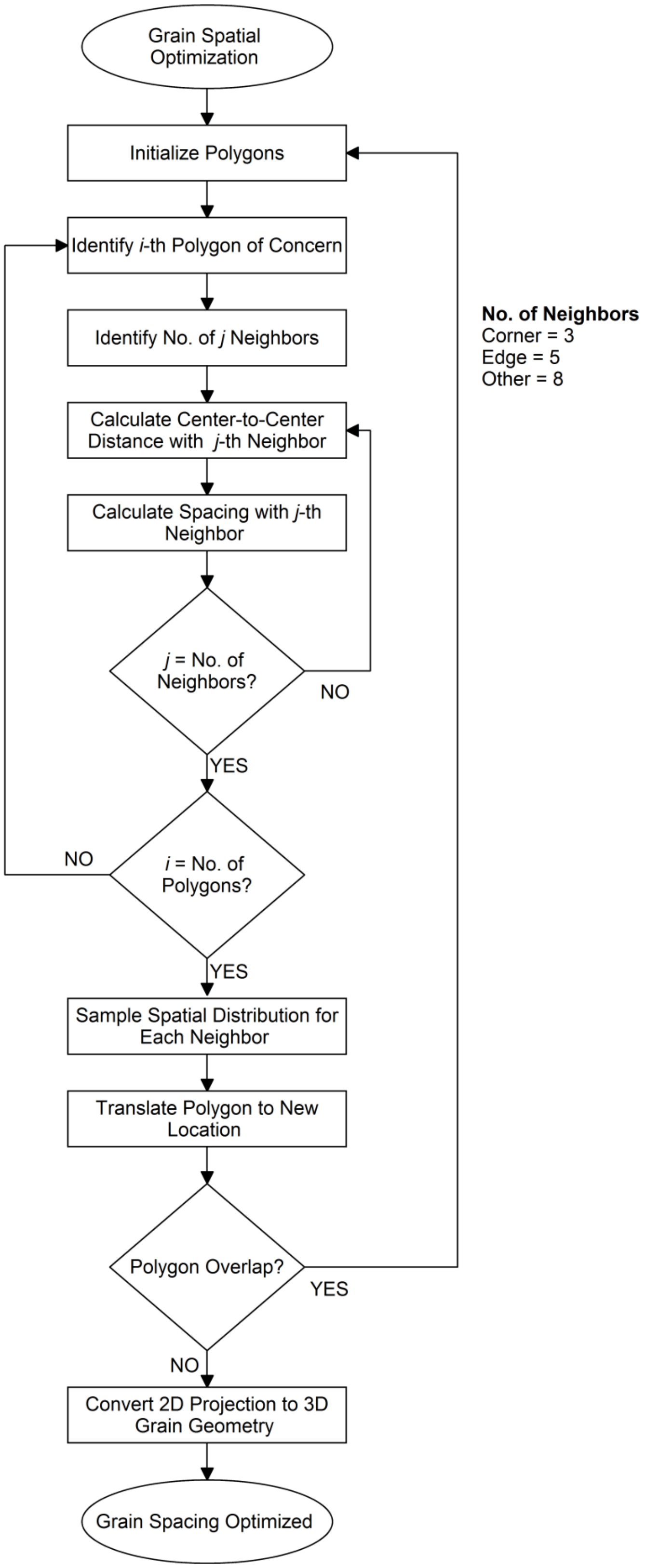

Figure 5.9 – Spatial optimization algorithm

5.5.1 Grain Spacing Calculation

It is first necessary to calculate the spacing between each polygonal model of a grain and its neighboring grains. This is accomplished by looking at the closest neighbors with edge identification. It is critical to be able to determine where the grain is located in reference to the simulated surface area of the initial lattice structure layout of grains to determine how many neighbors will be considered in the calculation. For instance, grains at a corner of the lattice only have to consider three neighbors while grains on an edge have to consider five neighbors. Grain neither on an edge nor at a corner must take all eight neighbors into consideration. This includes the cardinal and inter-cardinal (or ordinal) directions.

For each pair of grains, the center-to-center distance is calculated as the minimum Euclidean distance between the center grain and the j^{th} neighbor as shown in Figure 5.10a [111]. This procedure is then repeated until the i^{th} polygon equals the number of polygons created.

5.5.2 Optimized Spatial Separation

The next step is to apply the grain spatial separation per the statistical distribution found from the experiments and described in the Characterization Chapter. In this case, the beta distribution (shape parameters of $\alpha = 1.53$ and $\beta = 7.63$) with positive skewness, is used, indicating that the grains tend to be closer together and, at times, almost touch each other. The beta distribution is sampled n_I times, from Equation 5.4, and the distances are applied to the interaction distances between the grains. Then the polygons are translated to create the two-dimensional topography as given by the example shown in

Figure 5.10b. The polygons are then checked again for overlap using similar methods as before. If overlap is detected, the process repeats.

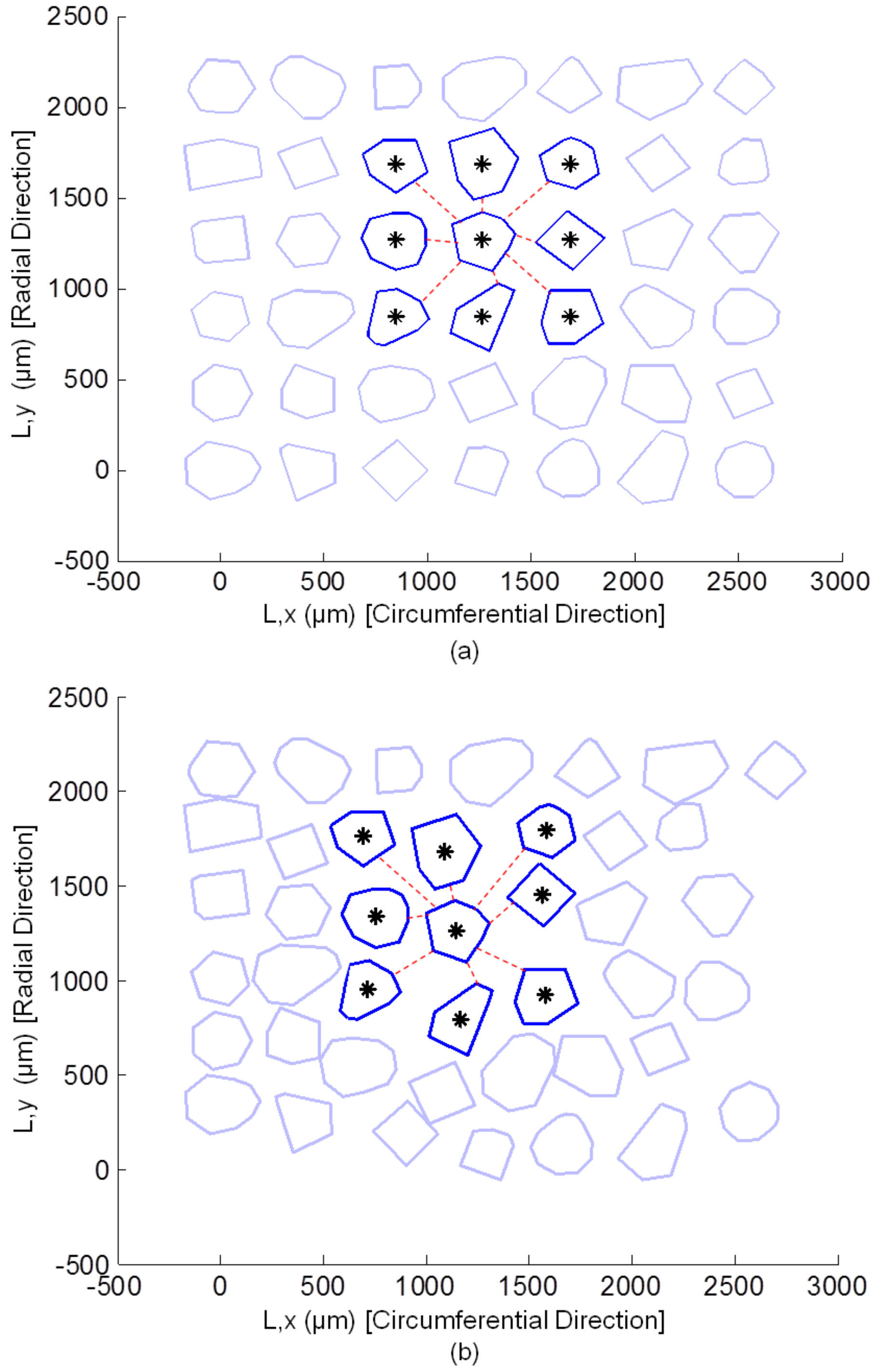

Figure 5.10 – Polygon optimization layout

5.5.3 Two-Dimensional to Three-Dimensional Transformation

The complete two-dimensional geometrical representation of the simulated grinding wheel is complete as illustrated in Figure 5.11a. At this point of the simulation the grains have been created and spaced as per the statistical distribution derived from the experiments. It is now time to restore the three dimensional representation to the model as shown in Figure 5.11b. The geometry is restored by applying the *z*-coordinates of the corner vertices from section 5.4.4. The next step to obtain a model of the grinding wheel surface topography is to apply bonding material to the transformed grains.

5.6 BOND MATERIAL FORMATION

The final part of creating a realistic model to accurately represent the grinding wheel topography is to model the bond material of the grinding wheel. Grinding wheels are made up of grains embedded in a bonding material. The main bonding materials are vitrified bond, rubber bond, metal bond, and shellac bond. This work concentrates on vitrified bonded grinding wheels

It is essential to take into consideration the bonding material since it has a distinct effect on the grinding process, especially where the dressing effect is concerned [60]. A function of the dressing process is to ensure that the bond material is preferentially removed from the wheel so that as the severity of the dressing increases, more bond material will be removed and grit pull will be more likely [112].

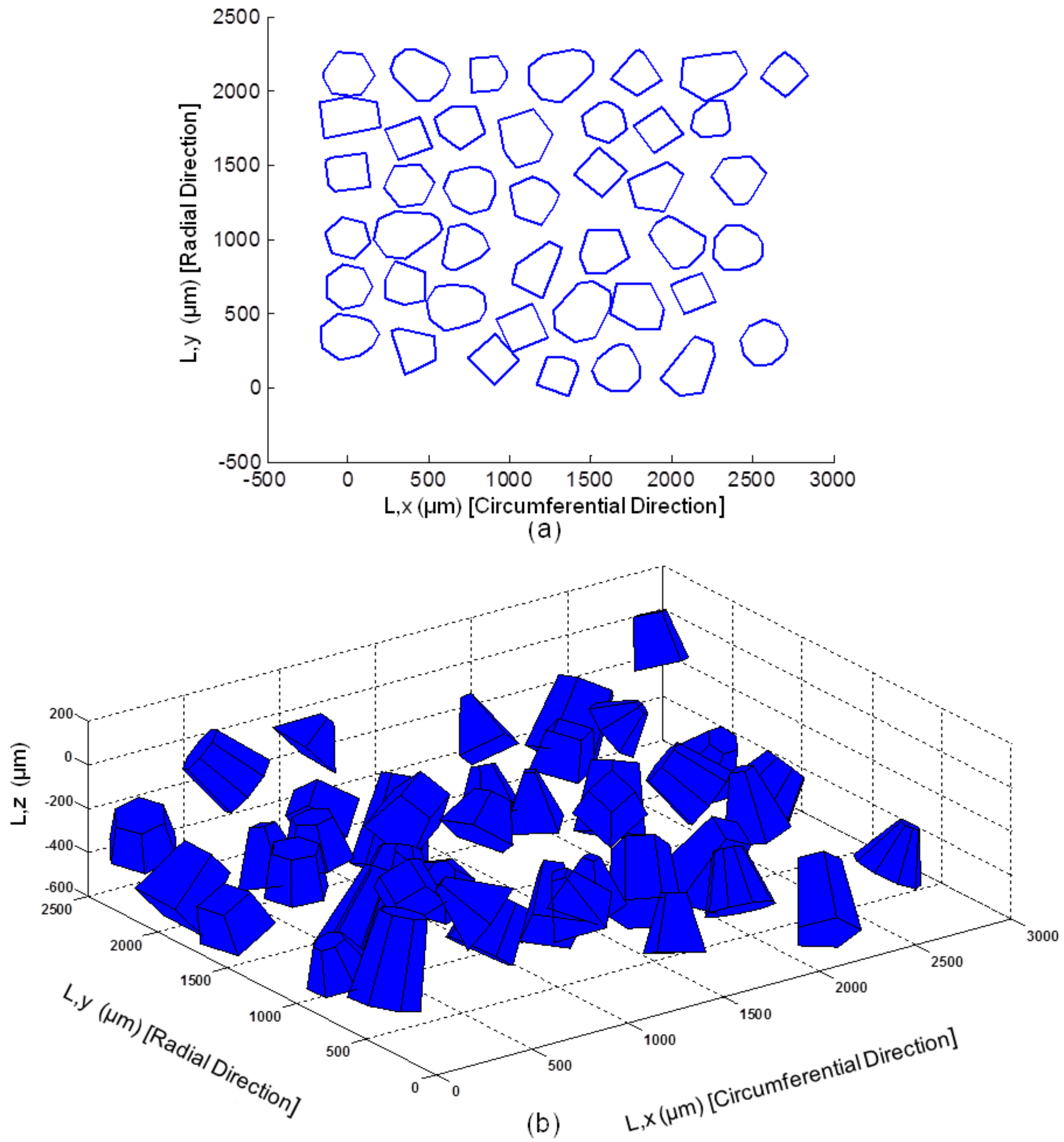

Figure 5.11 – Three-dimensional final grain layout

It is often difficult to tell the difference between the SG grains (white), aluminum oxide (translucent/blue) and bonding material (translucent/blue) as seen earlier in Figure 5.3a. It is also necessary to recognize that one is often looking through the first layer of grains and also seeing the second and third layers during experimentation.

For an electroplated CBN wheel, a grain protrusion height of 35% of the grain size is used for modeling the grinding wheel [113]. Even though multilayered, similar results were found for the SG wheel used in the experiments. Based on observations of the actual grinding wheel surface, a distinction between the bonding material and grains was made as shown in Figure 5.12. This was accomplished by averaging individual grain and bond height measurements from multiple scans using the Alicona instrument.

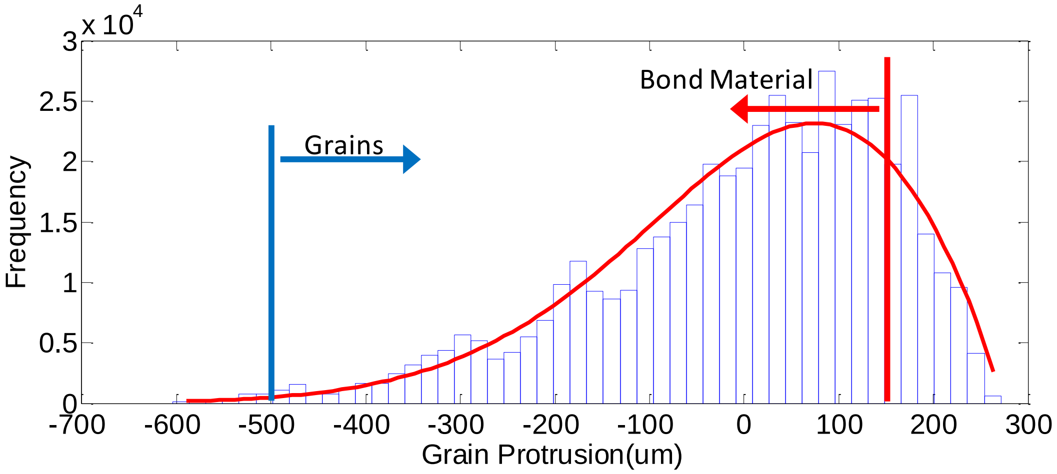

Figure 5.12 – Grain/bond transition

As shown in the figure, the grain negative cutoff was found to be around roughly 1.5 x average grain diameter (or -500µm). Bond material ranged from the grain cutoff to roughly half the grain size above the reference plane (grain protrusion = 0). Bond material is created by sampling the same beta distribution used for grain height but truncating bond material heights below the bond material cutoff indicated in Figure 5.12. The difference is that the bond material does not appear above the grains but only appears below the grain tip. The resulting grains and bond surface as represented in Figure 5.13.

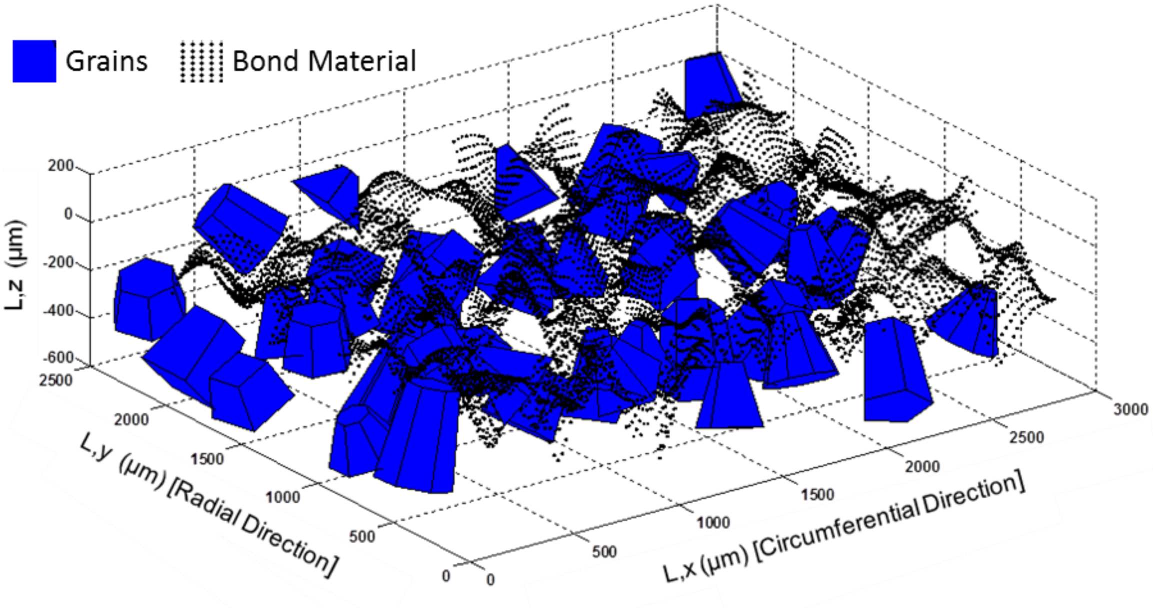

Figure 5.13 – Grain with bonding material point cloud

5.7 WHEEL TOPOGRAPHY FORMATION

The final step in creating the model for the surface topography of the grinding wheel consists of combining the abrasive grains modeled in earlier steps and the bond material. Figure 5.14 represents the transformation after the grain geometry and bonding material have been created. Figure 5.14a is a point cloud of the final wheel surface topography. This includes data points representing the simulated grains along with the bond material. Figure 5.14b shows the pseudo color topography plot to better represent the surface. Calculation of surface texture parameters of the wheel topography requires a reference plane to which measured heights are referred to. A MATLAB algorithm [114] was used to create a second-order least squares surface which was then fit to the height matrix, of the resulting combination of grains and bond material, to eliminate the form [115] and establish a reference plane (often referred to as the software datum) as illustrated by the hatched in Figure 5.14c.

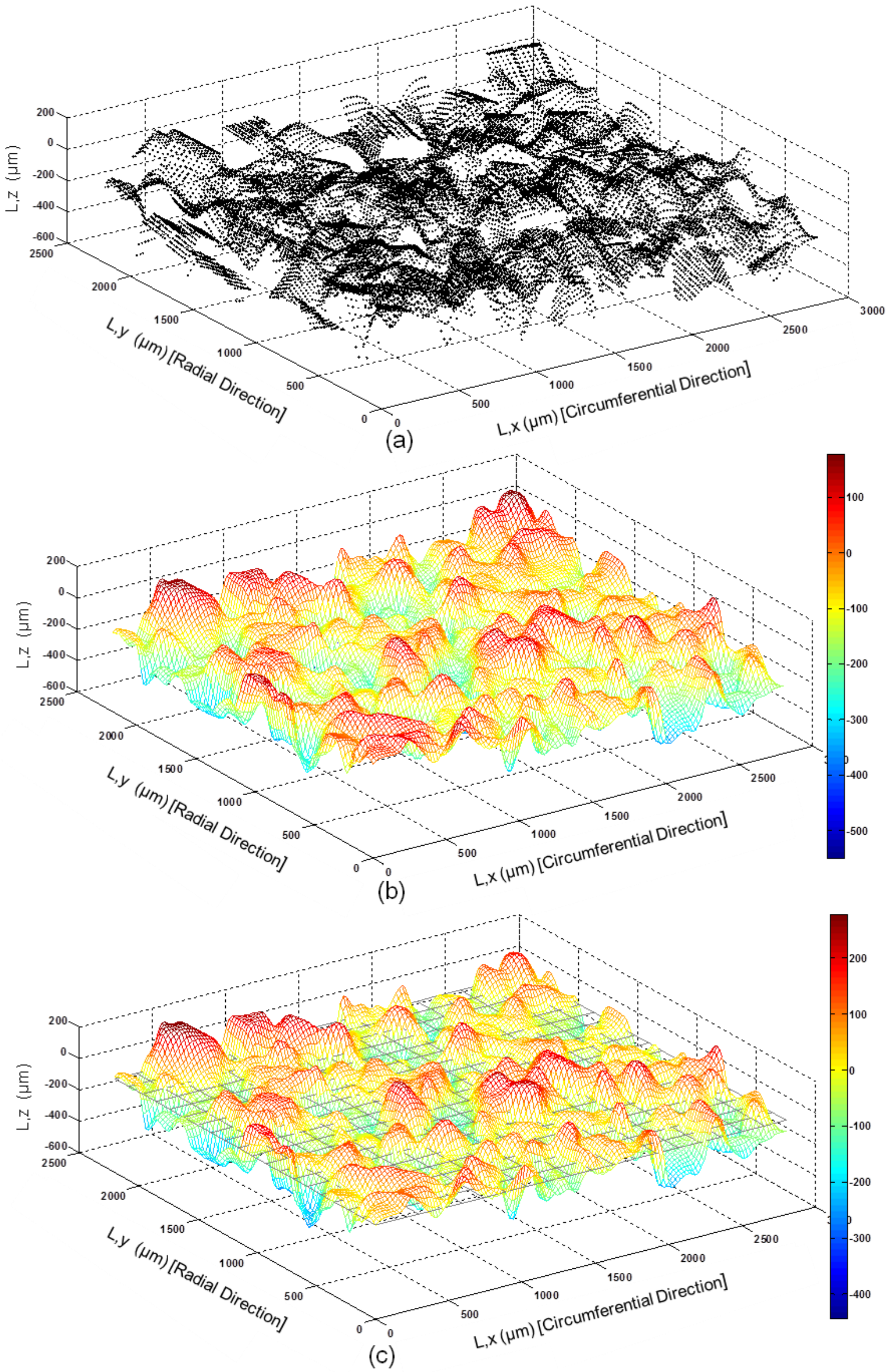

Figure 5.14 – Topography point cloud transformation. (a) point cloud of the simulated grinding wheel surface, (b) pseduo color topography plot, (c) resulting topography with form eliminated

5.8 SUMMARY

Grinding is an important precision material removal process and needs to be modeled correctly to be as accurate as possible. Many workpiece surface prediction models skip the wheel topography and go straight to the workpiece surface topography. This chapter introduced a stochastic model implemented in MATLAB to simulate a three-dimensional wheel surface topography under different dressing conditions. The grinding wheel is composed of a large number of abrasive grains randomly placed in the wheel and these are held together by a vitrified bond. Abrasive grains are difficult to model since they are geometrically undefined in shape on an actual grinding wheel but are modeled as polyhedrons in this work. This chapter described how the abrasive grains are placed in the grinding wheel using the statistical distributions found during wheel characterization experiments. It is now necessary to validate the developed model of wheel surface topography.

6. WHEEL TOPOGRAPHY MODEL VALIDATION

The previous chapter presented a model to simulate the three-dimensional surface topography of a precision grinding wheel. The main purpose of this chapter is to validate the model against the experimental findings of Chapter 3. The statistical inputs to the model consist of established distributions from the characterization and experimental chapters. Stochastic modeling was chosen since the grinding wheel surface topography consists of randomly distributed abrasive grains, bonding material, and porosity. The interaction between the wheel surface and the single point dressing tool is very complex. The transformation of the surface topography during dressing operations includes, but is not limited to, such factors such as grit fracture and/or grain pull-out. Fracture has the effect of altering the grain protrusion height distribution while grain pull-out decreases the grain density [8]. The stochastic approach results in a practical, useful model for production applications since parameters of the statistical distributions describing the various wheel properties adapt to such changes.

The output of the model created in the previous chapter is first converted into a three-dimensional point cloud describing the resulting simulated surface topography of the seeded-gel (SG) grinding wheel. This surface is then converted to a *.x3p* format and input to the Alicona software for comparison and validation to ensure that the output of the model is comparable to the measured wheel surface parameters. Conversion is accomplished by the *openGPS* software [116]. Essentially, it is Open Source Implementations for 3D – Surface Characterization Algorithms according to ISO 25178.

6.1 MODEL VALIDATION BACKGROUND

Simulations can be validated using both qualitative and quantitative methods to demonstrate similarities between the results of the model and experiments. Even though the simulation presented in this thesis is a stochastic model that uses statistical distributions acquired from sample populations of experimental data, it is important that results are realistic. The majority of existing grinding wheel simulations result in geometry that lacks realistic attributes of an actual grinding wheel surface topography. Specifically, early two-dimensional simulations resulted in plots like Figure 2.7 from the Chen and Rowe's model [7] and Figure 2.12 of Baseri *et al*.'s work [56]. Hegeman [4] three-dimensional modeled a diamond resin bonded grinding wheel but his resulting simulated surface, illustrated in Figure 2.14, lacks realism.

This thesis presented a model for simulating the three-dimensional surface topography of a seeded-gel (SG) grinding wheel illustrated in Figure 5.14 of the modeling chapter. Figure 6.1 and Figure 6.2 compares simulated and actual measured surfaces of the SG grinding wheel resulting from the same dressing conditions (50 µm infeed, 0.25 mm/rev lead; overlap ratio of 3). The typical simulated grinding wheel surface is shown in Figure 6.1a. Recall that this surface represents one random sample (out of thirty) from the model to determine the mean parameter measurements. Figure 6.1b is a representative surface scan obtained during experiments using a three-dimensional micro-coordinate measurement device. It can be seen that the simulated surface features appear very similar to the experimental surface maps and more realistic than past models presented in the literature review chapter including recent work by Darafon [51] in Figure 2.22.

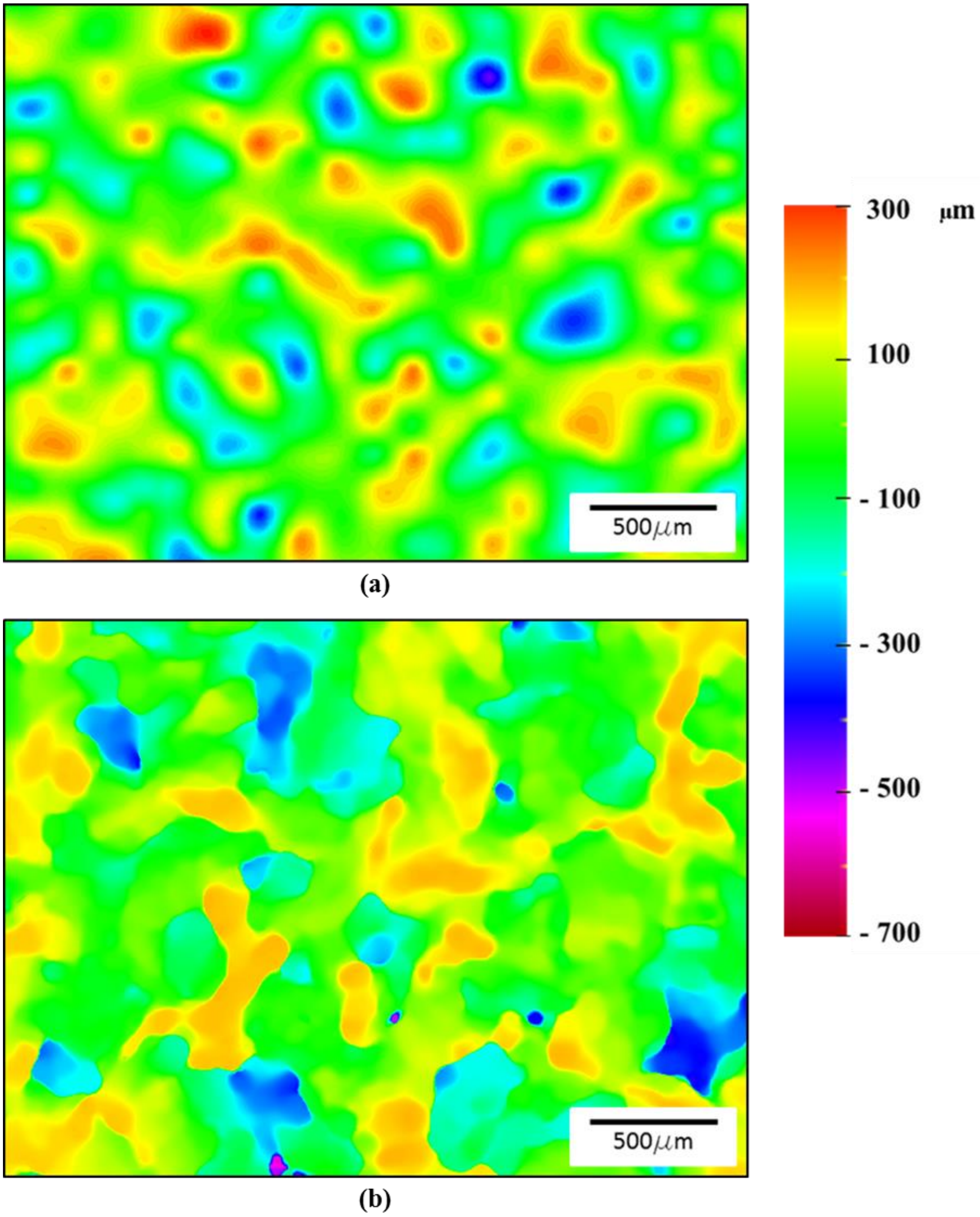

Figure 6.1 – Representative contour plots validating grinding wheel simulation model. Dressing parameters: 50 µm infeed, 0.25 mm/rev lead; overlap ratio of 3. a) simulated surface of grinding wheel b) experimental surface scan using 3D micro-coordinate measurement equipment

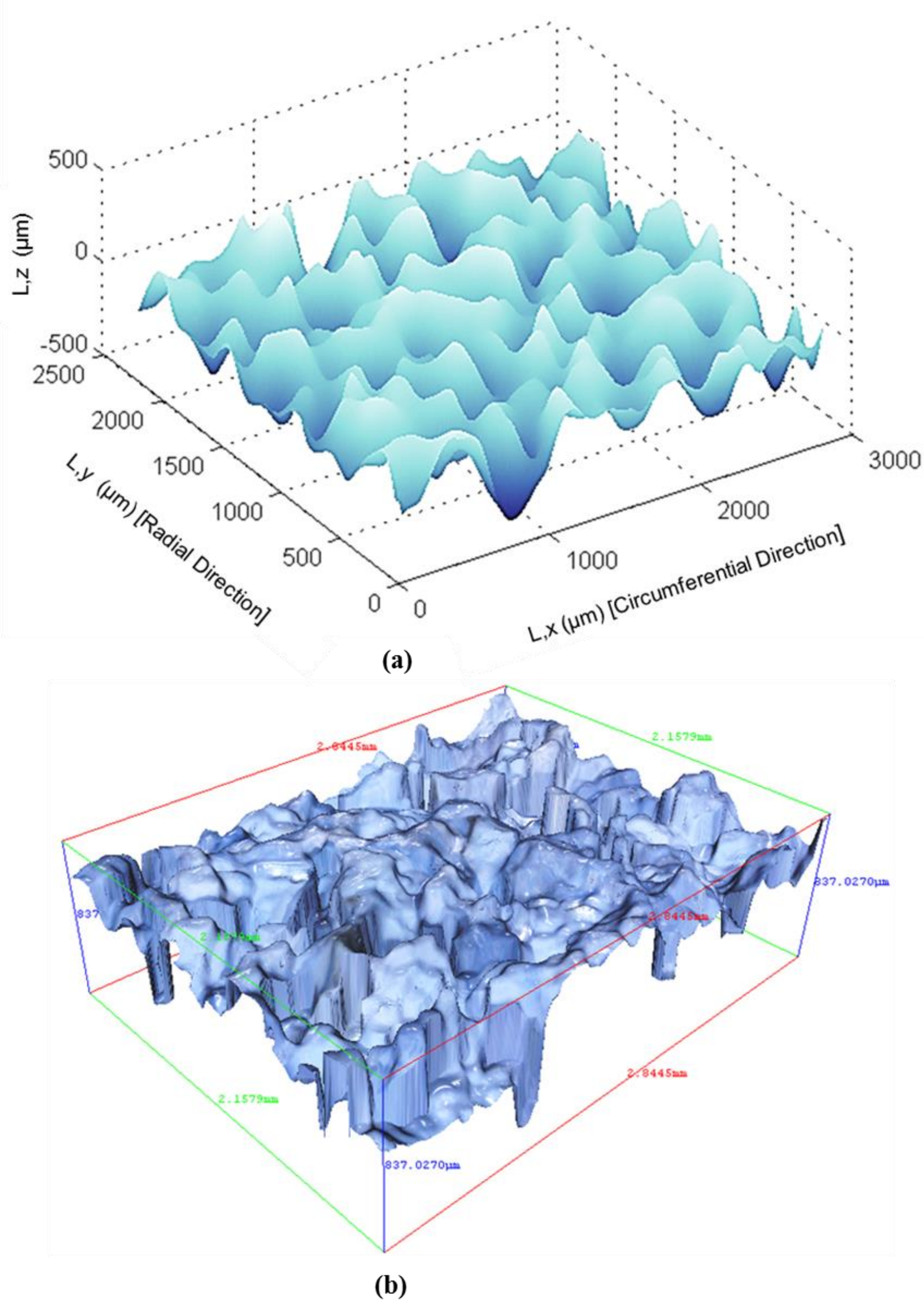

Figure 6.2 – Representative three-dimensional plots validating grinding wheel simulation model. Dressing parameters: 50 µm infeed, 0.25 mm/rev lead; overlap ratio of 3. a) simulated surface of grinding wheel b) experimental surface scan using 3D micro-coordinate measurement equipment

The quantitative validation process is accomplished by inputting the simulated surface topography into the same measurement Alicona software that was used to compute topography parameters presented in Chapter 3. Since the grinding wheel surface topography model created in Chapter 5 is stochastic, the simulations of the wheel surface for each dressing condition were repeated thirty times, similar to the actual experimental trials, and the values averaged and a standard deviation calculated for comparison. Note that all measurement parameters are not relevant to grinding wheel surfaces and therefore only some were chosen. The parameter set chosen consists of S-parameters and V-parameters. The S-parameters describe both amplitude and spatial information. The V-parameters give fundamental volumetric information based on the areal material ratio curve (Abbott–Firestone curve). The main parameter groups chosen for validation were i) amplitude, ii) bearing area, and iii) volume parameters.

For model validation, the simulated height parameters are compared to the experimental values reported in Chapter 4. It was decided to separate the effects of the dressing infeed and lead parameters along with the initial wheel condition. Recall that the infeed is the distance the single point diamond dresser is fed into the grinding wheel surface while the lead is related to the traverse rate of the dressing diamond across the surface of the grinding wheel. The *initial condition* of the wheel refers to the conditioning of the grinding wheel at very low infeed and lead to represent a worn, or dull, grinding wheel. This was accomplished by making several passes of the single point diamond dresser at a low lead (0.0229 mm/rev) and a gradually reducing infeed (ranging from 25.4 to 6.35 µm) [29]. The infeed comparison is intended to monitor the effects of changing the infeed (13, 25, and 50 µm) while maintaining the maximum lead (0.25 mm/rev). The lead values used for comparison are 0.05, 0.15, and 0.25 mm/rev while maintaining the maximum infeed of 50 µm.

Separating the dressing parameters by looking at the effects of lead and infeed enables the ability to recognize which parameter affects the dressing process more and which one the model is able to simulate better. Refer to Appendix B for a table of the magnitudes, standard deviations, and percent differences presented in the following sections for each dressing condition.

6.2 VALIDATION OF AMPLITUDE PARAMETERS

The first part of the validation involves comparing the three-dimensional height parameters of the simulated surface topography to the actual surfaces found in the experimental trials. The change in the height distribution is partially due to grit rising from grit fracture and/or dislodgement of the abrasive grains during dressing.

The height parameters in three-dimensions differ from the traditional two-dimensional parameters. In two-dimensions, a peak is the highest value between its two nearest neighbors, which is only along the line of the profile, but in 3D, a peak can be defined by various criteria (four nearest neighbors, eight nearest neighbors, autocorrelation, and so on). In this thesis, a peak is defined as any point that is above all eight nearest neighbors. Peaks are constrained to be separated by at least 1% of the minimum X and Y dimension comprising the 3D measurement area [46]. Standard roughness parameters *Sa* and *Sq*, which are normally used in practice for identifying and classifying contact surfaces, are not sufficient to determine the tribological properties [117]. This is why other parameters are chosen as well. The amplitude (height) parameters chosen for model validation include the root-mean-square height *Sq*, maximum peak height *Sp*, skewness *Ssk,* and kurtosis *Sku* of the selected area summarized in Table 6.1 These parameters were chosen to represent the surface topography of the grinding wheel.

Table 6.1 – Amplitude parameters utilized for model validation

Parameter	Units	Definition
Sq	µm	RMS height of selected area
Sp	µm	Maximum peak height of selected area
Ssk		Skewness of selected area
Sku		Kurtosis of selected area

6.2.1 RMS Height of Selected Area, *Sq*

The root-mean-square (RMS) *Sq* value of the ordinate values within a definition area is mathematically defined as

$$S_q = \sqrt{\frac{1}{A} \iint_A \; z^2(x,y)\, dxdy} \tag{6.1}$$

where *A* is the sampling area. Note that the above is for a continuous *z(x,y)* function. Making surface texture measurements using any surface texture measuring instrument, *z(x,y)* will be determined over a discrete number of measurement points and is therefore written as [118]

$$S_q = \sqrt{\frac{1}{N}\frac{1}{M}\sum_{i=1}^{N}\sum_{j=1}^{M} z_{ij}^2} \tag{6.2}$$

where *N* and *M* are points in the *x* and *y* direction, respectively. *Sq* is chosen since it is generally much more statistically significant parameter, compared to *Sa* [118]. Generally

Sq is used to describe the coarseness of the surface and *Sa* does not provide any more information than *S*q [119].

The comparisons between the simulated and experimental results are illustrated in Figure 6.3. Even though slightly low in magnitude, the simulated results follow the experimental trends well for the majority of dressing scenarios. However, the effect of 0.05 mm/rev lead value does not seem to experience the same change in magnitude when comparing the experimental findings to the simulated *Sq*.

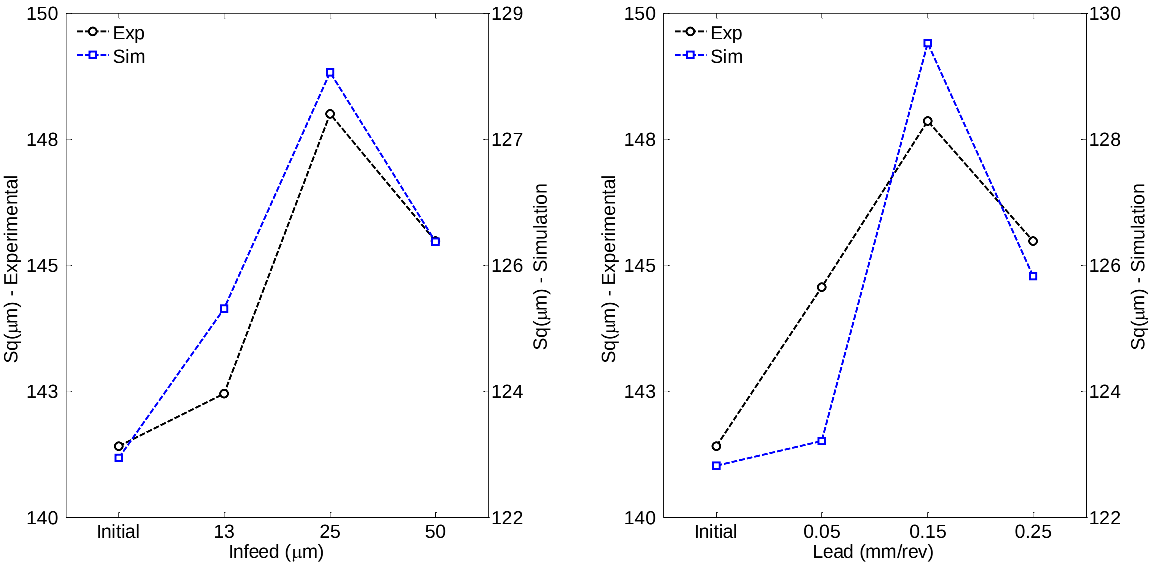

Figure 6.3 – Validation of root-mean square height *Sq*. a) (left) comparison of infeed for lead of 0.25 mm/rev, b) (right) comparison of lead for infeed of 50 μm

The effects of both infeed and lead seem to increase *Sq* until the most aggressive dressing condition when the RMS roughness appears to decrease. This may be the result of different combinations of factors but is thought to be the result of grain dislodgement. This occurs when the force applied by the dressing diamond exceeds the retention force of the bonding material holding the abrasive grain to the grinding wheel.

6.2.2 Maximum Peak Height of Selected Area, *Sp*

The second height parameter of the simulated wheel surface topography is the peak height of the selected area *Sp* and is expressed mathematically as [34]

$$S_p = MAX\ (\eta_p) \tag{6.3}$$

where η_p is the highest surface summit of the topography, which relies on the eight nearest neighbor definition. The maximum peak height *Sp* of the scale limited surface is the largest height value within a defined area from the calculated mean plane [120]. Results of the comparison are shown in Figure 6.4.

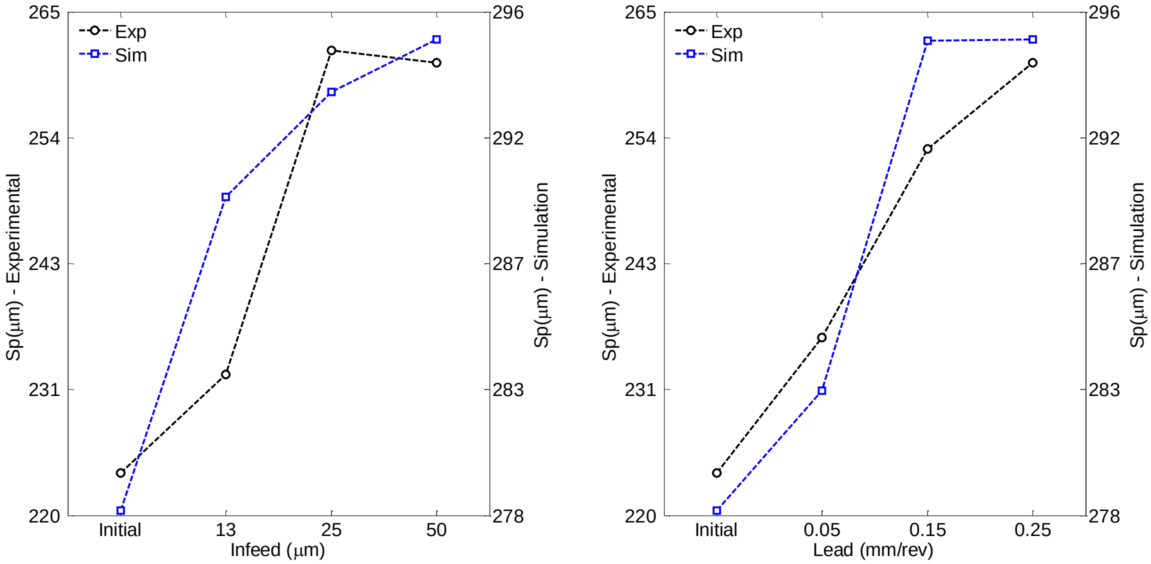

Figure 6.4 – Validation of peak height *Sp*. a) (left) comparison of infeed for lead of 0.25 mm/rev, b) (right) comparison of lead for infeed of 50 µm

There is no defining equation of this height parameter since it is simply the peak or a point whose departure from the reference or datum plane (on the positive side) is the highest. The comparisons of simulated results versus experimental measurements follow similar trends. The magnitude of *Sp* increases for both infeed and lead until the highest change in magnitude. In regards to the infeed, the experimental values actually decrease when the infeed is changed from 25 to 50 µm while the simulated values increase in an almost linear fashion from 13 to 50 µm. The comparison of the lead dressing parameter exhibits opposite trends. Experimental values increase linearly but the simulated results plateau at the higher lead from 0.15 to 0.25 mm/rev. It appears that that the lead has more of an effect on the protrusion peak height compared to the effect of infeed creating a slightly coarser surface while the model predicts the opposite even though the difference is small.

6.2.3 Skewness of Selected Area, *Ssk*

The third height parameter for validation is the skewness of the amplitude distribution. Skewness S_{sk} of the scale-limited surface is the quotient of the mean cube value of the ordinate values and the cube of the S_q within a definition area [120] given by

$$S_{sk} = \frac{1}{S_q^3}\left[\frac{1}{A}\iint_A z^3(x,y)\,dxdy\right] \tag{6.4}$$

where A is the sampling area. This parameter describes the shape of the surface height distribution and is a the measure of the profile symmetry about the mean plane [118] as shown in Figure 6.5 illustrating the shape dictated by the skewness value of the frequency of the surface topography height. The polarity of the amplitude is maintained since the sampling area is cubed. Typically, a surface with a Gaussian (normal) distribution that is symmetric has a skewness of zero (black solid line) while a positive skewness is indicated by the dashed red line and negative skewness is represented by the dotted blue line.

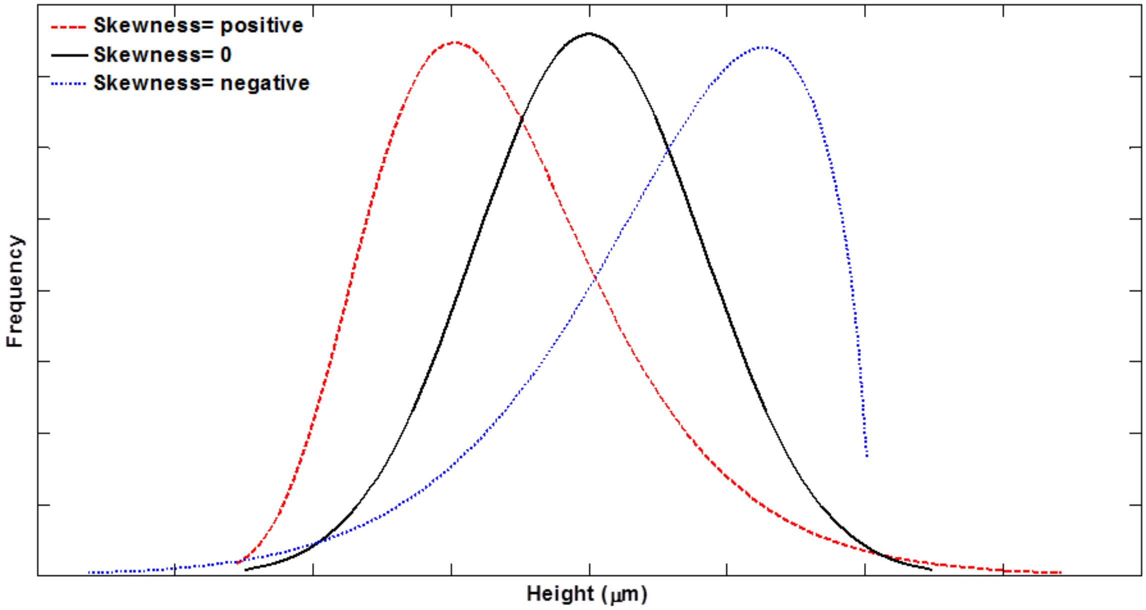

Figure 6.5 – Visualization of skewness

The skewness height parameter provides information regarding the dominance of either peaks (*Ssk*>0) or valleys (*Ssk*<0). The direction of the skew is dependent on whether the bulk of the material is above the mean plane (*Ssk*<0) or below the mean plane (*Ssk*>0). Overall, the simulated surface topography overall properly portrays the actual surface of the grinding wheel by having negative skewness indicating that the topography consists of the bulk of the material being above the mean plane with predominantly valley-type features in Figure 6.6.

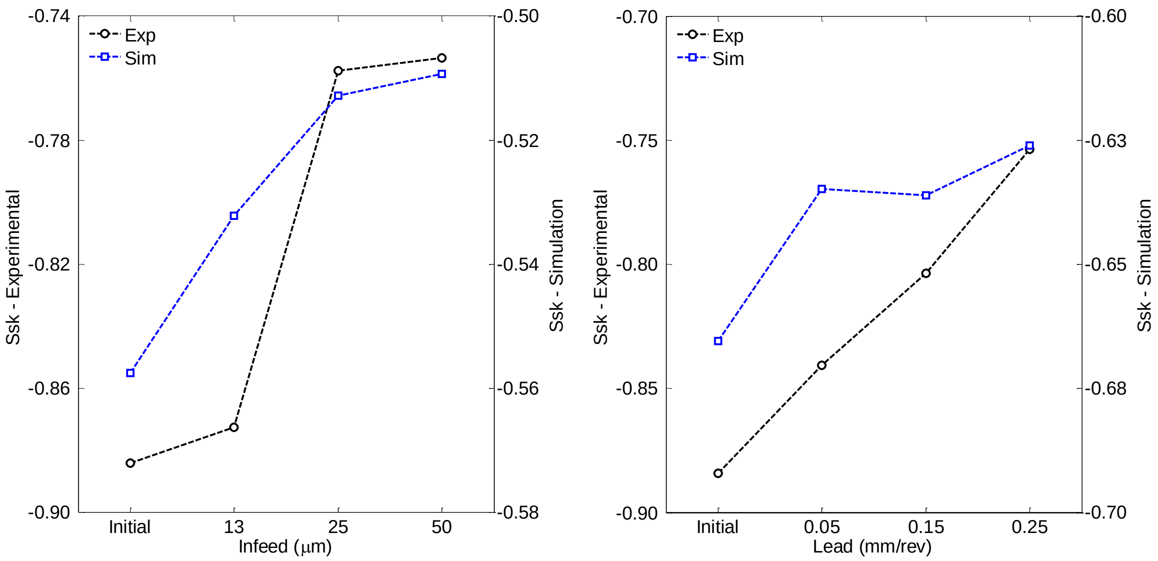

Figure 6.6 – Validation of skewness *Ssk*. a) (left) comparison of infeed for lead of 0.25 mm/rev, b) (right) comparison of lead for infeed of 50 μm

The simulation of the skewness continues to follow the basic experimental trends but not as closely as the other height parameters. This is most likely do the fact that skewness needs a larger sample size. Recall, that there were only thirty simulations sampled and 34 experimental runs for each dressing condition. It is assumed that the two cases of validation would further converge if both were repeated a greater number of times. Currently the simulated results of the infeed seem to exhibit more of a linear relationship ranging from the initialized wheel to the 50 μm infeed. The experimental findings show more of a stepped condition. The difference between initial and 13 μm infeed are similar and then there is a large change from 13 to 25 μm infeed. Then again, there is minimal change from 25 to 50 μm infeed. The effect of lead shows opposite trends. The experimental findings exhibit a linear relationship while there is minimal change between 0.05 and 0.15 mm/rev. The lead of 0.04 mm/rev seems to be simulating too many peaks.

6.2.4 Kurtosis of Selected Area, *Sku*

The final height parameter used to validate the simulation is the kurtosis of the amplitude distribution. Kurtosis *Sku* of the scale-limited surface is the quotient of the mean quartic value of the ordinate value and the fourth power of *Sq* within a definition area and is given by [120]

$$S_{ku} = \frac{1}{S_q^4}\left[\frac{1}{A}\iint_A \ z^4(x,y)\ dxdy\right] \tag{6.5}$$

where A is the sampling area. This parameter is used to describe the sharpness of the topography height distribution and is visualized in Figure 6.1. In general, the sharpness of a centrally distributed height distribution has a kurtosis value of three or more, visualized as the red dashed line, and less than three when the distribution is well spread out similar to the black solid line and blue dotted line in the figure. The latter has a kurtosis of less than three which indicates that their height departures are well spread out. Rolling hill type textures generally have values less than three and result when surfaces have a less peaked nature [119], [121]. When the kurtosis value is above three, it usually indicates high peaks or deep valleys. By definition, the kurtosis value is not able to distinguish between peaks and valleys since the equation is to the fourth power. With the combination of the skewness and kurtosis it may be possible to identify deep valleys and flat tops in surfaces [119].

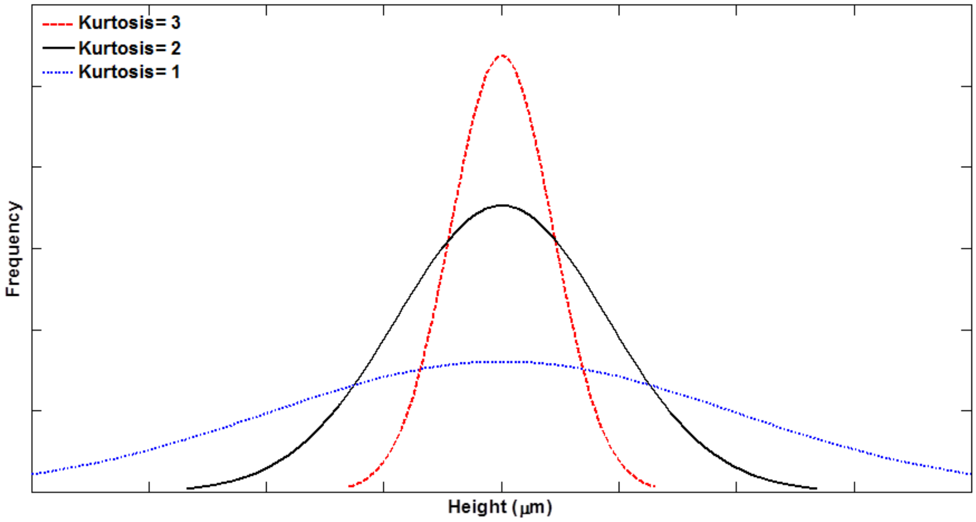

Figure 6.7 – Visualization of kurtosis

The comparison between the simulation and experimental findings are illustrated in Figure 6.8. The kurtosis values follow the same trends when comparing the actual grinding wheel topography found during the experimental trials and the simulated surface by both having values above three, which indicates less deviation of the height distribution in both cases.

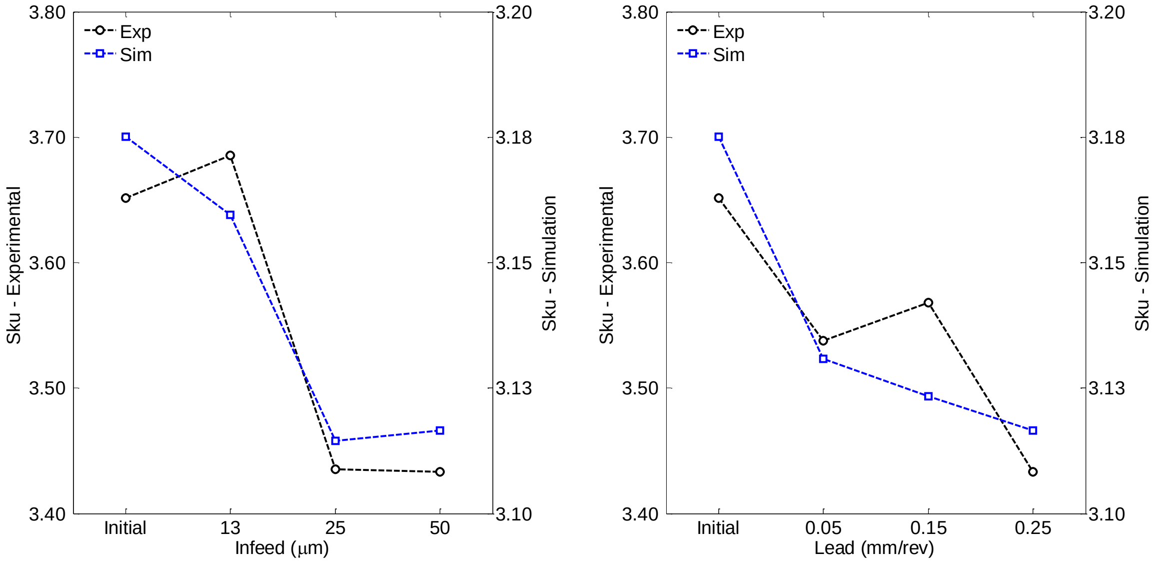

Figure 6.8 – Validation of kurtosis *Sku*. a) (left) comparison of infeed for lead of 0.25 mm/rev, b) (right) comparison of lead for infeed of 50 μm

Kurtosis decreases with both the increase of infeed and lead. This is expected since the contact between the diamond dressing tool exposes fresh abrasive grains. Therefore, more freshly sharpened grain summits are indicated by the slightly lower value of kurtosis when increasing both infeed and lead for the majority of cases.

6.3 VALIDATION OF BEARING AREA PARAMETERS

The next parameter group under investigation is the bearing area parameters visually defined in Figure 6.9. They are considered a subsection of *V-Parameters* by ISO. Figure 6.9a shows the parameters in relation to the Abbott-Firestone Curve and Figure 6.9b illustrates how the parameters are correlated to the traditional two-dimensional profile trace of the surface texture. The purpose of the Abbott-Firestone curve is to assess the functional topographical features of the surface by analyzing the material volume and void volume of the surface. The volume parameters are covered in the next section. The idea is to split the material ratio curve of a surface into three height zones: the peak, the core, and the valley zones. The parameters most related to the surface of the grinding wheel topography are: i) the distances between the highest and lowest level of the core surface, *Sk*, and ii) average heights of the protruding peaks above the core surface, *Spk*, with *Smr1* being a function of the two and therefore not compared. The other parameters *Svk* and *Smr2* are not evaluated since they are the valley structures and do not take part during the interaction of the diamond dressing tool and grinding wheel or in future studies simulating interaction of the grinding wheel with the workpiece. It is also difficult to get accurate measurements of these structures with the Alicona measurement equipment during the experiments since *Svk* would include layers beyond the first layer of grains. The volume parameters are equivalent to the cumulative probability of the profile heights and are directly related to the surface tribological behavior, and particularly, with the real contact area, asperities strength, and wear [108].

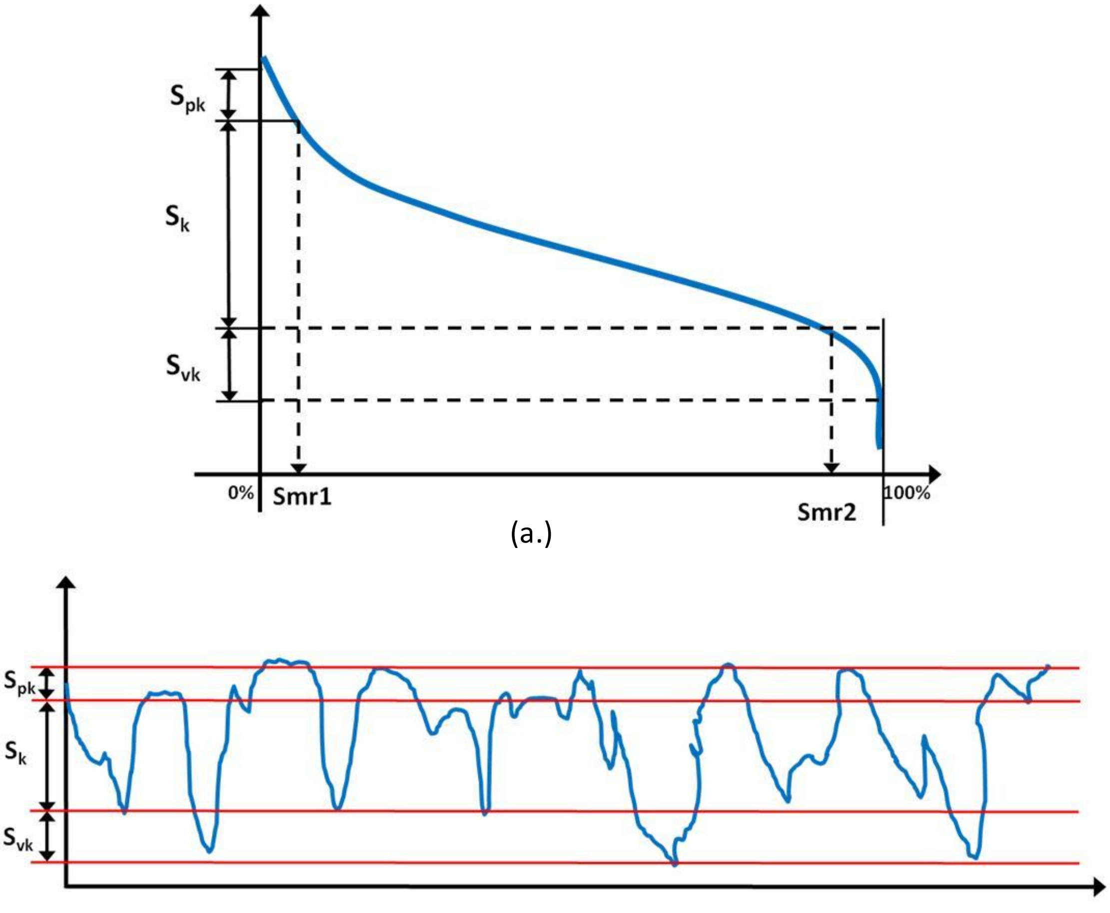

(a.)

(b.)

Figure 6.9 – Bearing area curve diagram [122]

6.3.1 Reduced Peak Height, *Spk*

The first parameter of concern when comparing the bearing area curve is the reduced peak height, *Spk*. The reduced peak height serves as a measurement of the peak height above the core roughness of the surface, or in layman’s terms, the small peaks above the main structure of the surface. In general, a high value implies the surface is composed of high peaks providing small initial contact area and high areas of stress when the surface is contacted. These peaks are generally the first part of the topography of the grinding wheel to be worn off during the interaction of the diamond during dressing or during workpiece interaction. The comparison of the experimental trials and simulated surfaces is illustrated in Figure 6.10.

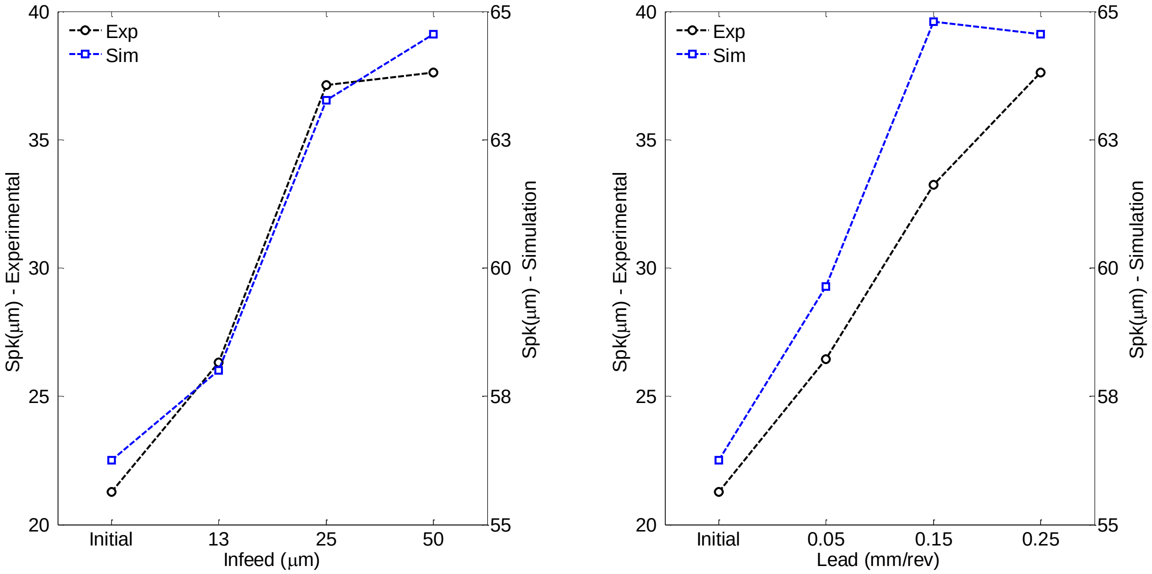

Figure 6.10 – Validation of reduced peak height *Spk*. a) (left) comparison of infeed for lead of 0.25 mm/rev, b) (right) comparison of lead for infeed of 50 µm

The simulated values follow the same general trends as were found during the experiments. The *Spk* value is such a small section of the bearing curve as indicated in Figure 6.9a and difficult to capture and, not surprisingly, the magnitudes have some deviation. It would be beneficial, but not mandatory, to have closer magnitudes since these high spots are assumed to be worn down quickly in actual grinding experiments.

6.3.2 Core Roughness Depth, *Sk*

The main portion of the Abbott-Firestone curve is *Sk*. The core of the material is described by the core roughness depth *Sk*, which is the peak-to-valley height with the main peaks and valleys removed. This parameter correlates to the depth of the working section of the grinding wheel taking part in the interaction with the diamond during dressing or workpiece surface after the break in-period. The parameter is determined by fitting a linear curve to the central 40% of the measurement points [123] and is considered the "core roughness" or "kernel" [34]. The comparison of the simulated results and experimental findings is shown in Figure 6.11.

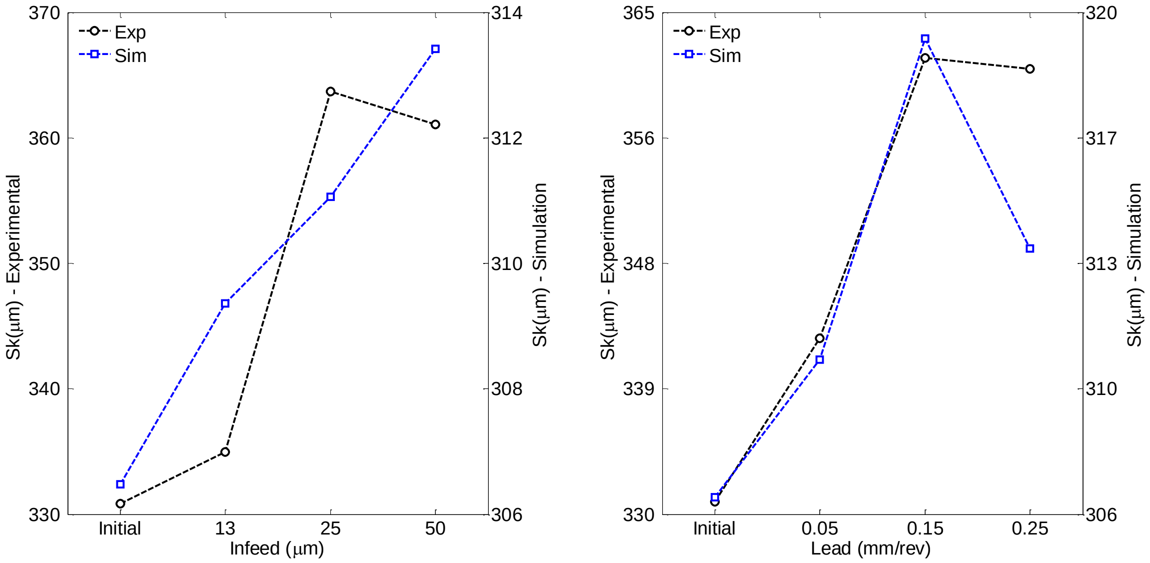

Figure 6.11 – Validation of core roughness depth *Sk*. a) (left) comparison of infeed for lead of 0.25 mm/rev, b) (right) comparison of lead for infeed of 50 μm

Not surprisingly, the simulated magnitudes of *Sk* match closer than *Spk* since the Abbott-Firestone curve consists of the bulk of peaks and valleys. The overall trends tend to match except for the lead value of 0.25 mm/rev. The simulation model appears to not capture the effects of aggressive dressing parameters and exaggerates the decrease for the high lead condition.

6.4 VALIDATION OF VOLUME PARAMETERS

The next set of parameters for comparison to validate the simulation model of the surface topography is the volume parameters derived from the volume information of the bearing area curve assuming that the peak material embraces 0~10% of the bearing area while the core and valley ranges cover 10~80% and 80~100% of the bearing area respectively [34]. They are summarized in Table 6.2.

Table 6.2 – Volume parameters

Parameter	Units	Definition
V_{mp}	ml/m^2	Peak material volume of the topographic surface
V_{mc}	ml/m^2	Core material volume of the topographic surface
V_{vc}	ml/m^2	Core void volume of the surface

The three main volume parameters under evaluation in this report include: i) peak material volume of the surface *Vmp*, ii) core material volume of surface *Vmc*, and iii) core void volume of the surface *Vvc*. The volume parameters are derived from the bearing analysis of the three-dimensional surface topography of the grinding wheel. The bearing area curve is created by calculating the amount of material a plane would rest on relative to the complete cross section of the surface for each height from the highest to the lowest point of the surface [46].

6.4.1 Peak Material Volume of the Topographic Surface, *Vmp*

The peak material volume *Vmp* parameter in the material is mathematically given by [34]

$$V_{mp} = \frac{V_m(h_{0.10})}{(M-1)(N-1)\Delta x \Delta y} \tag{6.6}$$

where *Vm* is the material volume parameters and *N* and *M* are points in the *x* and *y* direction. This is the enclosed material portion of the $h_{0.10}$ bearing area and normalized to unity. In general, the *Vmp* parameter can be used for the same purpose as the *Spk* parameter, i.e. to characterize the volume of material, which is likely to be removed during running-in of the grinding wheel [124]. The comparison between the experimental findings and simulations of peak material volume of the grinding wheel surface topography is examined in Figure 6.12.

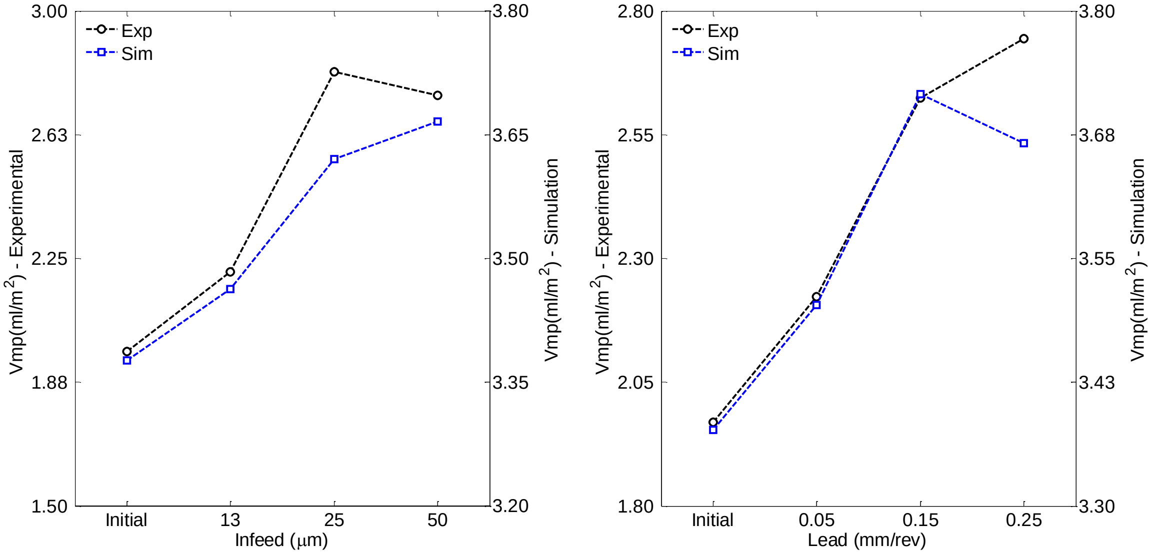

Figure 6.12 – Validation of peak material volume of the topographic surface *Vmp*. a) (left) comparison of infeed for lead of 0.25 mm/rev, b) (right) comparison of lead for infeed of 50 μm

The effects of infeed and lead on the peak material volume of the topographical surface follow similar trends when comparing simulation results to experimental findings for the majority of dressing conditions. However, the simulated aggressive lead of 0.25 mm/rev appears to decrease while the value increased during the experiments. Even though the trends are similar, the magnitudes are not considered acceptable when comparing the percentage difference. This is similar to the *Spk* situation, since related to

Vmp, both are very small measurements representing the small peaks that are worn during break-in of the grinding wheel.

6.4.2 Core Material Volume of the Topographic Surface, *Vmc*

The core material volume *Vmc* is the difference between the two material volumes calculated at different heights enclosed from 10% to 80% of the surface bearing area, normalized to the unit sampling area, and mathematically represented as [34]

$$V_{mc} = \frac{V_m(h_{0.08}) - V_m(h_{0.10})}{(M-1)(N-1)\Delta x \Delta y} \tag{6.7}$$

where *Vm* is the material volume parameters and *N* and *M* are points in the *x* and *y* direction. The comparison, in Figure 6.13, of infeed and lead dressing conditions for both experimental and simulated results exhibit similar trends and vary in percent difference of less than 20 percent. The effects of lead simulate well ranging from the initial wheel condition and following similar trends to aggressive 50 µm depth of cut. The lead simulation follows similar results as the infeed results. The simulated effect of 0.05 mm/rev lead does not seem to replicate the same amount of increase of core material volume seen in the experimental results but still predicts an increase. This indicates that the simulated core material volume is affected more by infeed than lead at lower values compared to the experimental results.

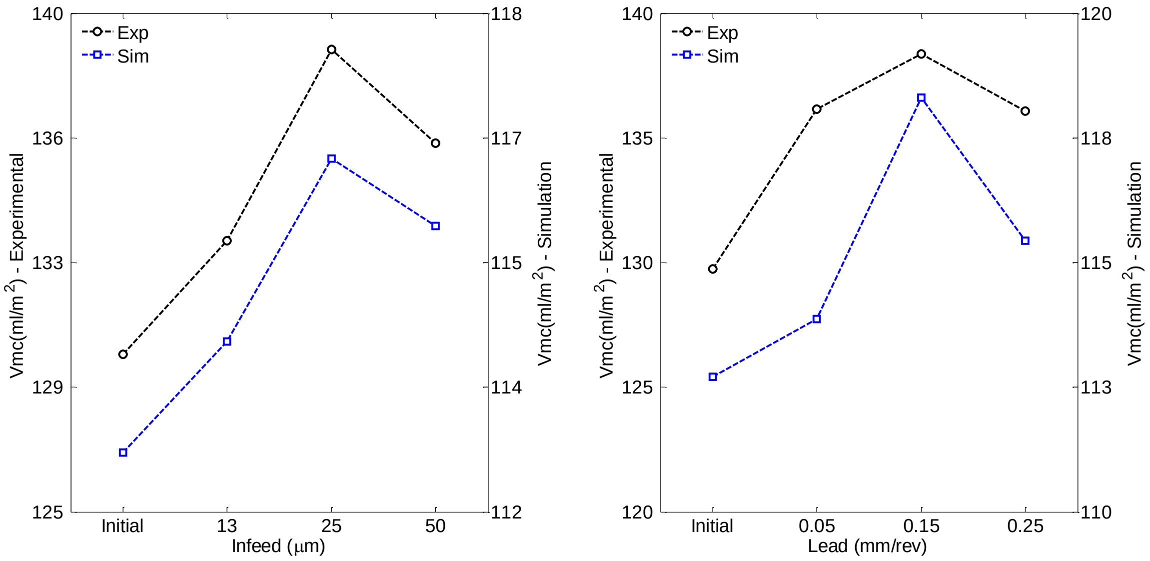

Figure 6.13 – Core material volume of the topographic surface *Vmc*. a) (left) comparison of infeed for lead of 0.25 mm/rev, b) (right) comparison of lead for infeed of 50 µm

6.4.3 Core Void Volume of the Surface, *Vvc*

The void volume of the surface *Vvc* is the difference in void between the material ratio's and mathematically expressed as [34]

$$V_{vc} = \frac{V_v(h_{0.10}) - V_v(h_{0.08})}{(M-1)(N-1)\Delta x \Delta y} \tag{6.8}$$

where void volume *Vvc* is expressed as [34]

$$V_v(h) = V_v(h_{max}) - (M-1)(N-1)\Delta x \Delta y (h_{max} - h) + V_m(h) \tag{6.9}$$

where *N* and *M* are points in the *x* and *y* direction. On a mechanical component, after several hours of function, the highest peaks are cut out or plastically deformed, and the corresponding particles of material are captured by the deepest valleys, so that the behavior of the surface is more likely described by *Vmc* and *Vvc*. [124].

Figure 6.14 compares the similarities between the simulated results and experimental findings for measurements of the core void volume of the surface of the grinding wheel as the function of different dressing conditions. The simulated surface topography of the grinding wheel appears to follow similar trends of the actual grinding wheel for different effects of both infeed and lead. The percentage difference also closely matches with the maximum of 14% difference throughout the dressing conditions. The simulated surface exhibits more of a linear relationship between initialization of the grinding wheel up to the central dressing parameter for both effects of infeed and lead. More aggressive conditions do not seem to have much of an effect when increasing from 25 to 50 µm infeed along with the effect of 0.15 to 0.25 mm/rev during the experimental trials. The simulation captures the same effect in the case of infeed but over estimates the decrease of core volume when increasing lead.

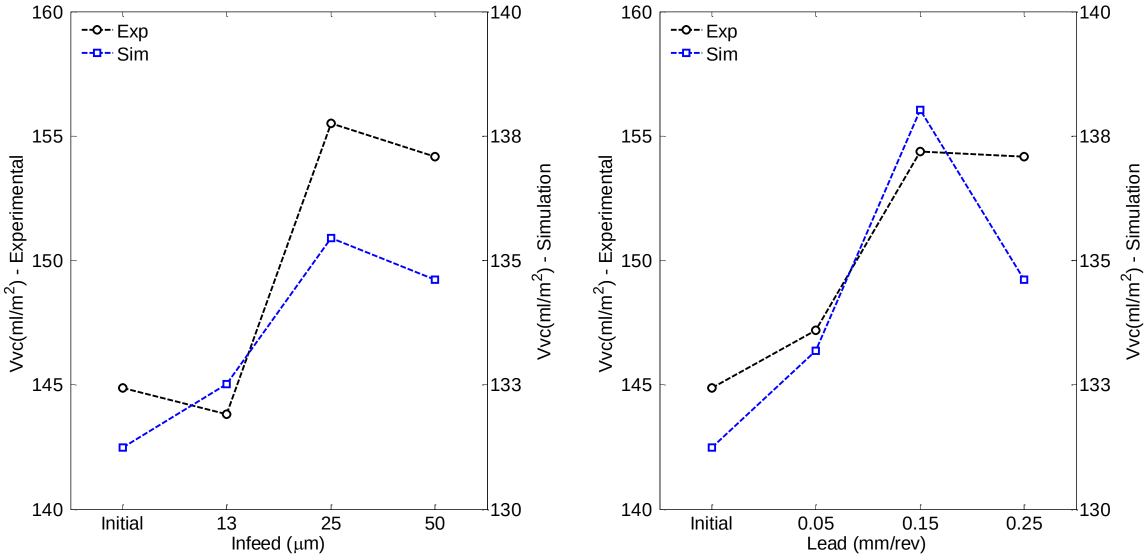

Figure 6.14 – Core void volume of the surface *Vvc*. a) (left) comparison of infeed for lead of 0.25 mm/rev, b) (right) comparison of lead for infeed of 50 µm

6.5 SUMMARY

The previous chapter introduced a stochastic model for simulating the surface topography of grinding wheels for different dressing conditions using statistical knowledge gained in the experimental section of this work. Examples of the key characterization attributes used to model the surface were based on the statistical distributions of geometry, height of grains, and spatial separation. The simulation is validated by comparing the simulated surface to the actual grinding wheel topography via three-dimensional areal surface parameters relevant to the grinding wheel surface. It is important to note that the surface of the grinding wheel is randomly created and the interaction between the diamond dresser and the wheel surface features is very complex so the model is not expected to match perfectly.

The amplitude parameters chosen for model validation include the root-mean-square height *Sq*, maximum peak height *Sp*, skewness *Ssk*, and kurtosis *Sku* of the selected area. The selected area modeled matched the same dimensions of the field of view using the Alicona surface metrology measurement equipment utilizing 5x optics resulting in a roughly 2.8 x 2.2 mm area.

The second step of validation compared the bearing area curve parameters computed from the simulated grinding wheel surface topography. The parameters most related to the surface of the grinding wheel topography included the distance between the highest and lowest level of the core surface *Sk*, average height of the protruding peaks above the core surface *Spk*, peak material volume of the surface *Vmp*, core material volume of surface *Vmc*, and core void volume of the surface *Vvc*.

The areal parameters resulting from the simulation matched the overall trends found during the experimental trials. In some cases, the simulated magnitudes were not as accurate but the statistical trends of simulated grinding wheel match within 20% and sometimes even better. The complete list of measured parameters for the different dressing conditions, listing magnitudes, standard deviation, and percentage difference are listed in the Appendix B.

7. CONCLUSION AND FUTURE WORK

The main objectives of this thesis were to: i) investigate different measurement methods for three-dimensional characterization of precision grinding wheels, ii) understand how the surface topography of a grinding wheel changes due to the single point diamond dressing process, iii) develop a method to model the 3D surface topography of grinding wheel surface under different dressing conditions, and iv) validate the resulting simulation results. This chapter summarizes the main conclusions of this thesis and suggests related areas for future investigation.

7.1 CHARACTERIZATION

This chapter focused on the characterization of the seeded-gel (SG) grinding wheel using multiple types of measurement equipment. Precision grinding wheels are often difficult to characterize due to the stochastic nature of abrasive grinding grains, which are randomly placed on the wheel surface during manufacture. Three-dimensional micro-coordinate metrology, scanning electron microscopy (SEM), and micro-tomography (μCT) were used to experimentally establish the statistical descriptors of the grinding wheel surface topography. The following conclusions are drawn from the work:

- In contrast to previous work [31], [39], [71], [82], [83], the wheel surface texture follows a negatively skewed beta distribution
- Abrasive grain diameters follow a Gaussian distribution, which is consistent with the majority of existing research [7], [8], [56], [102]

- Grain spacing follows a positively skewed beta distribution, which is in contrast to many existing models that assume a uniform distribution [7], [8], [60], [102] or the gamma distribution [51].
- Number of sides of the abrasive grains follows the Gamma distribution. This grain attribute is not usually considered in grinding wheel surface topography models, which tend to model the grains using simple shapes such as [8], [65]–[67].
- Grain aspect ratio follows a Weibull distribution. This grain attribute is not usually considered in existing grinding wheel topography models but is important to include since it has a bearing on the wheel-workpiece interaction.

7.2 DRESSING EXPERIMENTS

Single point dressing experiments on seeded-gel (SG) grinding wheels were performed and summarized in Chapter 3. The main conclusions of this work are as follows:

- Dressing affects the shape of the wheel surface texture height distribution, which follows a negatively skewed beta distribution
  - Shape parameters of the distribution (α and β) consistently change with the dressing condition
  - Peak height *Sp* increases with dressing infeed and lead indicating higher peaks are formed during the dressing process. In general, the lead parameter has a more dominant effect than the infeed.
  - The asymmetry of the wheel surface texture height distribution shifts left, quantified by increasing skewness, *Ssk*, indicating the increasing sharpness of the grains with increase in the dressing parameters

  - The wheel surface texture distribution curve becomes less ‘peaked’, as indicated by the decreasing kurtosis, *Sku*

- The peak material (~3.5%) of the grains is much smaller than the core material (~85%) indicated by *Smr1* and *Smr2*, respectively
- Even though smaller in magnitude (percentage wise), the peak material (*Spk*, *Vmp*) was more affected by the interaction of the dressing diamond compared to the core material (*Sk*, *Vmc*, *Vvc*)
- Negligible changes were observed in the valley material (*Svk*, *Smr2*, and *Vvv*), which is attributed to the fact that the single point dresser interacts mainly with the surface of the grinding wheel
- The dressing lead has a strong influence on grain macro-fracture and dislodgement, as indicated by the decrease of *Vmc* and increase of *Vvc*, especially under aggressive dressing conditions

7.3 WHEEL TOPOGRAPHY MODELING AND VALIDATION

This chapter introduced a three-dimensional stochastic model to simulate the three-dimensional surface texture of a precision grinding wheel under different dressing conditions using statistical descriptors found in the experimental trials.

- The simulated and measured surfaces of the SG grinding wheel resulting from the same dressing parameters appear to be visually similar
- Amplitude parameters:
  - Model slightly over estimates the maximum height, indicated by the peak height *Spk* , but follows the overall trends and is within ~18% of the experimental values

  - The model’s lack of ability to simulate plateaued surfaces, at less aggressive dressing conditions, slightly offsets the shape of simulated texture height distribution as indicated by the skewness (*Ssk*) and kurtosis (*Sku*) parameters; *Ssk* and *Sku* are still within ~26% of the experimental values.
- Bearing area curve parameters:
  - Similar to *Ssk* and *Sku*, the simulated peak material section (*Spk*, *Vmp, Smr1*) has difficulty in duplicating the plateaued surface features resulting in values ranging from 41 to 71% of the experimental data
  - Core material section (*Sk, Vmc, Vvc*) simulates well and is within ~17% of the experimental data even though the model doesn’t appear to capture the full effect of grain dislodgement for aggressive dressing lead conditions

7.4 FUTURE WORK

Related areas for further research include the following:

- Apply and validate predictive regression analytical equations to model
- Develop a more precise method to measure the changes in abrasive grain shape (e.g. tip/corner radius and angle) due to changes in the dressing conditions
- Rotary dressing: A rotating grinding wheel and rotary dresser are more complicated than single point dressing and should be investigated
- Workpiece interaction: develop a wheel topography model that includes the effect of wheel interaction with the workpiece material

APPENDIX A

DIAMOND DRESSER WEAR

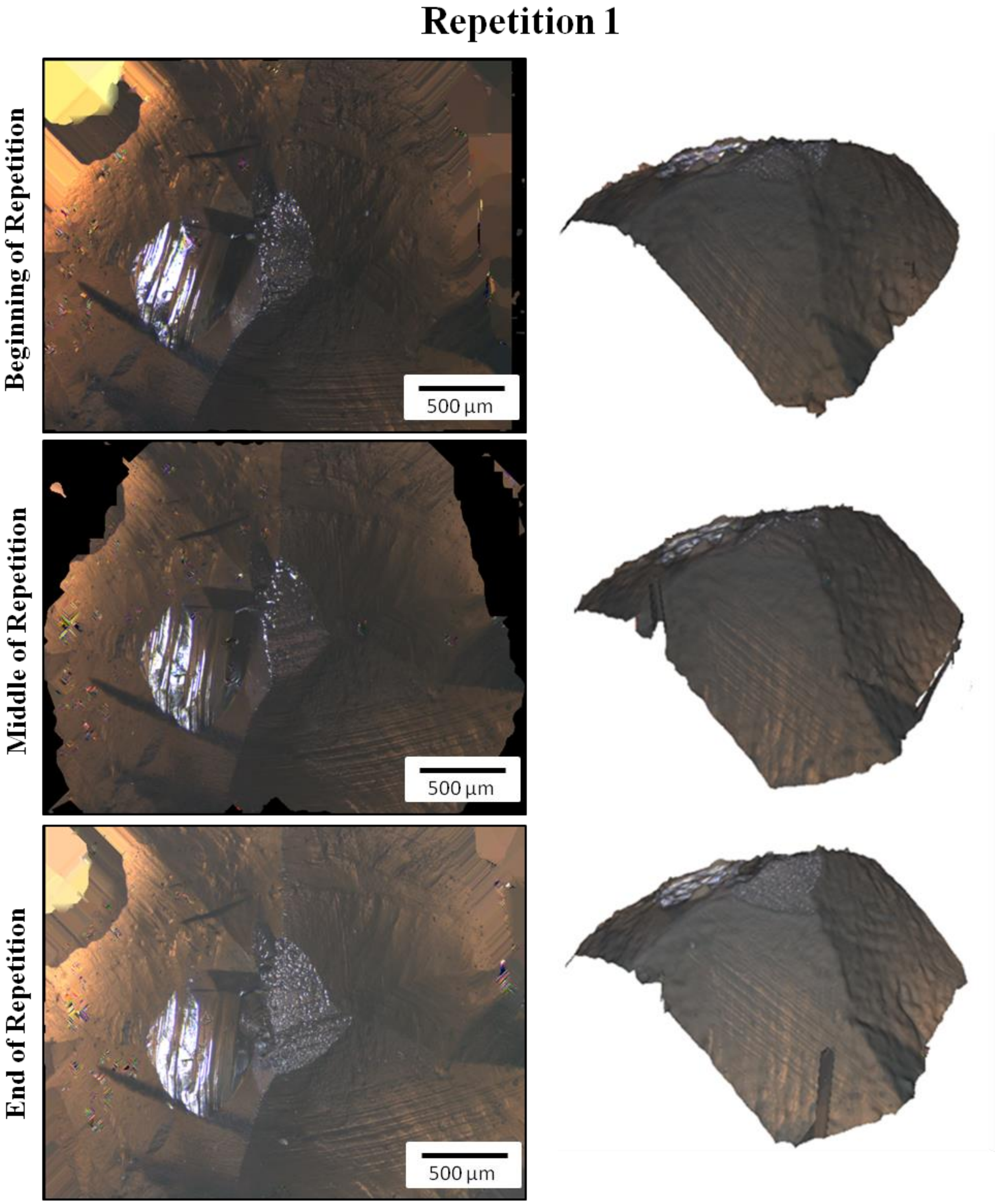

Repetition 2

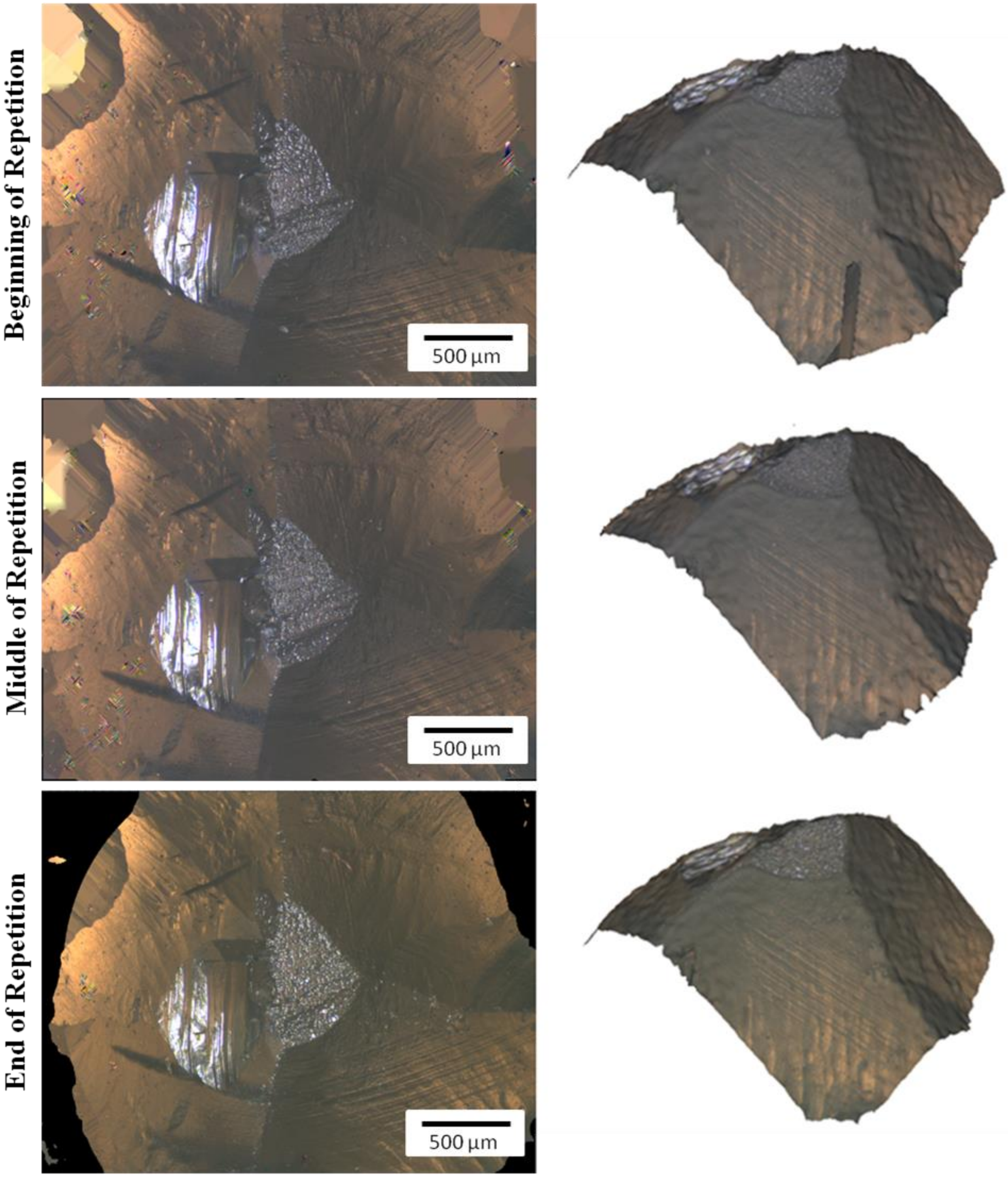

Repetition 3

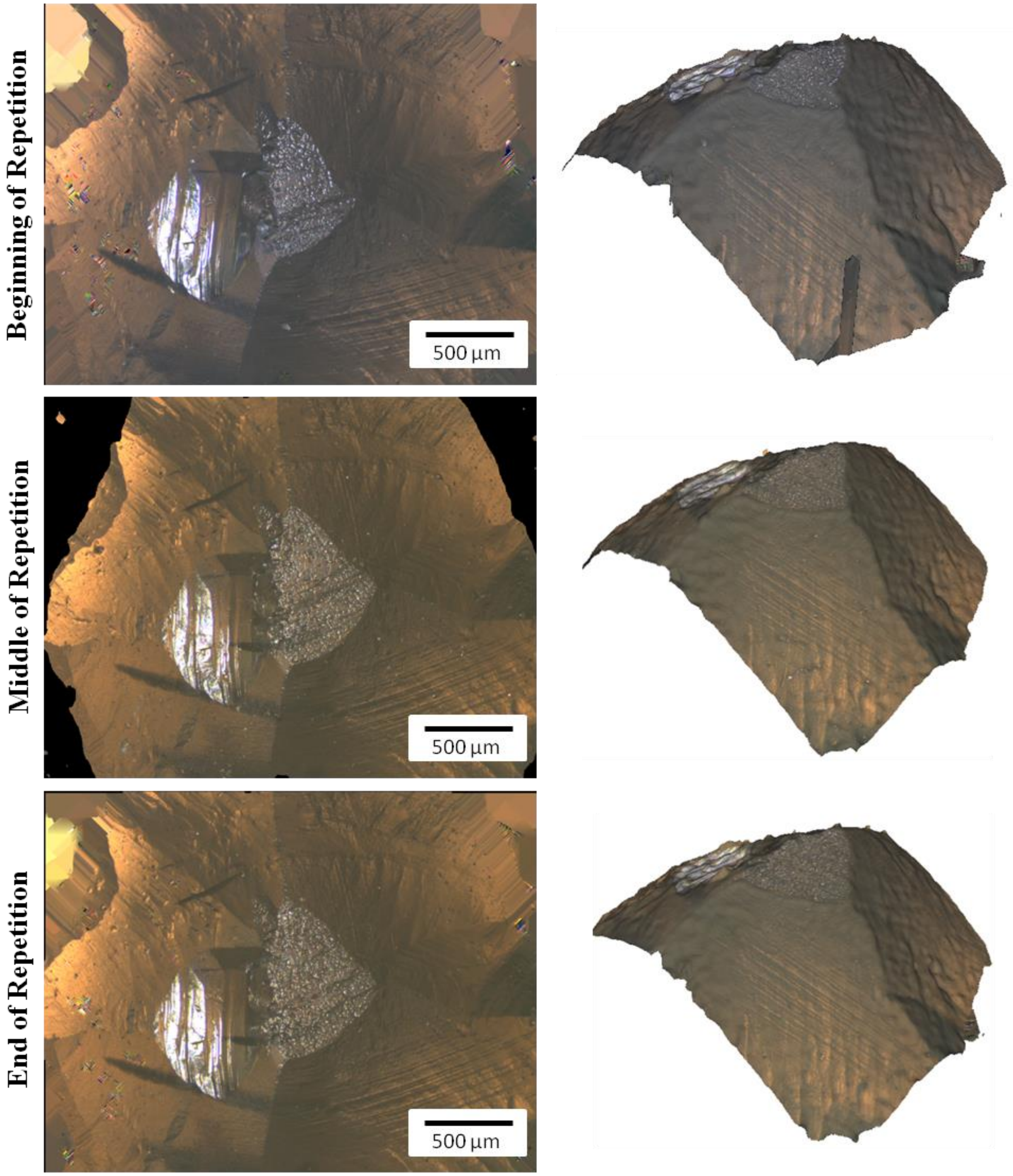

APPENDIX B

EXPERIMENTAL MEASUREMENT RESULTS

	INITIAL CONDITION					**CONDITION 1**				
Parameter	**Exp**	**±**	**Sim**	**±**	**% diff**	**Exp**	**±**	**Sim**	**±**	**% diff**
Sq (µm)	145.0280	5.6192	122.8220	9.6259	17	145.6822	3.1772	125.7638	9.2754	15
Sp (µm)	223.7925	13.5018	278.1707	19.9001	22	231.2172	8.1008	287.0918	20.8501	22
Ssk	-0.8841	0.1135	-0.6654	0.1728	28	-0.8579	0.0630	-0.6742	0.1604	24
Sku	3.6516	0.3855	3.3642	0.5319	8	3.5983	0.1644	3.3808	0.3810	6
Sk (µm)	330.8563	21.0939	306.4814	23.7093	8	337.4937	17.0422	307.8266	23.2715	9
Spk (µm)	21.2833	8.0706	56.2542	8.2470	90	24.6117	2.5794	59.4856	7.9448	83
Smr1 (%)	2.3868	0.9016	5.9220	0.9087	85	2.7137	0.4062	6.0186	0.8375	76
Vmp (ml/m²)	1.9688	0.3195	3.3767	0.3243	53	2.1777	0.1180	3.4952	0.3251	46
Vmc (ml/m²)	137.3317	6.8990	112.7109	9.7326	20	138.0730	3.5968	114.9640	9.6149	18
Vvc (ml/m²)	144.8892	7.6806	131.2413	9.5840	10	146.6012	6.6394	132.6541	8.7862	10
	CONDITION 2					**CONDITION 3**				
Parameter	**Exp**	**±**	**Sim**	**±**	**% diff**	**Exp**	**±**	**Sim**	**±**	**% diff**
Sq (µm)	142.6521	3.4269	123.3362	9.1691	15	142.4552	4.7154	124.9009	8.1653	13
Sp (µm)	229.2979	20.5578	286.2770	18.4869	22	232.5988	11.9854	289.3930	28.8013	22
Ssk	-0.8761	0.0700	-0.6478	0.1392	30	-0.8724	0.0300	-0.6702	0.1387	26
Sku	3.6918	0.1138	3.4183	0.4322	8	3.6857	0.1086	3.4071	0.3547	8
Sk (µm)	331.3858	22.7043	307.0259	21.4554	8	334.9502	15.2468	309.3644	16.4149	8
Spk (µm)	25.9004	8.1261	59.9316	9.1096	79	26.3302	3.0144	58.0036	9.1748	75
Smr1 (%)	2.6771	0.7014	6.2193	1.1288	80	2.7593	0.1115	5.9822	0.7279	74
Vmp (ml/m²)	2.1266	0.3649	3.5162	0.3458	49	2.2101	0.1582	3.4631	0.3445	44
Vmc (ml/m²)	133.9750	2.8670	113.0720	8.8912	17	133.1560	4.0164	114.0467	7.4974	15
Vvc (ml/m²)	143.7312	7.9878	132.2529	8.0644	8	143.8100	5.8256	132.5112	6.6143	8
	CONDITION 4					**CONDITION 5**				
Parameter	**Exp**	**±**	**Sim**	**±**	**% diff**	**Exp**	**±**	**Sim**	**±**	**% diff**
Sq (µm)	141.7549	2.7486	120.1405	8.1580	17	145.7942	2.5393	124.6555	7.7055	16
Sp (µm)	227.1241	10.3158	280.8248	27.8021	21	250.2984	5.5208	291.8981	20.1979	15
Ssk	-0.8690	0.0635	-0.5974	0.1773	37	-0.8188	0.0389	-0.5876	0.1322	33
Sku	3.6730	0.2503	3.2675	0.5198	12	3.5779	0.1011	3.2564	0.3495	9
Sk (µm)	330.2518	15.0027	305.5846	27.1297	8	350.1788	9.5738	314.0561	23.5932	11
Spk (µm)	25.6438	3.5710	58.2136	7.5616	78	33.2960	0.2600	62.6803	10.2292	61
Smr1 (%)	2.7758	0.3755	6.0759	0.9547	75	3.5999	0.2829	6.3563	1.0886	55
Vmp (ml/m²)	2.1807	0.1817	3.4375	0.3493	45	2.5293	0.0137	3.6687	0.3997	37
Vmc (ml/m²)	133.7722	3.4207	111.1539	10.0307	18	136.9322	3.0716	115.0664	8.4552	17
Vvc (ml/m²)	142.8114	5.2360	130.5300	10.2454	9	150.7806	4.8530	135.4151	9.0746	11

	CONDITION 6					CONDITION 7				
Parameter	**Exp**	**±**	**Sim**	**±**	**% diff**	**Exp**	**±**	**Sim**	**±**	**% diff**
Sq (µm)	147.9948	0.4775	128.1750	6.0853	14	144.5599	1.8905	123.2124	7.3266	16
Sp (µm)	261.5440	1.2584	293.1475	19.8658	11	235.9030	2.5358	282.4596	19.1873	18
Ssk	-0.7575	0.0281	-0.6717	0.1411	12	-0.8406	0.0450	-0.6348	0.1091	28
Sku	3.4352	0.0692	3.3834	0.4018	2	3.5376	0.1300	3.2105	0.3429	10
Sk (µm)	363.6836	6.5390	311.0618	14.7656	16	342.2945	5.8792	310.3204	18.3742	10
Spk (µm)	37.1343	1.4713	63.2745	8.1834	52	26.4489	2.6049	59.6388	9.8527	77
Smr1 (%)	3.9487	0.1033	6.2800	0.9758	46	2.7682	0.2019	6.0710	1.0223	75
Vmp (ml/m²)	2.8162	0.0846	3.6205	0.2989	25	2.2226	0.1012	3.5028	0.3783	45
Vmc (ml/m²)	138.9152	0.2753	116.2535	6.3773	18	136.1613	1.7404	113.8697	6.8947	18
Vvc (ml/m²)	155.5107	1.0103	135.4512	6.1225	14	147.2062	2.1283	133.1893	6.2398	10
	CONDITION 8					**CONDITION 9**				
Parameter	**Exp**	**±**	**Sim**	**±**	**% diff**	**Exp**	**±**	**Sim**	**±**	**% diff**
Sq (µm)	147.8516	2.1540	129.5215	8.6443	13	145.4718	1.5464	125.8203	7.7465	14
Sp (µm)	252.7446	3.9725	294.9615	21.4893	15	260.4319	6.2752	295.0171	21.9835	12
Ssk	-0.8037	0.0475	-0.6361	0.1781	23	-0.7536	0.0513	-0.6261	0.1591	18
Sku	3.5682	0.1315	3.2921	0.4272	8	3.4333	0.1337	3.3633	0.3764	2
Sk (µm)	361.8311	7.6062	319.2747	15.2029	12	361.0580	5.2628	313.4187	20.9092	14
Spk (µm)	33.2383	0.8257	64.8061	9.2213	64	37.6297	2.0351	64.5508	10.0934	53
Smr1 (%)	3.6426	0.2746	6.2469	0.5711	53	4.0369	0.2791	6.0733	0.8602	40
Vmp (ml/m²)	2.6247	0.0881	3.7163	0.4031	34	2.7440	0.0773	3.6664	0.3853	29
Vmc (ml/m²)	138.3628	2.7697	118.3069	7.1226	16	136.0875	1.1837	115.4412	8.5012	16
Vvc (ml/m²)	154.3737	3.5600	138.0210	6.1825	11	154.1721	2.7706	134.6198	7.9627	14

REFERENCES

[1] A. Saad, “Influence of Dresssing Parameters on the Performance of Aluminum Oxide Grinding Wheels,” M.S. Thesis, Mechanical Engineering, Dalhousie University, 2009.

[2] H. Baseri, S. M. Rezaei, a. Rahimi, and M. Rezaeian, “Modelling of Disc Dressing Forces,” *Mach. Sci. Technol.*, vol. 11, no. 2, pp. 201–216, May 2007.

[3] T. A. Nguyen and D. L. Butler, “Simulation of Surface Grinding Process, Part 2: Interaction of the Abrasive Grain with the Workpiece,” *Int. J. Mach. Tools Manuf.*, vol. 45, no. 11, pp. 1329–1336, Sep. 2005.

[4] J. B. J. W. Hegeman, “Fundamentals of Grinding: Surface Conditions of Ground Materials,” PhD Thesis, University of Groningen, 2000.

[5] J. Xie and J. Tamaki, “Computer Simulation of Sub-Micron-Scale Precision Truing of a Metal-Bonded Diamond Grinding Wheel,” *Int. J. Mach. Tools Manuf.*, vol. 48, no. 10, pp. 1111–1119, Aug. 2008.

[6] D. V. De Pellegrin, N. D. Corbin, G. Baldoni, and A. A. Torrance, “Diamond Particle Shape: Its Measurement and Influence in Abrasive Wear,” *Tribol. Int.*, vol. 42, no. 1, pp. 160–168, Jan. 2009.

[7] X. Chen and W. B. Rowe, “Analysis and Simulation of the Grinding Process. Part I: Generation of the Grinding Wheel Surface,” *Int. J. Mach. Tools Manuf.*, vol. 36, no. 8, pp. 871–882, Aug. 1996.

[8] P. Koshy, V. K. Jain, and G. K. Lal, “Stochastic Simulation Approach to Modelling Diamond Wheel Topography,” *Int. J. Mach. Tools …*, vol. 37, no. 6, pp. 751–761, 1997.

[9] T. W. Hwang, C. J. Evans, and S. Malkin, “An Investigation of High Speed Grinding with Electroplated Diamond Wheels,” *CIRP Ann. - Manuf. Technol.*, vol. 49, no. 1, pp. 245–248, Jan. 2000.

[10] P. J. Scott, “Feature Parameters,” *Wear*, vol. 266, no. 5–6, pp. 548–551, Mar. 2009.

[11] P. Herzenstiel and J. C. Aurich, “CBN-Grinding Wheel With a Defined Grain Pattern – Extensive Numerical and Experimental Studies,” *Mach. Sci. Technol.*, vol. 14, no. 3, pp. 301–322, Nov. 2010.

[12] F. W. Pinto, “An Experimental and Numerical Approach to Investigate the Machining Performance of Engineered Grinding Tools.” PhD Thesis, Eth Zurich, 2008.

[13] W. R. Backer, E. R. Marshall, and M. C. Shaw, “The Size Effect in Metal Cutting,” *Trans. ASME*, vol. 74, pp. 61–72, 1952.

[14] M. C. Shaw, D. A. Farmer, and K. Nakayama, “Mechanics of the Abrasive Cut-off Operation,” *Trans. ASME J. Eng. Ind.*, vol. 89, pp. 495–502, 1967.

[15] S. Lachance, A. Warkentin, and R. Bauer, “Development of an Automated System for Measuring Grinding Wheel Wear Flats,” *J. Manuf. Syst.*, 2003.

[16] R. Cai and W. B. Rowe, “Assessment of Vitrified CBN Wheels for Precision Grinding,” *Int. J. Mach. Tools Manuf.*, vol. 44, no. 12–13, pp. 1391–1402, Oct. 2004.

[17] J. A. Badger, “Microfracturing Ceramic Abrasive in Grinding,” *ASME 2012 Int. …*, no. 3, pp. 1–9, 2012.

[18] K. Syoji, L. Zhou, and S. Matsui, “Studies on Truing and Dressing of Diamond Wheels (1st Report)—the Measurement of Protrusion Height of Abrasive Grains by Using a Stereo Pair and the Influence of Protrusion Height on Grinding Performance,” *Bull. Japan Soc. Precis. Eng.*, vol. 24, no. 2, pp. 124–129, 1990.

[19] K. J. Stout and E. J. Davis, “Surface Topography of Cylinder Bores — the Relationship between Manufacture, Characterization and Function,” *Wear*, vol. 95, no. 2, pp. 111–125, Apr. 1984.

[20] A. Darafon, A. Warkentin, and R. Bauer, “Characterization of Grinding Wheel Topography Using a White Chromatic Sensor,” *Int. J. Mach. Tools Manuf.*, vol. 70, pp. 22–31, Jul. 2013.

[21] R. E. Reason, “Progress in the Appraisal of Surface Topography during the First Half-Century of Instrument Development,” *Wear*, vol. 57, no. 1, pp. 1–16, Nov. 1979.

[22] K. J. Stout, T. G. King, and D. J. Whitehouse, “Analytical Techniques in Surface Topography and Their Application to a Running-in Experiment,” *Wear*, vol. 43, no. 1, pp. 99–115, May 1977.

[23] T. R. Thomas, *Rough surfaces*, 2nd ed. London: Imperial College Press, 1999.

[24] K. J. Stout and W. P. Dong, *Three Dimensional Surface Topography; Measurement, Interpretation and Applications: A Survey and Bibliography*. London ; Bristol, Pa.: Penton Press., 1994.

[25] D. J. Whitehouse, *Handbook of Surface Metrology*. Bristol ; Philadelphia: Institute of Physics Publishing, 1994.

[26] M. Hasegawa, “Statistical Analysis for the Generating Mechanism of Ground Surface Roughness,” *Wear*, vol. 29, no. 1, pp. 31–39, Jul. 1974.

[27] H. T. McAdams, “The Role of Topography in the Cutting Performance of Abrasive Tools,” *J. Manuf. Sci. Eng.*, vol. 86, no. 1, p. 75, 1964.

[28] C. E. Davis, “The Dependence of Grinding Wheel Performance on Dressing Procedure,” *Int. J. Mach. Tool Des. Res.*, vol. 14, no. 1, pp. 33–52, Mar. 1974.

[29] T. J. Vickerstaff, “The Influence of Wheel Dressing on the Surface Generated in the Grinding Process,” *Int. J. Mach. Tool Des. Res.*, vol. 16, no. 2, pp. 145–152, 1976.

[30] T. Buttery, A. Statham, J. Percival, and M. Hamed, “Some Effects of Dressing on Grinding Performance,” *Wear*, 1979.

[31] F. Nassirpour and S. M. Wu, “Characterization and Analysis of Grinding Wheel Topography as a Stochastic Isotropic Surface,” *J. Eng. Ind.*, vol. 101, no. 79, pp. 165–170, 1979.

[32] J. B. . Williamson, “Microtopography of Surfaces,” in *Proceedings of the Institution of Mechanical Engineers*, 1967, vol. 182, no. 11.

[33] J. Peklenik and M. Kubo, “A Basic Study of a Three Dimensional Assessment of the Surface Generated in a Manufacturing Process,” *Ann. CIRP*, vol. 6, pp. 257–265.

[34] A. Waterworth, “Quantitative Characterization of Surface Finishes on Stainless Steel Sheet Using 3D Surface Topography Analysis.” PhD Thesis, University of Huddersfield, 2006.

[35] T. A. Nguyen and D. L. Butler, “Correlation of Grinding Wheel Topography and Grinding Performance: A Study from a Viewpoint of Three-Dimensional Surface Characterisation,” *J. Mater. Process. Technol.*, vol. 208, no. 1–3, pp. 14–23, Nov. 2008.

[36] D. L. Butler, L. A. Blunt, B. K. See, J. A. Webster, and K. J. Stout, “The Characterisation of Grinding Wheels Using 3D Surface Measurement Techniques,” *J. Mater. Process. Technol.*, vol. 127, no. 2, pp. 234–237, Sep. 2002.

[37] Z. Prusak, J. A. Webster, and I. D. Marinescu, “Influence of Dressing Parameters on Grinding Performance of CBN / Seeded Gel Hybrid Wheels in Cylindrical Grinding,” *Int. J. Prod. Res.*, vol. 35, no. 10, pp. 2899–2915, 1997.

[38] T. A. Nguyen and D. L. Butler, “Simulation of Precision Grinding Process, Part 1: Generation of the Grinding Wheel Surface,” *Int. J. Mach. Tools Manuf.*, vol. 45, no. 11, pp. 1321–1328, Sep. 2005.

[39] L. A. Blunt and S. Ebdon, “The Application of Three-Dimensional Surface Measurement Techniques to Characterizing Grinding Wheel Topography,” *Int. J. Mach. Tools …*, vol. 36, no. 1, pp. 1207–1226, 1996.

[40] W. P. Dong, P. J. Sullivan, and K. J. Stout, “Comprehensive Study of Parameters for Characterising Three-Dimensional Surface Topography: IV: Parameters for Characterising Spatial and Hybrid Properties,” *Wear*, vol. 35, no. 2, pp. 263–271, 1994.

[41] J. K. Brennan, “Algorithms for Surface Texture Profiles and Parameters,” no. 2010. Doctoral dissertation,University of Huddersfield, 2010.

[42] S. Shimizu and H. Sakamoto, “On-Machine Monitoring of the Wheel-Working Surface Condition with the Relative Frequency Distribution of its Profile,” *Key Eng. Mater.*, vol. 196, no. 2001, pp. 111–120, 2001.

[43] E. Brinksmeier and F. Werner, “Monitoring of Grinding Wheel Wear,” *CIRP Ann. - Manuf. Technol.*, vol. 41, no. 1, pp. 373–376, Jan. 1992.

[44] J. Liu, W. Y. Chen, and F. Chen, “Three-Dimensional Wheel Topography Measurement with Laser Triangulation,” *Key Eng. Mater.*, vol. 499, no. 2012, pp. 384–389, Jan. 2012.

[45] W. Liu, Z. H. Deng, L. L. Wan, Q. P. Wu, and H. Tang, “Progress of Researches on the Surface Topography Detection Techniques for Grinding Wheel,” *Adv. Mater. Res.*, vol. 797, no. 2013, pp. 505–510, Sep. 2013.

[46] L. Yan, Y. M. Rong, F. Jiang, and Z. X. Zhou, “Three-Dimension Surface Characterization of Grinding Wheel Using White Light Interferometer,” *Int. J. Adv. Manuf. Technol.*, vol. 55, no. 1–4, pp. 133–141, Dec. 2010.

[47] L. Yan, Z. X. Zhou, F. Jiang, and Y. M. Rong, “The Application of Three-Dimensional Surface Parameters to Characterizing Grinding Wheel Topography,” *Adv. Mater. Res.*, vol. 126–128, no. 2010, pp. 603–608, Aug. 2010.

[48] M. F. Ismail, K. Yanagi, and H. Isobe, “Characterization of Geometrical Properties of Electroplated Diamond Tools and Estimation of Its Grinding Performance,” *Wear*, vol. 271, no. 3–4, pp. 559–564, Jun. 2011.

[49] P. Demircioglu and M. N. Durakbasa, “Investigations on Machined Metal Surfaces through the Stylus Type and Optical 3D Instruments and Their Mathematical

Modeling with the Help of Statistical Techniques techniques," *Measurement*, vol. 44, no. 4, pp. 611–619, May 2011.

[50] H. J. Jordan, M. Wegner, and H. Tiziani, "Highly Accurate Non-Contact Characterization of Engineering Surfaces Using Confocal Microscopy," *Meas. Sci. Technol.*, vol. 9, no. 7, pp. 1142–1151, Jul. 1998.

[51] A. Darafon, "Measuring and Modeling of Grinding Wheel Topography," no. April 2013. Doctoral Dissertation, Dalhousie University, Halifax, Nova Scotia, 2013.

[52] W. Kapłonek, K. Nadolny, R. Tomkowski, and J. Valicek, "High-Accuracy Surface Topography Measurements of Abrasive Tools Using a 3D Optical Profiling System," *Meas Autom Monit*, vol. 58, no. 5, pp. 443–447, 2012.

[53] F. Blateyron, "Chromatic Confocal Microscopy," in *Optical Measurement of Surface Topography*, Springer Berlin Heidelberg, 2011, pp. 71–106.

[54] D. A. Doman, A. Warkentin, and R. Bauer, "A Survey of Recent Grinding Wheel Topography Models," *Int. J. Mach. Tools Manuf.*, vol. 46, no. 3–4, pp. 343–352, Mar. 2006.

[55] J. Verkerk, "Final Report concerning CIRP Cooperative Work on the Characterization of Grinding Wheel Topography," *Ann. CIRP*, vol. 26, no. 2, pp. 385–395, 1977.

[56] H. Baseri, S. M. Rezaei, a. Rahimi, and M. Saadat, "Analysis of the Disc Dressing Effects on Grinding Performance—Part 1: Simulation of the Disc Dressed Wheel Surface," *Mach. Sci. Technol.*, vol. 12, no. 2, pp. 183–196, May 2008.

[57] S. Malkin and C. Guo, *Grinding Technology:Theory and Application of Machining with Abrasives*. E. Horwood (Chichester and New York), 1989.

[58] P. Koshy, V. K. Jain, and G. K. Lal, "A Model for the Topography of Diamond Grinding Wheels," *Wear*, vol. 169, no. 2, pp. 237–242, Oct. 1993.

[59] J. Peklenik, R. Lane, and M. C. Shaw, "Comparison of Static and Dynamic Hardness of Grinding Wheels," *Trans ASME J. Eng. Ind.*, vol. 86, no. 3, pp. 294–297, 1964.

[60] Q. Feng, Q. Wang, and C. Z. Ren, "Three-Dimensional Simulation of Wheel Topography," vol. 487, pp. 149–154, 2011.

[61] Z. B. Hou and R. Komanduri, "On the Mechanics of the Grinding Process – Part I. Stochastic Nature of the Grinding Process," *Int. J. Mach. Tools Manuf.*, vol. 43, no. 15, pp. 1579–1593, Dec. 2003.

[62] A. Koziarski and A. Gołąbczak, "The Assessment of the Grinding Wheel Cutting Surface Condition After Dressing with the Single Point Diamond Dresser," *Int. J. Mach. Tool Des. …*, vol. 25, no. 4, pp. 313–325, 1985.

[63] E. J. Salisbury, K. V. Domala, K. S. Moon, M. H. Miller, and J. W. Sutherland, "A Three-Dimensional Model for the Surface Texture in Surface Grinding, Part 2: Grinding Wheel Surface Texture Model," *J. Manuf. Sci. Eng.*, vol. 123, no. 4, p. 582, 2001.

[64] D. V. De Pellegrin and G. W. Stachowiak, "Evaluating the Role of Particle Distribution and Shape in Two-Body Abrasion by Statistical Simulation," *Tribol. Int.*, vol. 37, no. 3, pp. 255–270, 2004.

[65] W. L. Cooper and A. S. Lavine, "Grinding Process Size Effect and Kinematics Numerical Analysis," *J. Manuf. Sci. Eng.*, vol. 122, no. 1, pp. 59–69, 2000.

[66] G. Warnecke and U. Zitt, "Kinematic Simulation for Analyzing and Predicting High-Performance Grinding Processes," *CIRP Ann. Technol.*, vol. 47, pp. 265–270, 1998.

[67] X. Chen and W. B. Rowe, "Analysis and simulation of the grinding process. Part II: Mechanics of grinding," *Int. J. Mach. Tools …*, 1996.

[68] R. Hecker, "Part Surface Roughness Modeling and Process Optimal Control of Cylindrical Grinding," 2002.

[69] W. Lortz, "A Model of the Cutting Mechanism in Grinding," *Wear*, vol. 53, no. 1, pp. 115–128, Mar. 1979.

[70] T. R. Thomas, "Recent Advances in the Measurement and Analysis of Surface Microgeometry," *Wear*, vol. 33, no. 2, pp. 205–233, 1975.

[71] S. Jacobson, P. Wallén, and S. Hogmark, "Fundamental Aspects of Abrasive Wear Studied by a New Numerical Simulation Model," *Wear*, vol. 123, no. 2, pp. 207–223, Apr. 1988.

[72] Y. Xie and J. Williams, "The Prediction of Friction and Wear When a Soft Surface Slides against a Harder Rough Surface," *Wear*, vol. 1648, no. 95, 1996.

[73] J. Jiang, F. Sheng, and F. Ren, "Modelling of two-body abrasive wear under multiple contact conditions," *Wear*, vol. 217, no. 1, pp. 35–45, Apr. 1998.

[74] N. Kramer and C. Wangenheim, "Model Based Characterization of the Grinding Wheel Effective Topography," *Key Eng. Mater.*, vol. 389–390, no. 2009, pp. 258–263, 2009.

[75] J. A. Badger and A. A. Torrance, “A Comparison of Two Models to Predict Grinding Forces from Wheel Surface Topography,” *Int. J. Mach. Tools Manuf.*, vol. 40, no. 8, pp. 1099–1120, Jun. 2000.

[76] P. Guan, J. Q. Li, S. Zhu, T. B. Yu, and W. S. Wang, “Advances in Simulation of Grinding Process,” *Appl. Mech. Mater.*, vol. 121–126, pp. 1879–1885, Oct. 2011.

[77] E. Brinksmeier, J. C. Aurich, E. Govekar, C. Heinzel, H.-W. Hoffmeister, F. Klocke, J. Peters, R. Rentsch, D. J. Stephenson, E. Uhlmann, K. Weinert, and M. Wittmann, “Advances in Modeling and Simulation of Grinding Processes,” *CIRP Ann. - Manuf. Technol.*, vol. 55, no. 2, pp. 667–696, Jan. 2006.

[78] J. Xie, F. Wei, J. H. Zheng, J. Tamaki, and A. Kubo, “3D Laser Investigation on Micron-Scale Grain Protrusion Topography of Truncated Diamond Grinding Wheel for Precision Grinding Performance,” *Int. J. Mach. Tools Manuf.*, vol. 51, no. 5, pp. 411–419, May 2011.

[79] X. Chen, W. B. Rowe, B. Mills, and D. R. Allanson, “Analysis and Simulation of the Grinding Process. Part III: Comparison with Experiment,” *Int. J. Mach. …*, vol. 36, no. 8, pp. 897–906, 1996.

[80] J. Eranki, G. Xiao, and S. Malkin, “Evaluating the Performance of ‘Seeded Gel’ Grinding Wheels,” *J. Mater. Process. Technol.*, vol. 32, no. 3, pp. 609–625, Aug. 1992.

[81] I. D. Marinescu, M. Hitchiner, E. Uhlmann, W. B. Rowe, and I. Inasaki, *Handbook of Machining with Grinding Wheels*. CRC Press, 2006.

[82] X. Zhou and F. Xi, “Modeling and Predicting Surface Roughness of the Grinding Process,” *Int. J. Mach. Tools Manuf.*, vol. 42, no. 8, pp. 969–977, Jun. 2002.

[83] S. Chakrabarti and S. Paul, “Numerical Modelling of Surface Topography in Superabrasive Grinding,” *Int. J. Adv. Manuf. Technol.*, vol. 39, no. 1–2, pp. 29–38, 2008.

[84] K. Brakhage, M. Makowski, F. Klocke, and M. Weiss, “Grinding Wheel Modeling : Development of a Mathematical Model,” *MASCOT11 Proceedings—IMACS Ser. Comput. Appl. Math.*, 2011.

[85] H. T. McAdams, “A Statistical Polyhedron Model of Abrasive Grain,” *J. Eng. Ind.*, vol. 85, no. 62, pp. 388–393, 1963.

[86] H.-C. Chang and J.-J. J. Wang, “A Stochastic Grinding Force Model Considering Random Grit Distribution,” *Int. J. Mach. Tools Manuf.*, vol. 48, no. 12–13, pp. 1335–1344, Oct. 2008.

[87] E. Brinksmeier and M. Cinar, “Characterization of Dressing Processes by Determination of the Collision Number of the Abrasive Grits,” *CIRP Ann. Technol.*, vol. 44, no. 2, pp. 299–304, 1995.

[88] L. A. Blunt and Jiang X., *Advanced Techniques for Assessment Surface topography: Development of a Basis for 3D Surface Texture Standards“ Surfstand.”*London ; Sterling, VA: Kogan Page Science, 2003.

[89] C. P. Bhateja, “On the Mechanism of the Diamond Dressing of Grinding Wheels,” *Proc. Int. Conf. Prod. Eng.*, p. 733, 1974.

[90] F. Helmli, “Focus variation instruments,” in *Optical Measurement of Surface Topography,* Springer Berlin Heidelberg, 2011, pp. 131–166.

[91] O. Huber, “Focus Variation – A New Technology for High Resolution Optical 3D Surface Metrology in the Micro- and Nanometer Range,” *EGU Gen. Assem. Conf. Abstr.*, vol. 11, 2009.

[92] S. Malkin and N. H. Cook, “The Wear of Grinding Wheels: Part 1—Attritious Wear,” *J. Eng. Ind.*, vol. 93, no. 4, pp. 1120–1128, 1971.

[93] S. Malkin and N. H. Cook, “The Wear of Grinding Wheels: Part 2—Fracture Wear,” *J. Eng. Ind.*, vol. 93, no. 4, pp. 1129–1133, 1971.

[94] H. Yoshikawa and T. Sata, “Study on Wear of Grinding Wheels: 1—Bond Fracture in Grinding Wheels,” *J. Eng. Ind.*, vol. 85, no. 1, pp. 39–42, 1963.

[95] G. Pahlitzsch and J. Appun, “Effect of Truing Conditions on Circular Grinding,” *Ind. Diam. Rev*, vol. 14, no. 185–189, pp. 212–217, 1954.

[96] R. P. Lindsay, “Dressing and Its Effect on Grinding Performance,” *Tech. Pap. MR*, pp. 69–568, 1969.

[97] T. J. Vickerstaff, “Diamond Dressing-Its Effect on Work Surface Roughness,” *Ind. Diam. Rev.*, vol. 30, no. 356, pp. 260–267, 1970.

[98] S. Malkin and T. Murray, “Mechanics of Rotary Dressing of Grinding Wheels,” *ASME*, vol. 100, no. 1, pp. 95–102, 1978.

[99] S. Malkin, “Grinding of Metals : Theory and Application,” *J. Appl. Metalwork.*, vol. 3, no. 2, pp. 95–109, 1984.

[100] H. K. Tönshoff, J. Peters, I. Inasaki, and T. Paul, “Modelling and Simulation of Grinding Processes,” *CIRP Ann. …*, vol. 41, no. 1, pp. 677–688, 1992.

[101] K. Gotoh and J. L. Finney, “Representation of the Size and Shape of a Single Particle,” *Powder Technol.*, vol. 12, no. 2, pp. 125–130, Sep. 1975.

[102] D. X. Chen and Q. Feng, “A Methodology for the Simulation of Surface-Contact Grinding Tool Topography,” *Key Eng. Mater.*, vol. 416, pp. 348–353, Sep. 2009.

[103] C. M. Borror, *Certified Quality Engineer Handbook*, 3rd ed. American Society for Quality (ASQ), 2009.

[104] D. B. Kececioglu, *Reliability & Life Testing Handbook, Volume 1*. DEStech Publications, 2002.

[105] J. Xie, J. Xu, Y. Tang, and J. Tamaki, “3D Graphical Evaluation of Micron-Scale Protrusion Topography of Diamond Grinding Wheel,” *Int. J. Mach. Tools Manuf.*, vol. 48, no. 11, pp. 1254–1260, Sep. 2008.

[106] W. Choi, T. R. Kurfess, and J. Cagan, “Sampling Uncertainty in Coordinate Measurement Data Analysis,” *Precis. Eng.*, vol. 22, no. 3, pp. 153–163, Jul. 1998.

[107] D. J. Whitehouse, “Beta Functions for Surface Typologie,” *Ann. CIRP*, vol. 27, no. 1, pp. 194–497, 1978.

[108] G. P. Petropoulos, C. N. Pandazaras, N. M. Vaxevanidis, and A. Antoniadis, “Multi-Parameter Identification and Control of Turned Surface Textures,” *Int. J. Adv. Manuf. Technol.*, vol. 29, no. 1–2, pp. 118–128, Nov. 2005.

[109] K. Krishnamoorthy, *Handbook of Statistical Distributions with Applications*, 7th. ed. Boca Raton, FL: Chapman & Hall/CRC, 2006.

[110] K. Pankratov, “Intersection of Polygons Using isintpl.m.” Massachusetts Institute of Technology, 2005.

[111] G. Jacquenot, “Minimum Distance Between Two Polygons Using min_dist_between_two_polygons.” MATLAB Central File Exchange, 2008.

[112] V. Pacitti and C. Rubenstein, “The Influence of the Dressing Depth of Cut on the Performance of a Single Point Diamond Dressed Alumina Grinding Wheel,” *Int. J. Mach. Tool Des. ...*, vol. 12, pp. 267–279, 1972.

[113] J. C. Aurich, P. Herzenstiel, H. Sudermann, and T. Magg, “High-Performance Dry Grinding Using a Grinding Wheel with a Defined Grain Pattern,” *CIRP Ann. - Manuf. Technol.*, vol. 57, no. 1, pp. 357–362, Jan. 2008.

[114] R. C. Kalil, “Evaluation of Frictional Characteristics of Precision Machined Surfaces.” Master’s Thesis, Georgia Institute of Technology, 2004.

[115] W. P. Dong, E. Mainsah, and K. J. Stout, “Reference Planes for the Assessment of Surface Roughness in Three Dimensions,” *Int. J. Mach. Tools Manuf.*, vol. 35, no. 2, pp. 263–271, Feb. 1995.

[116] G. Wiora, “X3P: Open Source Implementation of an ISO5436-2 based XML Data Format.” openGPS Software, 2008.

[117] M. Sedlaček, B. Podgornik, and J. Vižintin, “Correlation between Standard Roughness Parameters Skewness and Kurtosis and Tribological Behaviour of Contact Surfaces,” *Tribol. Int.*, vol. 48, pp. 102–112, Apr. 2012.

[118] R. Leach, L. Brown, X. Jiang, R. Blunt, M. Conroy, and D. Mauger, “Measurement Good Practice Guide No. 108 ‘Guide to the Measurement of Smooth Surface Topography using Coherence Scanning Interferometry,’” no. 108. Teddington, UK, 2008.

[119] R. A. Waikar and Y. B. Guo, “A Comprehensive Characterization of 3D Surface Topography Induced by Hard Turning versus Grinding,” *J. Mater. Process. Technol.*, vol. 197, no. 1–3, pp. 189–199, Feb. 2008.

[120] ISO, “Geometrical Product SpecifiCation (GPS)—Surface Texture:Areal - Part 2: Terms, Definitions and Surface Texture Parameters.” ISO 25178-2:2012, 2012.

[121] E. S. Gadelmawla, M. M. Koura, T. M. A. Maksoud, I. M. Elewa, and H. H. Soliman, “Roughness parameters,” *J. Mater. Process. Technol.*, vol. 123, no. 1, pp. 133–145, Apr. 2002.

[122] A. Strabe, “Alicona: IF-MeasureSuite Manual EN.” Raaba/Graz, 2013.

[123] F. Blateyron, “The Areal Feature Parameters,” in *Characterisation of Areal Surface Texture*, R. Leach, Ed. Berlin, Heidelberg: Springer Berlin Heidelberg, 2013, pp. 45–65.

[124] F. Blateyron, “The Areal Field Parameters,” in *Characterisation of Areal Surface Texture*, R. Leach, Ed. Berlin, Heidelberg: Springer Berlin Heidelberg, 2013, pp. 15–43.